JETP Letters, Vol. 74, No. 3, 2001, pp. 129–132. Translated from Pis'ma v Zhurnal Éksperimental'noĭ i Teoreticheskoĭ Fiziki, Vol. 74, No. 3, 2001, pp. 147–150.

What Should Be the Spectrum of Galactic Cosmic Rays?

N. L. Grigorov and E. D. Tolstaya*

Skobel'tsyn Research Institute of Nuclear Physics, Moscow State University, Vorob'evy gory, Moscow, 119899 Russia

** e-mail: katya@srdlan.npi.msu.su*

Received June 14, 2001

Numerous experimental data on cosmic rays sensitive to the spectrum of primary cosmic rays were analyzed in the energy range $E > 1$ TeV. They proved to be incompatible with the pure power-law spectrum of primary particles. The spectral index of the proton spectrum is derived from the data considered. It was found to be 0.4 ± 0.1 greater than for the nuclei with $Z \geq 2$. Therefore, the flux of galactic cosmic rays consisting of protons and nuclei with $Z \geq 2$ cannot be described by a unified power law in the energy range 0.1–10^3 TeV. © *2001 MAIK "Nauka/Interperiodica".*

PACS numbers: 98.70.Sa; 95.85.Ry; 96.40.De

In his report at the 26th International Cosmic Ray Conference, S. Yoshida formulated the basic characteristics of the energy spectrum of galactic cosmic rays (GCRs) as follows: "Energy spectrum of cosmic rays is well described by three-knee power-law dependence. The first knee is observed for energies ~3×10^{15} eV, where the spectral index changes from ~2.7 to ~3. … At present, it is reliably (*underlined by us*) established that all spectral components obey the power law without knees, and no tendency toward sharpening is observed at least below 10 TeV" [1]. In quantitative terms, this definition of the GCR spectrum reads, $I_0(E) \sim E^{-\beta_0}$, and all components are described by the same law at least up to $E \sim 10^3$ TeV.

The spectrum characteristic presented in [1] is based on the all-particle spectrum observed in [2], from which it follows that $\beta_0 = 2.65 \pm 0.05$ and that all nuclei with $Z \geq 2$ have the same index at least up to $E = 10$–20 TeV. The proton spectrum is well known up to $E \cong 1$ TeV. For higher energies, only two works are known [3, 4] which are consistent with each other in the energy range $E =$ 20–30 TeV [5]. There is no consensus on the proton spectrum in the range 1–20 TeV.

Let us consider the experimental results which are sensitive to the spectrum of primary particles.

(i) For $E \geq 10$ TeV, the ratio of proton flux to helium nucleus flux is $I_p/I_{\mathrm{He}} = 1.02 \pm 0.35$ [6] and 0.77 ± 0.35 [7]; i.e., the mean value is 0.9 ± 0.25. For $E < 1$ TeV, $I_p/I_{\mathrm{He}} = 2.15 \pm 0.1$. If the spectral index is the same for all components, then the ratio $I_p/I_{\mathrm{He}} = \mathrm{const} = 2.15$ cannot be equal to 0.9 for $E > 10$ TeV.

(ii) Direct measurements of the proton spectrum for $E \geq 20$ TeV give spectral indices $\beta_p = 3.05 \pm 0.19$ [3] and 3.17 ± 0.19 [4]. The mean value is $\beta_p = 3.11 \pm 0.14$. For the spectral index $\beta_0 = 2.65 \pm 0.05$ of all particle fluxes in galactic cosmic rays in the interval $0.1 \leq E \leq 10^3$ TeV, $\beta_p = 3.11$ is impossible.

(iii) The GCR all-particle spectrum has a spectral index $\beta_0 = 2.65 \pm 0.05$ in the ranges $E < 1$ TeV and $E >$ 5 TeV. In the range $1 < E < 5$ TeV, $\beta_0 = 2.89$ [8], 2.79 [9], and 2.81 [10], with the mean value $\beta_0 = 2.83 \pm 0.03$. For $\beta_0 =$ const in the range 0.1–10^3 TeV, β_0 cannot change by 0.18 in a narrow energy.

(iv) The quantity $E^{2.6}I_0$, where I_0 is the flux of all particles with energy E, changes from 0.256 $\mathrm{m^{-2}\,s^{-1}\,sr^{-1}\,TeV^{1.6}}$ in the range $E < 1$ TeV to (0.149 ± 0.003) $\mathrm{m^{-2}\,s^{-1}\,sr^{-1}\,TeV^{1.6}}$ in the range $E \geq 10$ TeV [9, 11]; i.e., a step is observed in the all-particle spectrum. No such step can occur if $\beta_0 =$ const in the interval 0.1–10^3 TeV.

(v) At mountain altitudes, the spectral index is $\beta_s = 3.38 \pm 0.08$ [12–14] for single hadrons and $\beta_h = 2.95 \pm 0.05$ for all hadrons; i.e., $\beta_s - \beta_h = 0.43 \pm 0.1$. This is impossible if $\beta_0 =$ const, which is equivalent to the identical spectral indices of all components, $\beta_s - \beta_h = 0$.

(vi) At a depth of 60 g/cm^2 of the residual atmosphere, the spectrum of gamma-ray quanta with energies $E_\gamma > 3$ TeV has a spectral index $\beta_\gamma = 2.9 \pm 0.09$ [15]. This value is inconsistent with the spectral index $\beta_0 = 2.65 \pm 0.05$ of GCRs.

(vii) The vertical muon flux for $E_\mu > 1$ TeV has a spectral index 3.75 [16]. This contradicts the value $\beta_0 = 2.65$.

The above-listed characteristics of cosmic rays contradict the GCR spectrum with $\beta_0 =$ const in the range $0.1 < E < 10^3$ TeV. To eliminate these discrepancies, we

Table 1

E_m, TeV	1	3	5	10	15	Minimum β_p value
β_p	2.79	2.79	2.79	2.80	2.80	2.79
β_p	–	3.04	3.08	3.24	–	3.04 ± 0.17

assume that the GCR flux consists of two components. The first component consists of the nuclei with $Z \geq 2$ and has a constant spectral index $\beta_Z = 2.65 \pm 0.05$ over the entire interval $0.1 \leq E \leq 10^3$ TeV. The second component consists of protons, whose spectral index β_p in the range $E \geq 1$ TeV will be determined independently for each of the above-listed items. As a result, it will be established whether the entire proton spectrum can be assigned a unique β_p value that describes all the phenomena considered.

First of all, we note that, within one order of magnitude (the usual accuracy in measuring the cosmic ray spectrum), the sum of two power-law spectra with indices β_1 and β_2 is well approximated by one exponential function with index $\beta = (A\beta_1 + B\beta_2)/(A + B)$, where A and B are the intensities of the respective components at the minimal energy E_m in the spectrum of interest.

(i) Let $I_p(E) = CE^{-\beta_p}$ and $I_{He}(E) = DE^{-\beta_Z}$ in the range $E \geq 0.4$ TeV; then $I_p/I_{He} = (C/D)E^{-(\beta_p - \beta_Z)}$. Taking this ratio at $E = 0.4$ and 10 TeV, we obtain $(2.15 \pm 0.1)/(0.9 \pm 0.25) = (10/0.4)^{\beta_p - \beta_Z}$, from which one has $\beta_p = 2.92 \pm 0.10$.

(ii) In this case, direct measurements give $\beta_p = 3.11 \pm 0.14$.

(iii) Direct measurements of the all-particles spectrum gave $\beta_0 = 2.83 \pm 0.03$ and 2.65 ± 0.05 in and beyond the interval $0.4 < E < 4$ TeV, respectively. Therefore, $2.83 \pm 0.03 = \beta_0 I_p/I_0 + \beta_Z I_Z/I_0$, where I_p/I_0 and I_Z/I_0 are, respectively, the fractions of protons and nuclei with $Z \geq 2$ in the total GCR flux immediately below the step. In our case, $I_Z/I_0 = (0.149 \pm 0.003)/0.256 = 0.58 \pm 0.01$ and $I_p/I_0 = 0.42 \pm 0.01$. Therefore, $\beta_p = 3.07 \pm 0.10$.

(iv) If $E^{\beta_0} I_0(E) = A$ and B for $E < E_1$ and $E > E_2$, respectively, and $I_0(E) \sim E^{-\beta}$ in the interval $E_1 \leq E \leq E_2$, then the minimal β value is

$$\beta_{min} = \frac{\ln(I_0(E_1)/I_0(E_2))}{\ln(E_2/E_1)} = \beta_0 + \frac{\ln(A/B)}{\ln(E_2/E_1)}.$$

In our case, $A = 0.256$, $B = 0.149$, $E_2/E_1 = 10$, and $\beta_0 = 2.65 \pm 0.05$, so that $\beta_{min} = 2.89 \pm 0.05$.

The spectrum $I_0(E)$ is formed by two fluxes: the proton flux with spectral index β_p and intensity $(A - B)E_1^{-\beta_p}$ at E_1 and the nuclear flux with spectral index β_Z and intensity $BE_1^{-\beta_Z}$ at E_1. Therefore,

$$\beta_{min} = \frac{\beta_p(A - B) + \beta_Z B E_1^{(\beta_p - \beta_Z)}}{(A - B) + BE_1^{(\beta_p - \beta_Z)}}.$$

Since $E_1 = 1$ TeV, one has

$$\beta_{min} = \frac{\beta_p(A - B) + \beta_Z B}{A},$$

so that $\beta_p = 3.27 \pm 0.21$.

(v) The spectrum of single hadrons in the atmosphere at a depth of X g/cm^2 is predominantly formed by the primary protons passing through the atmosphere without interaction. Therefore, the spectral index of this spectrum is $\beta_s = \beta_p + kX/\lambda_0$ if the cross section for inelastic interaction of protons has the form $\sigma^{in} = \sigma_0[1 + k\ln(E/E_0)]$. The spectral index of all hadrons is $\beta_h = \beta_0 + kX/L_0$, where λ_0 and L_0 are, respectively, the mean free paths for interaction and absorption in the atmosphere at $E = E_0$. In our case, $\beta_s = 3.38 \pm 0.08$, $\beta_h = 2.95 \pm 0.05$, $X = 670$ g/cm^2, $\lambda_0 \sim 80$ g/cm^2, and $L_0 \sim 110$ g/cm^2. It follows from the difference $\beta_s - \beta_h = (\beta_p - \beta_0) + (\beta_h - \beta_0)(L_0/\lambda_0 - 1)$ that $\beta_p = \beta_0 + (\beta_{01} - \beta_h) - (\beta_h - \beta_0)(L_0/\lambda_0 - 1)$. Substituting the values of β_s, β_h, β_0, and L_0/λ_0, we obtain $\beta_p = 2.98 \pm 0.1$.

(vi) and (vii) If the spectra of secondary particles (muons with $E_\mu > 1$ TeV and gamma-ray quanta with $E_\gamma > 3$ TeV) are not distorted by the secondary interactions, they have the power-law form, similar to the power law for the primary particles. Because muons and gamma-ray quanta are produced by protons with spectrum $I_p(E) = I_p^0 E^{-\beta_p}$ and intranuclear neutrons with spectrum $I_n(E) = I_n^0 E^{-\beta_Z}$, the spectrum of secondary particles has the form $I_{sc}(E) = K(I_p^0 E^{-\beta_p} + I_n^0 E^{-\beta_Z}) \sim E^{-\beta}$.

In our case,

$$\beta = \frac{\beta_p + C\beta_Z E_m^{(\beta_p - \beta_Z)}}{1 + CE_m^{(\beta_p - \beta_Z)}}, \quad (1)$$

where $C = I_n^0/I_p^0 = 0.35$. The β value is taken from the experimental data and β_p is determined from Eq. (1) for different E_m values. In the experiments with muons and gamma-ray quanta, $\beta = 2.75$ and 2.9 ± 0.09, respectively. Table 1 presents the β_p values obtained for different E_m with β = (upper row) 2.75 and (lower row) 2.9 ± 0.09.

Thus, the resulting seven β_p values extracted from more than 12 different experiments, carried out by different methods and by different authors with approximately the same error ~ 0.1, can be averaged. The corresponding mean value is $\langle\beta_p\rangle = 3.03 \pm 0.06$ and $\sigma =$

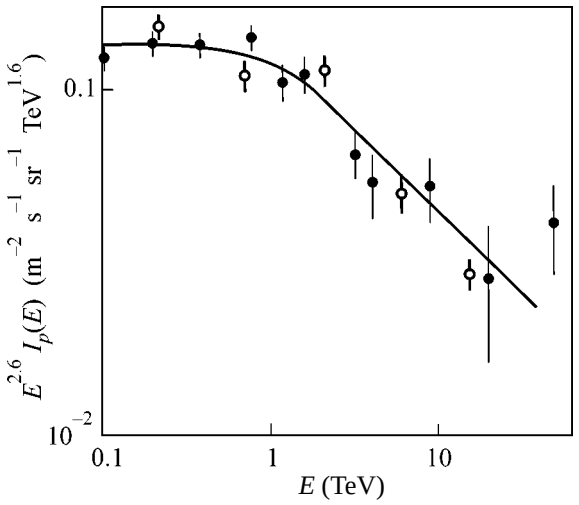

Proton spectrum (open circles) from direct measurements and (closed circles) as the difference between the fluxes of all particles and nuclei with $Z \geq 2$ [11].

0.1; i.e., σ is close to the error of individual determination of β_p.

Thus, we obtain the following answer to the question formulated above: the proton spectrum in energy range $E > 1$ TeV must have the spectral index $\beta_p \cong 3$, which differs considerably from $\beta_p = 2.65$ in the range $E < 1$ TeV. Only in this case can many experimental results be explained. In other words, the predicted proton spectrum must have a knee in the range $\ll 10$ TeV, where the spectral index changes from 2.65 to 3.

We now analyze what information about the proton spectra in the range $E > 1$ TeV can be extracted from the available balloon and satellite measurements.

All proton spectra that have already been reported for the energy range $E \geq 5$ TeV can be represented as $I_p(E) = CE^{-\beta_p}$. Table 2 presents the corresponding β_p values. N_0 is the total number of protons used to obtain the spectrum in this work and $E_{\min}$ is the minimal proton energy after which the spectrum presented in this work is applicable.

Table 2

Authors	Year of publication	β_p	$E_{\min}$, TeV	N_0
Ya. Kawamura *et al.* [17]	1989	2.88	5	90*
N.L. Grigorov [7]	1990	3.11 ± 0.15	4	90
I. Ivanenko *et al.* [18]	1993	2.85 ± 0.14	5	160*
V. Zatsepin *et al.* [3]	1994	3.14 ± 0.08	10	602
M.L. Cherry *et al.* [4]	1997	2.80	6	656

* Estimated from the data in the cited reference.

The mean spectral index in Table 2 is $\beta_p = 2.96 \pm 0.07$. The mean value weighted with N_0 is $\beta_p = 2.96 \pm 0.03$. For the data reported before 1995, the mean value is $\beta_p = 3.00 \pm 0.08$. Thus, the direct measurements give a value of $\beta_p \cong 3.0$ for the proton spectral index in the range $E \geq 5$ TeV, which corroborates the above prediction. The figure shows the similar spectrum obtained in the direct measurements covering the energy range 0.1–10 TeV [8, 11].

Therefore, the GCR spectrum, being the sum of a power-law spectrum of nuclei and the proton spectrum with a knee at $E \cong 1$ TeV, cannot be described by a pure power-law dependence and, hence, cannot be approximated by the exponential function with a single index $\beta_0 = 2.65$.

Note that the form of proton spectrum could be predicted even 10–15 years ago, because many experimental data used for this prediction were available before 1985–1990. If this prediction had been made 10–15 years ago, the spectrum shown in the figure would be received as obvious and not as a foreign phenomenon breaking the "harmonious" pattern of identical spectra of all cosmic ray components.

REFERENCES

1. S. Yoshida, in *Proceedings of the 26th International Cosmic Ray Conference, 1999*, Rapporteur paper.
2. T. Shibata, in *Proceedings of the 24th International Cosmic Ray Conference, 1995*, Rapporteur paper.
3. V. I. Zatsepin, T. V. Lazareva, G. P. Sazhina, *et al.*, Yad. Fiz. **57**, 684 (1994) [Phys. At. Nucl. **57**, 645 (1994)].
4. M. L. Cherry (JACEE Collab.), in *Proceedings of the 25th International Cosmic Ray Conference, 1997*, Vol. 4, p. 1.
5. N. L. Grigorov and E. D. Tolstaya, in *Proceedings of the 26th International Cosmic Ray Conference, 1999*, Vol. 3, p. 183.
6. K. Asakimori, T. H. Burnett, and M. L. Cherry, in *Proceedings of the 23rd International Cosmic Ray Conference, 1993*, Vol. 2, p. 21.
7. N. L. Grigorov, Yad. Fiz. **51**, 157 (1990) [Sov. J. Nucl. Phys. **51**, 99 (1990)].
8. N. L. Grigorov, V. E. Nesterov, I. D. Rapoport, *et al.*, Yad. Fiz. **11**, 1058 (1970) [Sov. J. Nucl. Phys. **11**, 588 (1970)].
9. N. L. Grigorov, V. E. Nesterov, and I. D. Rappoport, in *Space Research XII* (Akademic, Berlin, 1972), p. 1617.
10. J. Adams, J. Li, V. I. Zatsepin, and M. I. Panasyuk, Izv. Akad. Nauk, Ser. Fiz. **61**, 1181 (1997).

11. N. L. Grigorov, Kosm. Issled. **33**, 339 (1995).
12. Kh. P. Babayan, N. L. Grigorov, and Ch. A. Tret'yakova, Izv. Akad. Nauk SSSR, Ser. Fiz. **29**, 1648 (1965).
13. C. Aguirre, K. Kamata, *et al.*, Nuovo Cimento **5**, 279 (1975).
14. R. A. Nam, S. I. Nikol'skiĭ, and V. P. Pavlyuchenko, Tr. Fiz. Inst. Akad. Nauk SSSR **109**, 153 (1979).
15. M. A. Ivanova, K. V. Mandritskaya, E. A. Osipova, *et al.*, in *Proceedings of the 16th International Cosmic Ray Conference, 1979*, Vol. 7, p. 111.
16. O. G. Ryazhgkaya, in *Proceedings of the 24th International Cosmic Ray Conference, 1995*, Rapporteur paper.
17. Ya. Kawamura, H. Matsutani, and H. Nanjyo, Phys. Rev. D **40**, 729 (1989).
18. I. Ivanenko, V. Shestoperov, and I. Rappoport, in *Proceedings of the 23rd International Cosmic Ray Conference, 1993*, Vol. 2, p. 17.

Translated by R. Tyapaev

JETP Letters, Vol. 74, No. 3, 2001, pp. 133–138. Translated from Pis'ma v Zhurnal Éksperimental'noĭ i Teoreticheskoĭ Fiziki, Vol. 74, No. 3, 2001, pp. 151–156.

Schwinger Mechanism of Electron–Positron Pair Production by the Field of Optical and X-ray Lasers in Vacuum

V. S. Popov

Institute of Theoretical and Experimental Physics, ul. Bol'shaya Cheremushkinskaya 25, Moscow, 117259 Russia
e-mail: marina@vxitep.itep.ru

Received June 28, 2001

The probability W of e^+e^--pair production in vacuum by an intense time-varying electric field created by optical or X-ray laser is calculated. Two characteristic regions $\gamma \ll 1$ and $\gamma \gg 1$ of adiabaticity parameter γ are considered. With an increase in γ and on passing from monochromatic radiation to a finite laser pulse, the probability W increases sharply (for the same field intensity). The dependence of the probability W and the electron and positron momentum spectrum on the pulse shape is discussed (the dynamic Schwinger effect). © *2001 MAIK "Nauka/Interperiodica".*

PACS numbers: 12.20.Ds

1. Quantum electrodynamics predicts that a strong electric field can induce electron–positron pair production in vacuum [1]. Being first considered for a static field, this nonlinear effect was also explored theoretically for time-varying electric fields. In particular, the spatially uniform field

$$\mathscr{E}(t') = \{F\varphi(t), 0, 0\}, \quad \mathbf{B}(t) = 0, \quad t = \omega t', \quad (1)$$

was studied for $\varphi(t) = \cos t$ [2–6]. Here, t' and t are the time and the dimensionless time, respectively; F and ω are the amplitude and characteristic frequency of the electric field; and the function $\varphi(t)$ specifies the shape of a laser pulse. Such a field can occur in an antinode of a standing light wave arising upon the superposition of two coherent laser beams [4, 7]. In what follows, we will assume that φ is an analytic function of t^2 and $|\varphi(t)| \le \varphi(0) = 1$ for real t values; i.e., the field is maximal at $t = 0$, when an electron and a positron emerge from under a barrier [3].

This process, the so-called Schwinger pair-production mechanism, is of fundamental importance for QED and quantum field theory in general.[1] However, estimates [4, 11, 12] showed that this process could not be observed experimentally with lasers available at that time. For this reason, studies [1–6] were regarded as being of pure theoretical interest for QED. At present, the situation is changing because the powers of optical and infrared lasers increased by many orders of magnitude [13, 14], and the projects of developing free-electron X-ray lasers at the DESY electron–positron linear collider TESLA (and at SLAC) were proposed to obtain coherent photon beams with energies of about several kiloelectronvolts [7, 15]. In light of these circumstances and new experimental possibilities, it is necessary to examine in more detail the theory of the Schwinger effect, to which recent Ringwald's work [7] was devoted.

In this paper, I continue to discuss these problems. The following notation is used: $\epsilon = F/F_{cr}$ is the reduced electric field, $F_{cr} = m^2c^3/e\hbar \approx 1.32 \times 10^{16}$ V/cm is the critical or Schwinger field in QED [1], $\alpha = e^2/\hbar c = 1/137$, $K_0 = 2mc^2/\hbar\omega = \lambda/\pi\lambda\!\!\!^{-}_e$ is the multiphoton parameter, λ is the laser wavelength, $\lambda\!\!\!^{-}_e = \hbar/mc = 386$ fm, and further, as a rule, $\hbar = c = 1$.

2. Let us first consider a monochromatic laser field with $\varphi(t) = \cos t$. Using the imaginary time method for the description of the subbarrier motion of a relativistic electron [3, 4], one can show that the probability of production of a pair with $e^\pm$ momenta $\pm\mathbf{p}$ in vacuum, to a preexponential factor, is

$$w(\mathbf{p}) = d^3W/d^3p \propto$$
$$\propto \exp\left\{-\frac{\pi}{\epsilon}\left[\tilde{g}(\gamma) + \tilde{b}_1(\gamma)\frac{p_\parallel^2}{m^2} + \tilde{b}_2(\gamma)\frac{p_\perp^2}{m^2}\right]\right\}, \quad (2)$$

where the adiabaticity parameter γ is

$$\gamma = \omega/\omega_t = mc\omega/eF = 2/K_0\epsilon, \quad (3)$$

ω_t is the electron tunneling frequency through the $2mc^2$ gap between the lower and upper continua. The function $\tilde{g}(\gamma)$ and the coefficients $\tilde{b}_{1,2}(\gamma)$ of the pulse spectrum depend strongly on the pulse shape at $\gamma \gtrsim 1$. The tilde functions refer to the pair production and differ from the analogous functions g and $b_{1,2}$ appearing in the theory of multiphoton ionization of atoms [16],

[1] Processes similar to the Schwinger pair production occur, e.g., in the theory of quantum evaporation of black holes [8, 9], in consideration of the early stages of universe evolution, in the theory of multiphoton ionization of semiconductors [10], etc.

because the dispersion relations $E(\mathbf{p})$ for a subbarrier electron and, in addition, the orders of magnitude of the parameter γ, are different in these two cases. The total probability W per the invariant Compton 4-volume $\lambda_e^4/c = m^{-4} \approx 7.25 \times 10^{-53}$ cm^3 s is determined by integrating Eq. (2) with respect to d^3p with the inclusion of energy conservation law in n-photon absorption. The resulting formulas (which are rather unwieldy) are presented in [4] and require numerical calculations.

The formulas are considerably simplified for $\gamma \ll 1$ and $\gamma \gg 1$.[2] In the first case (adiabatic region: low frequency ω and strong electric field), the $n\omega$ spectrum is virtually continuous and

$$W = \frac{m^4}{2^{3/2}\pi^4}\epsilon^{5/2}\exp\left\{-\frac{\pi}{\epsilon}\tilde{g}(\gamma)\right\}, \quad (4)$$

$$\tilde{g}(\gamma) = 1 - \frac{1}{8}\gamma^2 + \frac{3}{64}\gamma^4 + \ldots,$$

$$\tilde{b}_1 = \frac{1}{2}\gamma^2\left(1 - \frac{9}{8}\gamma^2 + \ldots\right), \quad (4')$$

$$\tilde{b}_2 = 1 - \frac{1}{4}\gamma^2 + \ldots .$$

Assuming that the maximum electric field F is attained upon focusing laser radiation to the volume $\Delta V = \lambda^3$ (diffraction limit) and that the pulse duration is T, one finds the following expression for the total number of e^+e^- pairs produced in vacuum:

$$N(T) = 0.354K_0^4\epsilon^{5/2}\exp\left\{-\frac{\pi}{e}\left[1 - \frac{1}{2(K_0\epsilon)^2}\right]\right\}N', \quad (5)$$

where $N' = \omega T/2\pi$ is the number of field periods in the laser pulse.

In the other limiting case $\gamma \gg 1$, one has

$$\tilde{g}(\gamma) = \frac{4}{\pi\gamma}\left[\ln\gamma + 0.386 + \frac{\ln\gamma}{4\gamma^2} + \ldots\right],$$

$$\tilde{b}_1(\gamma) \approx \tilde{b}_2(\gamma) \approx \frac{2\ln\gamma}{\pi\gamma},$$

and the pair-production probability is represented as the following sum of the probabilities of n-photon processes:

$$W = \sum_n w_n, \quad w_n = \frac{2}{\pi^3}m^4K_0^{-5/2}\left(\frac{e}{4\gamma}\right)^{2n}q(n - K_0), \quad (6)$$

where $n > K_0 = 2m/\omega$ and

$$q(x) = \frac{1}{2}e^{-2x}\int_0^{2x} e^t t^{-1/2}dt \approx \begin{cases} \sqrt{2x}, & x \longrightarrow 0 \\ (8x)^{-1/2}, & x \longrightarrow \infty. \end{cases} \quad (6')$$

In this case, the probabilities w_n rapidly decrease with an increase in n and Eq. (6) yields the estimates

$$W \approx \frac{m^4}{2^{3/2}\pi^3}\left(\frac{\omega}{m}\right)^{5/2}(4\gamma/e)^{-2K_0}, \quad (7)$$

$$N(T) \approx 2\pi K_0^{3/2}\exp\{-2K_0\ln(4\gamma/e)\}N'.$$

The comparison of Eq. (4) with Eq. (7) indicates that the pair-production probability for $\gamma \gg 1$ exceeds that in the adiabatic region (for the same electric field F) by many orders of magnitude.[3]

Figure 1 shows the values of a reduced electric field corresponding to the production of one electron–positron pair in the volume λ^3 for several pulse durations from $T = 2\pi/\omega$ (one field period) to $T = 1$ s. These fields are rather close to each other for optical lasers, but the difference between them increases with frequency ω if $\hbar\omega \gtrsim 1$ keV (dashed curve corresponds to $\gamma = 1$).

Figures 2 and 3 show the total number of pairs produced in the volume λ^3 as functions of, respectively, the reduced electric field ϵ and electric field F for different pulse durations T. The curve numbers in Fig. 2 correspond to the photon energies given in the table. The solid curves are for an ultrashort pulse with $T = 2\pi/\omega$ (one period) and the dashed curves correspond to the pulse duration $T = 1$ ps. The latter value is chosen because the maximal fields are attained in experiments with pulsed lasers and $T \lesssim 1$ ps [13, 14]. As the field F increases, the number of pairs increases so rapidly (especially for $\lambda \gtrsim 1$ μm) that this process can be treated as a laser vacuum breakdown. For a fixed field F, the number N of pairs also increases with wavelength λ. This is explained by the fact that N is proportional to the volume of the focusing region. Because of the exponential field dependence of N, an increase in the pulse duration by many orders of magnitude from one period to even 1 s leads (Fig. 3) to a comparatively small shift of the $N = N(\epsilon, \omega)$ curves toward weaker fields (for optical lasers). A decrease in the lowest required field is more pronounced for X-ray lasers.

The table presents the Schwinger effect threshold, i.e., the field F_{th} necessary for producing one electron–positron pair in one field period. For optical lasers, this threshold is attained at $F = (0.7–1.0) \times 10^{15}$ V/cm, which is smaller than the critical field F_{cr} by one and a half orders of magnitude (for $F \gtrsim F_{cr}$, the back action of the produced particles on the external field should be

[2] See Eqs. (20), (21), and (A.12) in [4] for $\gamma \ll 1$ and $\gamma \gg 1$, respectively. The formulas used by Ringwald {see Eq. (18) in [7]} coincide with Eq. (4) for $\gamma \ll 1$ and, in the case of $\gamma \gg 1$, differ from Eq. (7) only in the numerical factor $2/\sqrt{\pi} \approx 1.13$, which is immaterial for further estimates.

[3] The same relationship takes place for the multiphoton ionization of atoms [10] and, in general, for particle tunneling through a barrier oscillating with frequency $\omega \gg \omega_t$.

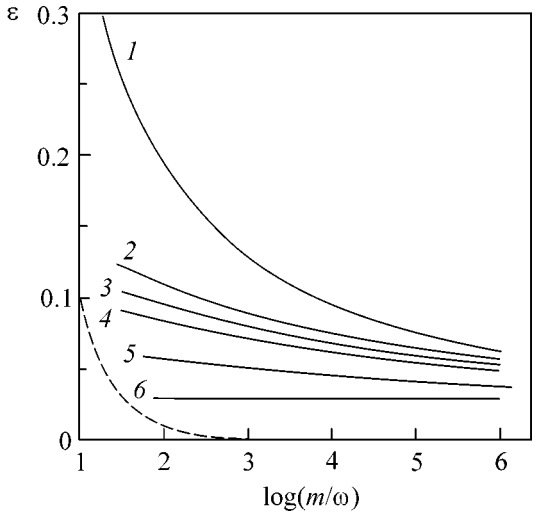

Fig. 1. The reduced electric field $\epsilon = F/F_{cr}$ necessary for the production of one electron–positron pair in the volume λ^3 in time T = (*1*) $2\pi/\omega$ (one field period), (*2*) 10^{-12}, (*3*) 10^{-10}, (*4*) 10^{-8}, and (*5*) 1 s. Curve *6* is for $\Delta V = 1$ cm^3 and $T = 1$ s; it corresponds to $\epsilon \approx 0.0297$. The adiabaticity region is above the dashed curve for which $\gamma = 1$.

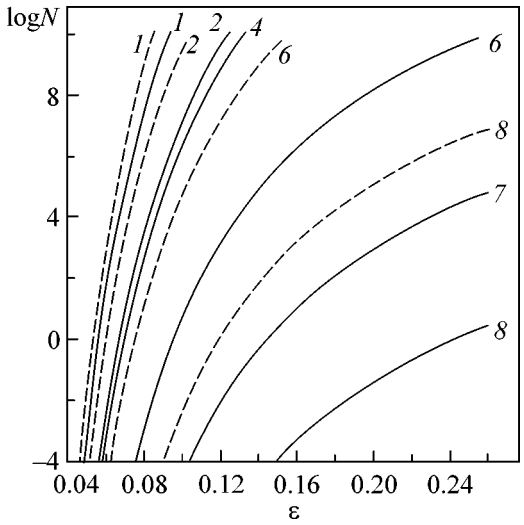

Fig. 2. The number of e^+e^- pairs produced in the volume λ^3 in (solid curves) one field period and (dashed curves) 1 ps. The curve numbers correspond to the energies from the table.

taken into account, but this effect is negligible in the field range under investigation).

For $\gamma \gg 1$, the dependence of $N_{e^+e^-}$ on the field amplitude has the power-law, $N_{e^+e^-} \propto F^{2K_0}$, rather than the exponential character, which corresponds to the perturbation theory of high order (K_0) in an external field. In this case, Eq. (7) gives the values that exceed the extrapolation by adiabatic Eq. (5) by many orders of magnitude. The ratio of the corresponding values is $\rho \sim (K_0\epsilon)^{2K_0}\exp(\pi/\epsilon)$, which yields $\rho \sim 4 \times 10^{10}$ for $K_0 = 5$ and $\epsilon = 0.1$, $\rho \sim 10^{21}$ for $K_0 = 10$ and $\epsilon = 0.05$, $\rho \sim 10^{35}$ for $K_0 = 10$ and $\epsilon = 0.03$, etc. Therefore, it is easier to observe the Schwinger effect in the region $\gamma \gtrsim 1$ (for a given F value), which is understood from the physical considerations: in this case, an external field $F\cos\omega t'$ reverses its direction many times during the tunneling, resulting in a decrease in the effective barrier width and, therefore, a sharp increase in the barrier transmittivity (this is clearly seen in the imaginary time method [3]).

Unfortunately, the $\gamma \gg 1$ regime is realized only in weak fields, where the probability W is extremely low. As in the case of multiphoton ionization of atoms, the values $K_0 \leq 10$–15 are necessary in this case, which corresponds to $\hbar\omega \gtrsim 100$ keV. The fabrication of such γ lasers is possible only in the far distant future.

Recently, considerable efforts have gone into the design of free electron lasers (see, e.g., [15, 18]). Ringwald [7] pointed out that, if these lasers can operate in X-ray range and their radiation can be focused to a volume of about λ^3, the minimal laser power P necessary for observing the Schwinger effect will decrease considerably. In particular, the power $P_{min} \approx 4 \times 10^{16}$ W is

The parameters of some lasers

No.	λ	ħω	K_0	F_{th}	Laser type
1	10.6 μm	0.117 eV	8.74(6)	0.74	CO_2 laser [17]
2	1.064 μm	1.165 eV	8.77(5)	0.87	YAG:Nd [17]
3	0.785 μm	1.58 eV	6.47(5)	0.90	Ti:sapphire
4	0.69 μm	1.8 eV	5.69(5)	0.91	Ruby
5	109 nm	11.4 eV	8.98(4)	1.07	Free electron laser
6	25 nm	50 eV	2.04(4)	1.26	–
7	1.24 nm	1 keV	1.02(3)	1.89	X-ray laser [7, 15]
8	0.1 nm	12.4 keV	82.4	3.15	"

λ is the wavelength, K_0 is the multiphoton parameter, and F_{th} is the threshold electric field in 10^{15} V/cm; $a(b) \equiv a \times 10^b$.

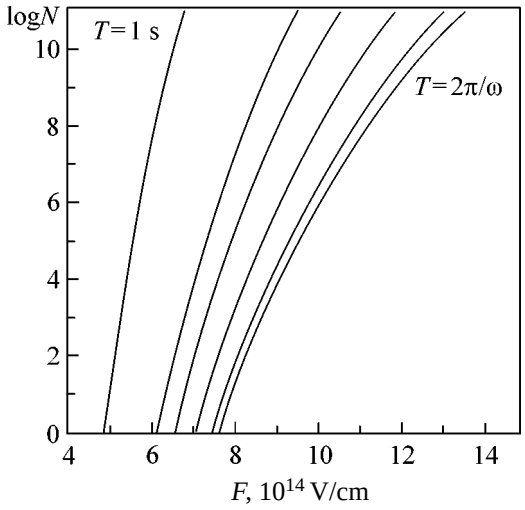

Fig. 3. The field dependence of the number of electron–position pairs produced by the CO_2-laser pulse of duration $T = 2\pi/\omega$ = (from right to left) 0.035, 0.01, 1, 100 ps, 10 ns, and 1 s.

required to produce one e^+e^- pair at $\lambda = 0.1$ nm and pulse duration $T = 0.1$ ps. Such powers have long been achieved in laser technology in the optical range [14], but the possibilities of constructing lasers with $\hbar\omega \sim 10$ keV and focusing a beam in X-ray optics are still under study [7].

3. Optical electromagnetic fields of highest intensities are created by compressing a laser pulse whose duration is comparable with the optical period and shape is far from an ideal sinusoid [13, 16, 19]. The same is likely true for X-ray lasers as well. For this reason, we consider the influence of pulse shortening on the probability of the Schwinger effect.

The momentum spectrum of $e^{\pm}$ produced in vacuum by electric field (1) is determined by Eq. (2), where

$$\tilde{g}(\gamma) = \frac{4}{\pi}\int_0^1 \chi(\gamma u)(1-u^2)^{1/2}du, \quad \tilde{b}_1(\gamma) = -\gamma\tilde{b}_2'(\gamma),$$
$$\tilde{b}_2(\gamma) = \frac{2}{\pi}\int_0^1 \chi(\gamma u)(1-u^2)^{-1/2}du, \tag{8}$$

and the function $\chi(u)$ is completely determined by the pulse shape and has the same form as in the theory of multiphoton ionization of atoms [16]. In particular, $\chi(u) = (1+u^2)^{-1/2}$ for monochromatic radiation, $\chi(u) = 1/(1+u^2)$ for the solitonlike pulse $\varphi(t) = 1/\cosh^2 t$, etc.

Using Eq. (8), I calculated the function $\tilde{g}(\gamma)$ and the coefficients $\tilde{b}_{1,2}(\gamma)$ of the momentum spectrum for several pulsed fields. In all cases, the function $\tilde{g}(\gamma)$ decreases monotonically with an increase in the adiabaticity parameter (Fig. 4), and the probability W increases drastically for a given field amplitude F (because $\epsilon \ll 1$) and starts to depend on the pulse shape $\varphi(t)$. It is natural to refer to this phenomenon, arising at frequencies $\omega \gtrsim \omega_t$, as the dynamic Schwinger effect.

Let us consider a modulated electromagnetic pulse with the Gaussian envelope

$$\varphi(t) = \exp(-t^2/2\sigma^2)\cos t. \tag{9}$$

In this case, the function $\chi(u)$ is determined numerically from the equations

$$\chi = \frac{\exp(-\tau^2/2\sigma^2)}{\cosh\tau}, \quad u = \int_0^\tau \exp(t^2/2\sigma^2)\cosh t\,dt, \tag{9'}$$

where τ is a parameter ($0 \le \tau < \infty$). As σ decreases, the pulse shortens; its amplitude decreases by a factor of $\delta \approx \exp(-2\pi^2/\sigma^2)$ in one period. As is seen from Fig. 5, the decrease in the function $\tilde{g}(\gamma)$ entering the exponent begins to be noticeable for $\sigma \sim 5$ and is substantial for $\sigma = 1$. The σ dependence of the coefficients $b_{1,2}(\gamma)$ is negligible for $\sigma \ge 3$, but the momentum spectrum broadens noticeably at $\sigma \sim 1$. The probability W for $\sigma \gtrsim 3$ can be calculated by the formulas for monochromatic radiation (as it was done above).

The indicated effects are manifested in full measure in the region $\gamma \gtrsim 1$, whereas the dependence on the pulse shape for $\gamma \ll 1$ has a universal form

$$w(\mathbf{p}) \approx \exp\left\{-\left[\frac{\pi}{\epsilon}\left(1-\frac{1}{8}\tilde{\gamma}^2\right)+\frac{1}{eF}(\tilde{\gamma}^2 p_\parallel^2 + p_\perp^2)\right]\right\}, \tag{10}$$

where $\tilde{\gamma} = \sqrt{a_2}\gamma$ and $a_2 = -\varphi''(0)$ is the curvature of the pulse near its peak. In this case, $p_\perp \sim \Delta p_\perp \sim \sqrt{eF} = m\sqrt{\epsilon}$ and $\Delta p_\parallel \sim \gamma^{-1}\Delta p_\perp \sim mK_0\epsilon^{3/2}$. The transverse $e^{\pm}$ momentum remains nonrelativistic, but the longitudinal momentum is $p_\parallel \sim 1/\gamma \gtrsim m$ if $K_0^{-3/2} \ll \epsilon \ll 1$.

Figure 4 demonstrates that, on passing from the monochromatic radiation (curve *1*) to variously shaped pulsed fields concentrated in a finite time interval, the function $\tilde{g}(\gamma)$ decreases substantially if $\gamma \gtrsim 1$. Therefore, pulse shortening facilitates experimental observation of the Schwinger effect.

4. For some cases, the quantities appearing in Eq. (2) can be calculated analytically by Eq. (8). In particular, for

$$\chi(u) = (1+u^2)^{-a}, \quad a > 0, \tag{11}$$

one obtains

$$\tilde{g}(\gamma) = F(1/2, a; 2; -\gamma^2),$$
$$\tilde{b}_1(\gamma) = a\gamma^2 F(3/2, a+1; 2; -\gamma^2), \tag{12}$$
$$\tilde{b}_2(\gamma) = F(1/2, a; 1; -\gamma^2),$$

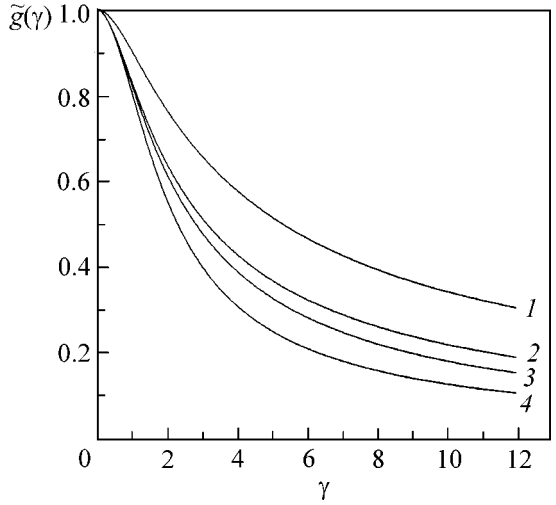

Fig. 4. Dynamic Schwinger effect: the function $\tilde{g}(\gamma)$ for different values of the adiabaticity parameter γ. Electric-field shape $\varphi(t)$ = (*1*) cos*t*, (*2*) $\exp(-t^2)$, (*3*) $1/\cosh^2 t$, and (*4*) $1/(1+t^2)$.

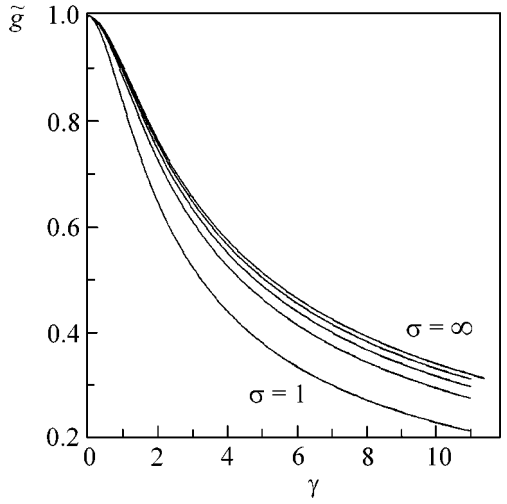

Fig. 5. The same as in Fig. 4, but for the modulated pulse shape (9) with the parameter σ = (from bottom to top) 1, 2, 3, 5, and ∞.

where $F(\ldots) \equiv_2 F_1(\ldots)$ is the Gauss hypergeometric function. The parameters a = 1/2, 1, and 3/2 correspond to the field shapes $\varphi(t) = \cos t$, $1/\cosh^2 t$, and $(1+t^2)^{-3/2}$, respectively. In the general case,

$$\varphi(t) = 1 - at^2 + \frac{1}{6}(7a^2 - 3a)t^4 + \ldots, \quad t \longrightarrow 0 \quad (13)$$

and

$$\varphi(t) \approx \begin{cases} [2(a-1)t]^{-a/(a-1)}, & a > 1 \\ 4\exp(-2t), & a = 1 \end{cases} \quad (13')$$

for $t \longrightarrow \infty$. Expressing the complete elliptic integrals through the hypergeometric function, one can easily find that Eq. (12) for a = 1/2 is consistent with the formulas previously obtained for monochromatic light [2, 3]. For a = 1, i.e., for

$$\varphi(t) = 1/\cosh^2 t, \quad (14)$$

the functions $\tilde{g}$ and others have a highly simple form

$$\tilde{g}(\gamma) = \frac{2}{1+\sqrt{1+\gamma^2}}, \quad \tilde{b}_1(\gamma) = \frac{\gamma^2}{(1+\gamma^2)^{3/2}}, \quad \tilde{b}_2(\gamma) = \frac{1}{\sqrt{1+\gamma^2}}. \quad (15)$$

At the same time, the Dirac and Klein–Gordon equations can be solved exactly for a solitonlike pulse (14),[4] and the probability of producing the e^+e^- pair in the quantum state $(\mathbf{p}, \sigma)$ is [20, 21]

$$w_{\mathbf{p}\sigma} = \frac{\cosh 2\pi\nu - \cosh\pi(\nu_+ - \nu_-)}{\cosh\pi(\nu_+ - \nu_-) - \cosh 2\pi\nu}, \quad \nu_\pm = \frac{E_\pm}{\omega}, \quad (16)$$

where s = 1/2 is the spin, $E_\pm = \sqrt{m^2 + p_\perp^2 + (p_\parallel \pm q/2)^2}$, $\nu = q/2\omega$, and $q = 2eF/\omega$ is the momentum transfer to an electron in time from $t = -\infty$ to $t = +\infty$. In the quasiclassical limit, one has $\nu_\pm \gg 1$ and $\nu_+ + \nu_- \gg 2\nu \gg |\nu_+ - \nu_-|$; under these conditions, Eq. (16) differs from quasiclassical Eqs. (2) and (15) only in the preexponential factor

$$P = [1 - \exp(-2\pi\nu)]^2 \approx 1 - 2\exp(-\pi K_0/\gamma), \quad (17)$$

which is unity within the exponential accuracy if $\gamma \ll \pi K_0$ (this condition is practically always satisfied). This demonstrates that the accuracy of the quasiclassical imaginary time method [3, 4] is quite satisfactory in the problem under consideration.

5. At present, QED is in excellent agreement with experimental results. For the most crucial case of anomalous magnetic moments of e^- and μ^-, the accuracy achieves 10^{-12}, which corroborates the high-order perturbative calculations up to $(\alpha/\pi)^4$ (see, e.g., [23]). The experimental confirmation of the Schwinger pair-production mechanism in vacuum would mean the verification of the Dirac equation and QED for ultrastrong external fields beyond the perturbation theory. Indeed,

[4] See [20]. As was shown in [21], the determination of the pair-production probability in a uniform electric field reduces to the problem of quantum oscillator with variable frequency. For pulse (14), this is equivalent to the calculation of the coefficient of over-barrier reflection in the Eckart potential [22].

the exponential decrease of probability (4) for $\epsilon \longrightarrow 0$ is closely connected with the factorial-like increase of higher perturbation orders and the divergence of perturbation series in QED (so-called Dyson phenomenon [24]). This nonperturbative effect cannot be obtained by summing any finite number of terms of the perturbation series and, therefore, its observation is of fundamental interest for QED (and quantum field theory). The above calculations demonstrate that, most likely, the Schwinger effect will be discovered with a further increase in power of infrared or optical lasers.

I am grateful to L.B. Okun', who called my attention to work [7], for discussion of the results and useful remarks, to M.I. Vysotskiĭ, V.D. Mur, V.A. Novikov, S.V. Popruzhenko, and Yu.A. Simonov for stimulating discussions, to S.V. Bulanov, A.B. Kaĭdalov, and participants in the ITEP theoretical seminar for discussion of the results, to S.G. Pozdnyakov for continuous assistance in numerical calculations, and to V.A. Gani for help in manuscript preparation. This study was supported in part by the Russian Foundation for Basic Research (project no. 01-02-16850).

REFERENCES

1. J. Schwinger, Phys. Rev. **82**, 664 (1951).
2. E. Brezin and C. Itzykson, Phys. Rev. D **2**, 1191 (1970).
3. V. S. Popov, Pis'ma Zh. Éksp. Teor. Fiz. **13**, 261 (1971) [JETP Lett. **13**, 185 (1971)]; Zh. Éksp. Teor. Fiz. **61**, 1334 (1971) [Sov. Phys. JETP **34**, 709 (1971)].
4. V. S. Popov, Pis'ma Zh. Éksp. Teor. Fiz. **18**, 435 (1973) [JETP Lett. **18**, 255 (1973)]; Yad. Fiz. **19**, 1140 (1974) [Sov. J. Nucl. Phys. **19**, 584 (1974)].
5. N. B. Narozhnyĭ and A. I. Nikishov, Zh. Éksp. Teor. Fiz. **65**, 862 (1973) [Sov. Phys. JETP **38**, 427 (1973)].
6. M. S. Marinov and V. S. Popov, Fortschr. Phys. **25**, 373 (1977).
7. A. Ringwald, Preprint DESY 01-024 (2001); hep-ph/0103185.
8. S. W. Hawking, Commun. Math. Phys. **43**, 199 (1975).
9. K. M. Parikh and F. Wilczek, Phys. Rev. Lett. **85**, 5042 (2000).
10. L. V. Keldysh, Zh. Éksp. Teor. Fiz. **47**, 1945 (1964) [Sov. Phys. JETP **20**, 1307 (1964)].
11. F. V. Bunkin and I. I. Tugov, Dokl. Akad. Nauk SSSR **187**, 541 (1969) [Sov. Phys. Dokl. **14**, 678 (1969)].
12. G. J. Troup and H. S. Perlman, Phys. Rev. D **6**, 2299 (1972).
13. N. Bloembergen, Rev. Mod. Phys. **71**, S283 (1999).
14. S. V. Bulanov, V. A. Vshivkov, G. I. Dudnikova, *et al.*, Zarubezhn. Radioélektron., No. 2, 3 (2000).
15. CERN Courier **40** (6), 26 (2000); **41** (5), 20 (2001).
16. V. S. Popov, Laser Phys. **10**, 1033 (2000); Pis'ma Zh. Éksp. Teor. Fiz. **73**, 3 (2001) [JETP Lett. **73**, 1 (2001)].
17. O. Svelto, *Principles of Lasers* (Plenum, New York, 1982; Mir, Moscow, 1984).
18. J. Andruszkow *et al.*, Phys. Rev. Lett. **85**, 3825 (2000).
19. L. Keldysh, Multiphoton ionization by avery short pulse (in press).
20. N. B. Narozhnyĭ and A. I. Nikishov, Yad. Fiz. **11**, 1072 (1970) [Sov. J. Nucl. Phys. **11**, 596 (1970)].
21. V. S. Popov, Zh. Éksp. Teor. Fiz. **62**, 1248 (1972) [Sov. Phys. JETP **35**, 659 (1972)].
22. C. Eckart, Phys. Rev. **35**, 1303 (1930).
23. V. W. Hughes and T. Kinoshita, Rev. Mod. Phys. **71**, S133 (1999).
24. F. J. Dyson, Phys. Rev. **85**, 631 (1952).

Translated by R. Tyapaev

JETP Letters, Vol. 74, No. 3, 2001, pp. 139–143. Translated from Pis'ma v Zhurnal Éksperimental'noĭ i Teoreticheskoĭ Fiziki, Vol. 74, No. 3, 2001, pp. 157–161.

Neutrino Mixing and Leptonic *CP* Phase in Neutrino Oscillations

D. A. Ryzhikh* and K. A. Ter-Martirosyan**

Institute of Theoretical and Experimental Physics, ul. Bol'shaya Cheremushkinskaya 25, Moscow, 117259 Russia

** e-mail: ryzhikh@heron.itep.ru*

*** e-mail: termarti@heron.itep.ru*

Received December 15, 2000; in final form, July 2, 2001

Oscillations of the Dirac neutrinos of three generations in vacuum are considered with allowance made for the effect of the *CP*-violating leptonic phase (analogue of the quark *CP* phase) in the lepton mixing matrix. The general formulas for the probabilities of neutrino transition from one sort to another in oscillations are obtained as functions of three mixing angles and the *CP* phase. It is found that the leptonic *CP* phase can, in principle, be reconstructed by measuring the oscillation-averaged probabilities of neutrino transition from one sort to another. The manifestation of the *CP* phase as a deviation of the probabilities of direct processes from those of inverse processes is an effect that is practically unobservable as yet. © *2001 MAIK "Nauka/Interperiodica".*

PACS numbers: 14.60.Pq; 11.30.Er

Rapidly growing interest in neutrino physics has recently been stimulated by new data from facilities at Kamiokande [1], Super-Kamiokande [2], LSND [3], CHOOZ [4], and some others [5, 6]. These data are indicative, directly or indirectly, of the Pontecorvo (vacuum) oscillations [7] of neutrinos of three types, ν_e, ν_μ, and ν_τ. The frequency of these oscillations, i.e., of the $\nu_i \rightleftharpoons \nu_k$ transitions in oscillations, is proportional to $\sin^2\left(\frac{m_3^2 - m_2^2}{4p_\nu}t\right)$, where p_ν is the ultrarelativistic neutrino momentum and $t = L/c$ is the time it takes for a neutrino to run from source to detector (the distance L is called the "base length"). In what follows, we set $c = 1$ for convenience.

The presence of vacuum oscillations means that

(i) similar to quarks, neutrinos produced in decays or collisions have no definite mass [7] but are the superpositions of neutrinos ν_1°, ν_2°, and ν_3°, which have small ($m_i \sim 10^{-2}$–10^{-4} eV) though definite masses [8, 9]:

$$\nu_\alpha(\mathbf{x}, t) = \sum_{i=1}^{3} \hat{V}^l_{\alpha i}\nu_i^\circ(\mathbf{x}, t), \qquad \alpha = e, \mu, \tau; \quad i = 1, 2, 3; \tag{1}$$

(ii) neutrinos of different generations have different masses; i.e., $m_i^2 - m_k^2 \neq 0$.

It is assumed in Eq. (1) that neutrinos ν_i° move with ultrarelativistic energy $E_i = \sqrt{\mathbf{p}_\nu^2 + m_i^2} \simeq |\mathbf{p}_\nu| + m_i^2/2p_\nu$ in a beam along the X axis of their momentum. Therefore, at the detection time $t_0 = L$ we have

$$\nu_i(\mathbf{x}, t) = \nu_i(L, t_0) = \exp(i\mathbf{p}_\nu\mathbf{x})\exp(-iE_it)\nu_i^\circ(0) \simeq \exp\left(-i\frac{m_i^2}{2p_\nu}t\right)\nu_i^\circ(0) = \exp(-i\varphi_i t)\nu_i^\circ(0), \qquad \varphi_i = \frac{m_i^2}{2p_\nu}. \tag{2}$$

The Maki–Nagava–Sakata (MNS) mixing matrix $\hat{V}^l_{\alpha i}$ of Dirac neutrinos [9] has the same form as the SKM mixing matrix of quarks [10], but with its own mixing angles ϑ_{12}, ϑ_{13}, and ϑ_{23} and its own *CP*-violating phase δ_l:

$$\hat{V}^l = \begin{pmatrix} c_{12}c_{13} & s_{12}c_{13} & s_{13}e^{-i\delta_l} \\ -s_{12}c_{13} - c_{12}s_{23}s_{13}e^{i\delta_l} & c_{12}c_{23} - s_{12}s_{23}s_{13}e^{i\delta_l} & s_{23}c_{13} \\ s_{12}s_{23} - c_{12}c_{23}s_{13}e^{i\delta_l} & -c_{12}s_{23} - s_{12}c_{23}s_{13}e^{i\delta_l} & c_{23}c_{13} \end{pmatrix}, \tag{3}$$

where $s_{ik} = \sin\vartheta_{ik}$ and $c_{ik} = \cos\vartheta_{ik}$. Like $\hat{V}_{\mathrm{SKM}}$, the matrix $\hat{V}^l$ is unitary; i.e., $\hat{V}^l\hat{V}^{l+} = 1$.

Previous analysis of experimental data [1–6] gave the following mixing angles [8, 9, 11]

$$\vartheta_{12} = (42.1 \pm 6.9)^\circ, \quad \vartheta_{13} = (2.3 \pm 0.6)^\circ, \quad \vartheta_{23} = (43.6 \pm 3.1)^\circ \tag{4}$$

for $\delta_l = 0$ and

$$m_3 = (0.058 \pm 0.025)\ \text{eV},$$
$$m_2 = (0.0060 \pm 0.0035)\ \text{eV}, \quad m_1 \ll m_2. \tag{5}$$

Here, the mean error in the mixing angles and the masses is taken from figures and tables in [8, 9, 11], where the CHOOZ data [4] from ground-based ν_e sources were taken into account.[1]

Below, we will consider the possibility of determining the leptonic *CP* phase δ_l from the data obtained in current experiments of the type [1–6], where oscillations were not observed directly but only the oscillation-averaged probabilities $P(\nu_\alpha\nu_\beta)$ of $\nu_\alpha \longrightarrow \nu_\beta$ transitions were measured.

The action of matrix (3) on the column vector ν_i° gives [see Eq. (1)]

$$\begin{pmatrix}\nu_e\\ \nu_\mu\\ \nu_\tau\end{pmatrix}_t = \hat{V}_l \begin{pmatrix}\nu_1^\circ\\ \nu_2^\circ\\ \nu_3^\circ\end{pmatrix},$$

i.e.,

$$\begin{aligned}
\nu_e(t) &= [c_{12}c_{13}\nu_1^\circ(0) + s_{12}c_{13}\nu_2^\circ(0)e^{-i\varphi_{21}} \\
&\quad + s_{13}\nu_3^\circ(0)e^{-i\varphi_{31}-i\delta_l}]\exp\left(-i\frac{m_1^2}{2p_\nu}t\right), \\
\nu_\mu(t) &= [-(s_{12}c_{13} + c_{12}s_{23}s_{13}e^{i\delta_l})\nu_1^\circ(0) \\
&\quad + (c_{12}c_{23} - s_{12}s_{23}s_{13}e^{i\delta_l})\nu_2^\circ(0)e^{-i\varphi_{21}} \\
&\quad + c_{13}s_{23}\nu_3^\circ(0)e^{-i\varphi_{31}}]\exp\left(-i\frac{m_1^2}{2p_\nu}t\right), \\
\nu_\tau(t) &= [(s_{12}s_{23} - c_{12}c_{23}s_{13}e^{i\delta_l})\nu_1^\circ(0) \\
&\quad - (c_{12}s_{23} + s_{12}c_{23}s_{13}e^{i\delta_l})\nu_2^\circ(0)e^{-i\varphi_{21}} \\
&\quad + c_{13}c_{23}\nu_3^\circ(0)e^{-i\varphi_{31}}]\exp\left(-i\frac{m_1^2}{2p_\nu}t\right),
\end{aligned} \tag{6}$$

where, taking into account the dependence (2) of neutrino states on time $t = L$, one has

$$\varphi_{ij} = \frac{(m_i^2 - m_j^2)}{2p_\nu}t = 2.54\frac{(m_i^2 - m_j^2)(\text{eV}^2)}{2E_\nu(\text{MeV})}L(\text{m}), \tag{7}$$

with $E_\nu \simeq p_\nu$ being the neutrino energy in a beam, $E_\nu \gg m_3 > m_2 > m_1$. Because the neutrino states $\nu_i^\circ(0)$ are orthonormalized, i.e., $(\overline{\nu_i^\circ}\nu_k^\circ) = \delta_{ik}$,[2] one has for the amplitudes $A_{\alpha\to\beta} = (\overline{\nu_\beta(t)}\,\nu_\alpha(0))$ and probabilities $P(\nu_\alpha\nu_\beta) = \left|(\overline{\nu_\beta(t)}\nu_\alpha(0))\right|^2$ of $\nu_\alpha(0) \longrightarrow \nu_\beta(t)$ transitions in vacuum

$$\begin{aligned}
P(\nu_e\nu_e) &= \left|c_{12}^2c_{13}^2 + s_{12}^2c_{13}^2e^{i\varphi_{21}} + s_{13}^2e^{i\varphi_{31}}\right|^2, \\
P(\nu_\mu\nu_\mu) &= \left|c_{13}s_{12} + c_{12}s_{13}s_{23}e^{i\delta_l}\right|^2 \\
&\quad + \left|c_{12}c_{23} - s_{12}s_{23}s_{13}e^{i\delta_l}\right|^2e^{i\varphi_{21}} + c_{13}^2s_{23}^2e^{i\varphi_{31}}\right|^2, \\
P(\nu_\tau\nu_\tau) &= \left|s_{12}s_{23} - c_{12}c_{23}s_{13}e^{i\delta_l}\right|^2 \\
&\quad + \left|c_{12}s_{23} + s_{12}c_{23}s_{13}e^{i\delta_l}\right|^2e^{i\varphi_{21}} + c_{13}^2c_{23}^2e^{i\varphi_{31}}\right|^2,
\end{aligned} \tag{8}$$

and

$$\begin{aligned}
P(\nu_e\nu_\mu) &= \left|c_{12}c_{13}(c_{13}s_{12} + c_{12}s_{23}s_{13}e^{i\delta_l})\right| \\
&\quad - c_{13}s_{12}(c_{12}c_{23} - s_{12}s_{23}s_{13}e^{i\delta_l})e^{i\varphi_{21}} \\
&\quad - s_{13}c_{13}s_{23}e^{i(\delta_l+\varphi_{31})}\right|^2, \\
P(\nu_e\nu_\tau) &= \left|c_{12}c_{13}(s_{23}s_{12} - c_{12}c_{23}s_{13}e^{i\delta_l})\right. \\
&\quad - c_{13}s_{12}(c_{12}s_{23} + c_{23}s_{12}s_{13}e^{i\delta_l})e^{i\varphi_{21}} \\
&\quad + s_{13}c_{13}c_{23}e^{i(\delta_l+\varphi_{31})}\right|^2, \\
P(\nu_\mu\nu_\tau) &= \left|(c_{13}s_{12} + c_{12}s_{13}s_{23}e^{i\delta_l})\right. \\
&\quad \times (s_{12}s_{23} - c_{12}c_{23}s_{13}e^{-i\delta_l}) \\
&\quad + (c_{12}c_{23} - s_{12}s_{13}s_{23}e^{i\delta}) \\
&\quad \times (c_{12}s_{23} + c_{23}s_{12}s_{13}e^{i\delta})e^{i\varphi_{21}} - c_{23}c_{13}^2s_{23}e^{i\varphi_{31}}\right|^2.
\end{aligned} \tag{9}$$

[1] Unfortunately, results (4) and (5) obtained in [8, 9, 11] using the data reported in [1–6] are insufficiently reliable, especially those based on the data for solar and, partly, atmospheric electron neutrinos ν_e, whose interaction with matter within the Sun or Earth can invert their spin and transform $(\nu_e)_L$ to the sterile, i.e., noninteracting, state $(\nu_e)_R$. This so-called MSW effect [12] does not occur in an analysis of the data from ground-based ν_e sources, e.g., CHOOZ data [4], whose processing yields very small angles $\vartheta_{13} \sim 2°$–$3°$ [see Eq. (4)].

[2] For the Majorana neutrinos, whose fields $\nu_i^0(0)$ with definite mass are real, the requirement that fields ν_e, ν_μ, and ν_τ (6) produced in the weak interaction be real even at $t = 0$ would mean that real matrix (3) is orthogonal, i.e., $\delta_l = \delta_{13} = \pi$ or 0. This is also true for the phases δ_{12} and δ_{23}, which are omitted in Eqs. (3) and (6) because they lead to vanishingly small probabilities of the $\nu_i \longrightarrow \bar{\nu}_k$ transitions with amplitudes $\sim m_\nu/E \sim 10^{-6}$–$10^{-9}$. However, besides simplicity and aesthetics, there are no other reasons for requiring that fields (6) be real and *CP* phase be zero. We intend to consider the Majorana neutrino oscillations elsewhere [13].

Averaging these probabilities over oscillations, i.e., over phases φ_{ij} [by setting $\langle\sin^2\varphi_{ij}\rangle = \langle\cos^2\varphi_{ij}\rangle = 1/2$ and $\langle\cos(\varphi_{ij} \pm \delta_l)\rangle = \langle\cos\varphi_{ij}\rangle = 0$ in Eqs. (8) and (9)], we obtain the following energy-independent probabilities, which were only measured to date [1–6]:

$$\begin{aligned}
\langle 1 - P(\nu_e\nu_e)\rangle &= A_{ee},\\
\langle 1 - P(\nu_\mu\nu_\mu)\rangle &= A_{\mu\mu} + B_{\mu\mu}\cos\delta_l + C_{\mu\mu}\cos^2\delta_l,\\
\langle 1 - P(\nu_\tau\nu_\tau)\rangle &= A_{\tau\tau} + B_{\tau\tau}\cos\delta_l + C_{\tau\tau}\cos^2\delta_l,\\
\langle P(\nu_e\nu_\mu)\rangle &= A_{e\mu} + B_{e\mu}\cos\delta_l,\\
\langle P(\nu_e\nu_\tau)\rangle &= A_{e\tau} + B_{e\tau}\cos\delta_l,\\
\langle P(\nu_\mu\nu_\tau)\rangle &= A_{\mu\tau} + B_{\mu\tau}\cos\delta_l + C_{\mu\tau}\cos(2\delta_l),
\end{aligned} \tag{10}$$

where

$$\begin{aligned}
A_{ee} &= \frac{1}{2}[c_{13}^4\sin^2(2\vartheta_{12}) + \sin^2(2\vartheta_{13})],\\
A_{\mu\mu} &= \frac{1}{2}[(c_{13}^2 + (c_{12}^4 + s_{12}^4)s_{13}^2)\sin^2(2\vartheta_{23})\\
&+ (s_{13}^4\sin^2(2\vartheta_{12}) + \sin^2(2\vartheta_{13}))s_{23}^4 + c_{23}^4\sin^2(2\vartheta_{12})],\\
B_{\mu\mu} &= \frac{1}{2}(c_{23}^2 - s_{23}^2 s_{13}^2)s_{13}\sin(2\vartheta_{23})\sin(4\vartheta_{12}),\\
C_{\mu\mu} &= -\frac{1}{2}s_{13}^2\sin^2(2\vartheta_{23})\sin^2(2\vartheta_{12});\\
A_{\tau\tau} &= \frac{1}{2}[(c_{13}^2 + (c_{12}^4 + s_{12}^4)s_{13}^2)\sin^2(2\vartheta_{23})\\
&+ (s_{13}^4\sin^2(2\vartheta_{12}) + \sin^2(2\vartheta_{13}))c_{23}^4 + s_{23}^4\sin^2(2\vartheta_{12})],\\
B_{\tau\tau} &= -\frac{1}{2}s_{13}\sin(2\vartheta_{23})(s_{23}^2 - c_{23}^2 s_{13}^2)\sin(4\vartheta_{12}),\\
C_{\tau\tau} &= -\frac{1}{2}s_{13}^2\sin^2(2\vartheta_{23})\sin^2(2\vartheta_{12});\\
A_{e\mu} &= \frac{1}{4}[(1 + c_{12}^4 + s_{12}^4)s_{23}^2\sin^2(2\vartheta_{13})]\\
&+ 2c_{13}^2c_{23}^2\sin^2(2\vartheta_{12})],\\
B_{e\mu} &= \frac{1}{8}c_{13}\sin(2\vartheta_{13})\sin(2\vartheta_{23})\sin(4\vartheta_{12});\\
A_{e\tau} &= \frac{1}{4}[(1 + c_{12}^4 + s_{12}^4)c_{23}^2\sin^2(2\vartheta_{13})]\\
&+ 2c_{13}^2s_{23}^2\sin^2(2\vartheta_{12})],\\
B_{e\tau} &= -\frac{1}{8}c_{13}\sin(2\vartheta_{13})\sin(2\vartheta_{23})\sin(4\vartheta_{12});
\end{aligned} \tag{11}$$

$$\begin{aligned}
A_{\mu\tau} &= \frac{1}{4}[2s_{13}^2\sin^2(2\vartheta_{12})\cos^2(2\vartheta_{23})\\
&+ \sin^2(2\vartheta_{23})\{(c_{12}^4 + s_{12}^4)s_{13}^4 + c_{13}^4 + c_{12}^4 + s_{12}^4\}],\\
B_{\mu\tau} &= \frac{1}{8}(1 + s_{13}^2)s_{13}\sin(4\vartheta_{12})\sin(4\vartheta_{23}),\\
C_{\mu\tau} &= -\frac{1}{4}s_{13}^2\sin^2(2\vartheta_{12})\sin^2(2\vartheta_{23}).
\end{aligned}$$

Note that the obvious relationships

$$1 - P(\nu_\alpha\nu_\alpha) = P(\nu_\alpha\nu_\beta) + P(\nu_\alpha\nu_\gamma), \quad \alpha, \beta, \gamma = e, \mu, \tau,$$

are satisfied, and $P(\nu_\beta\nu_\alpha) = [P(\nu_\alpha\nu_\beta)]_{\delta_l \to -\delta_l}$. Using the general formulas for oscillation probabilities from the Appendix, we obtain the following expressions for the differences between the probabilities of forward–backward neutrino transitions:

$$\begin{aligned}
&P(\nu_\mu\nu_e) - P(\nu_e\nu_\mu)\\
&= a_0(\sin\varphi_{21} + \sin\varphi_{32} - \sin\varphi_{31})\sin\delta_l,\\
&P(\nu_\tau\nu_e) - P(\nu_e\nu_\tau)\\
&= -a_0(\sin\varphi_{21} + \sin\varphi_{32} - \sin\varphi_{31})\sin\delta_l,\\
&P(\nu_\tau\nu_\mu) - P(\nu_\mu\nu_\tau)\\
&= a_0\left(\sin\varphi_{21} - 2\sin\frac{\varphi_{21}}{2}\cos\frac{(\varphi_{31} + \varphi_{32})}{2}\right)\sin\delta_l,
\end{aligned} \tag{12}$$

where $a_0 = \frac{1}{2}c_{13}\sin2\vartheta_{12}\sin2\vartheta_{13}\sin2\vartheta_{23} \simeq 0.07$. Unfortunately, the phases φ_{ik} appearing in these relationships depend on the neutrino energy in a beam; therefore, to determine the $\sin\delta_l$ value from Eq. (12), neutrinos ν_α and ν_β should have the same energy E in an experiment. Modern beams include only continuous-spectrum neutrinos, and the effect reflected in Eq. (12) vanishes after averaging over the phases φ_{ik}.

However, the *CP* phase can be obtained in a different way by using Eqs. (10) and (11) and the experimental data similar to those obtained in [1–6] but having a higher accuracy in order to compensate the smallness of angle ϑ_{13}. For clarity, let us introduce the coefficients $b_{ik} = B_{ik}/A_{ik}$ and $c_{ik} = C_{ik}/A_{ik}$ in Eqs. (10) and (11). Because of the smallness of $s_{13} = \sin\vartheta_{13} \simeq 0.07$, almost all of these coefficients are very small and are on the order of a fraction of a percent:

$$\begin{aligned}
A_{ee} &= 0.499;\\
A_{\mu\mu} &= 0.636, \quad b_{\mu\mu} = 0.0058, \quad c_{\mu\mu} = -0.0038;\\
A_{\tau\tau} &= 0.613, \quad b_{\tau\tau} = 0.0055, \quad c_{\tau\tau} = -0.0040;\\
A_{e\mu} &= 0.261, \quad b_{e\mu} = 0.014;
\end{aligned} \tag{13}$$

$$A_{e\tau} = 0.238, \quad b_{e\tau} = -0.015;$$
$$A_{\mu\tau} = 0.373, \quad b_{\mu\tau} = 0.0005, \quad c_{\mu\tau} = -0.0032.$$

For this reason, the ratio of the number of produced ν_μ to that of ν_τ in the primary ν_e beam at large distances L (about 300–500 km) will weakly decrease with increasing δ_l from 0 to π:

$$\frac{N_{\nu_\mu}}{N_{\nu_\tau}} = \frac{\langle P(\nu_e\nu_\mu)\rangle}{\langle P(\nu_e\nu_\tau)\rangle} \simeq \frac{A_{e\mu}}{A_{e\tau}}(1 + (b_{e\mu} - b_{e\tau})\cos\delta_l), \quad (14)$$

where $b_{e\mu} - b_{e\tau} \simeq 2b_{e\mu} \simeq 2.8\%$ and $A_{e\mu}/A_{e\tau} \simeq 1.04$. Therefore, if the experimentally measured ratio (14) differs from 1.04 + 0.03 = 1.07 by more than 1–3%, this would indicate that $\cos\delta_l < 1$; i.e., $\delta_l \neq 0$.

If $s_{13} = \sin\vartheta_{13} > 0.07$, i.e., if s_{13} is larger than the value used in this work, then the *CP* phase will be manifested more strongly. In particular, for $\vartheta_{13} = 14°$, we have $N_{\nu_\mu}/N_{\nu_\tau} \simeq 1.07(1 + 0.08\cos\delta_l)$, and the coefficient a_0 in Eq. (12) is $a_0 \simeq 0.23$.

We are grateful to D.I. Kazakov for information about last year's Osaka Conference and S.P. Mikheev for his discussion on the current situation in neutrino physics. This study was supported by the Russian Foundation for Basic Research (project nos. 00-15-96786 and 00-02-16363).

APPENDIX

The probabilities of all neutrino transitions in vacuum (in the Pontecorvo oscillations with allowance made for the *CP* phase δ_l) are determined by the following general algebraic formulas:

$$1 - P(\nu_e\nu_e) = c_{12}^2\sin^2(2\vartheta_{13})\sin^2(\varphi_{31}/2) + c_{13}^4\sin^2(2\vartheta_{12})\sin^2(\varphi_{21}/2) + s_{12}^2\sin^2(2\vartheta_{13})\sin^2(\varphi_{32}/2), \quad (A1)$$

$$\begin{aligned}1 - P(\nu_\mu\nu_\mu) &= \{c_{23}^4\sin^2(2\vartheta_{12}) + s_{12}^4 s_{13}^2\sin^2(2\vartheta_{23}) \\ &+ s_{23}^4 s_{13}^4\sin^2(2\vartheta_{12}) + c_{12}^4 s_{13}^2\sin^2(2\vartheta_{23}) \\ &+ \cos\delta_l\sin(4\vartheta_{12})\sin(2\vartheta_{23})(s_{13}c_{23}^2 - s_{13}^3 s_{23}^2) \\ &- \cos^2\delta_l s_{13}^2\sin^2(2\vartheta_{23})\sin^2(2\vartheta_{12})\}\sin^2(\varphi_{21}/2) \\ &+ \{s_{12}^2 c_{13}^2\sin^2(2\vartheta_{23}) + c_{12}^2 s_{23}^4\sin^2(2\vartheta_{13}) + \cos\delta_l s_{23}^2 c_{13} \\ &\times \sin(2\vartheta_{12})\sin(2\vartheta_{23})\sin(2\vartheta_{13})\}\sin^2(\varphi_{31}/2) \\ &+ \{c_{12}^2 c_{13}^2\sin^2(2\vartheta_{23}) + s_{12}^2 s_{23}^4\sin^2(2\vartheta_{13}) - \cos\delta_l s_{23}^2 c_{13} \\ &\times \sin(2\vartheta_{12})\sin(2\vartheta_{23})\sin(2\vartheta_{13})\}\sin^2(\varphi_{32}/2),\end{aligned} \quad (A2)$$

$$\begin{aligned}1 - P(\nu_\tau\nu_\tau) &= \{c_{23}^4\sin^2(2\vartheta_{12}) + s_{12}^4 s_{13}^2\sin^2(2\vartheta_{23}) \\ &+ c_{23}^4 s_{13}^4\sin^2(2\vartheta_{12}) + c_{12}^4 s_{13}^2\sin^2(2\vartheta_{23}) \\ &+ \cos\delta_l\sin(4\vartheta_{12})\sin(2\vartheta_{23})(s_{13}^3 c_{23}^2 - s_{13}^2 s_{23}^2) \\ &- \cos^2\delta_l s_{13}^2\sin^2(2\vartheta_{23})\sin^2(2\vartheta_{12})\}\sin^2(\varphi_{21}/2) \\ &+ \{s_{12}^2 c_{13}^2\sin^2(2\vartheta_{23}) + c_{12}^2 c_{23}^4\sin^2(2\vartheta_{13}) + \cos\delta_l c_{23}^2 c_{13} \\ &\times \sin(2\vartheta_{12})\sin(2\vartheta_{23})\sin(2\vartheta_{13})\}\sin^2(\varphi_{31}/2) \\ &+ \{c_{12}^2 c_{13}^2\sin^2(2\vartheta_{23}) + s_{12}^2 c_{23}^4\sin^2(2\vartheta_{13}) + \cos\delta_l c_{23}^2 c_{13} \\ &\times \sin(2\vartheta_{12})\sin(2\vartheta_{23})\sin(2\vartheta_{13})\}\sin^2(\varphi_{32}/2),\end{aligned} \quad (A3)$$

$$\begin{aligned}P(\nu_e\nu_\mu) &= \frac{1}{4}\{\sin^2(2\vartheta_{13})(s_{23}^2 + c_{12}^4 s_{23}^2 + s_{12}^4 s_{23}^2) \\ &+ \frac{1}{2}c_{13}\sin(2\vartheta_{13})\sin(2\vartheta_{23})\sin(4\vartheta_{12})\cos\delta_l) \\ &- 2c_{13}^2\sin^2(2\vartheta_{12})(c_{23}^2 - s_{13}^2 s_{23}^2)\cos(\varphi_{21}) \\ &- 2s_{23}^2\sin^2(2\vartheta_{13})(c_{12}^2\cos(\varphi_{31}) + s_{12}^2\cos(\varphi_{32})) \\ &+ c_{13}\sin(2\vartheta_{12})\sin(2\vartheta_{13})\sin(2\vartheta_{23})(s_{12}^2\cos(\delta_l + \varphi_{21}) \\ &- c_{12}^2\cos(\delta_l - \varphi_{21})) + c_{13}\sin(2\vartheta_{12})\sin(2\vartheta_{13})\sin(2\vartheta_{23}) \\ &\times(\cos(\delta_l + \varphi_{32}) - \cos(\delta_l - \varphi_{31})) + 2c_{13}^2 c_{23}^2\sin^2(2\vartheta_{12})\},\end{aligned} \quad (A4)$$

$$\begin{aligned}P(\nu_e\nu_\tau) &= \frac{1}{4}\{\sin^2(2\vartheta_{13})(c_{23}^2 + c_{12}^4 c_{23}^2 + s_{12}^4 c_{23}^2) \\ &- \frac{1}{2}c_{13}\sin(2\vartheta_{13})\sin(2\vartheta_{23})\sin(4\vartheta_{12})\cos\delta_l) \\ &+ 2c_{13}^2\sin^2(2\vartheta_{12})(c_{23}^2 - s_{13}^2 s_{23}^2)\cos(\varphi_{21}) \\ &- 2c_{23}^2\sin^2(2\vartheta_{13})(c_{12}^2\cos(\varphi_{31}) + s_{12}^2\cos(\varphi_{32})) \\ &+ c_{13}\sin(2\vartheta_{12})\sin(2\vartheta_{13})\sin(2\vartheta_{23})(c_{12}^2\cos(\delta_l - \varphi_{21}) \\ &- s_{12}^2\cos(\delta_l + \varphi_{21})) + c_{13}\sin(2\vartheta_{12})\sin(2\vartheta_{13})\sin(2\vartheta_{23}) \\ &\times(\cos(\delta_l + \varphi_{31}) - \cos(\delta_l + \varphi_{32})) + 2c_{13}^2 s_{23}^2\sin^2(2\vartheta_{12})\},\end{aligned} \quad (A5)$$

$$\begin{aligned}P(\nu_\mu\nu_\tau) &= \frac{1}{4}\{2s_{13}^2\sin^2(2\vartheta_{12})\cos^2(2\vartheta_{23}) \\ &+ (c_{13}^4 + c_{12}^4 + s_{12}^4 + (c_{12}^4 + s_{12}^4)s_{13}^4)\sin^2(2\vartheta_{23}) \\ &- [2s_{13}^2(c_{23}^4 + s_{23}^4)\sin^2(2\vartheta_{12}) + [2s_{13}^2(c_{12}^4 + s_{12}^4) \\ &- (1 + s_{13}^4)\sin^2(2\vartheta_{12})]\sin^2(2\vartheta_{23})]\cos(\varphi_{21}) \\ &- \Big[2c_{13}^2(s_{12}^2 + c_{12}^2 s_{13}^2)\sin^2(2\vartheta_{23}) \\ &- \frac{1}{2}c_{13}\sin(2\vartheta_{12})\sin(2\vartheta_{13})\sin(4\vartheta_{23})\cos\delta_l\Big]\cos(\varphi_{31})\end{aligned}$$

$$+\left[2c_{13}^2\sin^2(2\vartheta_{23})(s_{12}^2s_{13}^2-c_{12}^2)\right. \quad \text{(A6)}$$

$$\left.-\frac{1}{2}c_{13}\sin(2\vartheta_{12})\sin(2\vartheta_{13})\sin(4\vartheta_{23})\cos\delta_l\right]\cos(\varphi_{32})$$

$$+2c_{13}\sin(2\vartheta_{12})\sin(2\vartheta_{13})\sin(2\vartheta_{23})$$

$$\times\sin\delta_l\sin(\varphi_{21}/2)\cos\left(\frac{\varphi_{31}+\varphi_{32}}{2}\right)$$

$$+s_{13}\sin(4\vartheta_{12})\sin(4\vartheta_{23})\cos\delta_l[1+s_{13}^2]\sin^2(\varphi_{21}/2)$$

$$-c_{13}\sin(2\vartheta_{12})\sin(2\vartheta_{13})\sin(2\vartheta_{23})\sin\delta_l\sin(\varphi_{21})$$

$$-2s_{13}^2\sin^2(2\vartheta_{12})\sin^2(2\vartheta_{23})\cos(2\delta_l)\sin^2(\varphi_{21}/2)\}.$$

REFERENCES

1. W. W. M. Alison *et al.*, Phys. Lett. B **449**, 137 (1999); T. Mann, in *Proceedings of the 19th International Conference on Neutrino Physics and Astrophysics, Sadbury, Canada, 2000*; http://nu2000.sno.laurentian/T.Mann/index.html.
2. Y. Fukuda *et al.*, Phys. Lett. B **467**, 185 (1999); Phys. Rev. Lett. **82**, 2644 (1999); H. Sobel, in *Proceedings of the XIX International Conference on Neutrino Physics and Astrophysics, Sudbury, Canada, June 2000*; T. Toshito, in *Proceedings of the XXX International Conference on High Energy Physics, 2000, ICHEP 2000, Osaka, Japan.*
3. S. Athanassopoulos *et al.* (LSND Collab.), Phys. Rev. Lett. **81**, 1774 (1998).
4. M. Apollino *et al.* (CHOOZ Collab.), Phys. Lett. B **420**, 397 (1998); F. Boehm *et al.*, hep-ex/9912050.
5. Y. Suzuki, in *Proceedings of the XIX International Conference on Neutrino Physics and Astrophysics, Sudbury, Canada, 2000*; T. Takeuchi, in *Proceedings of the XXX International Conference on High Energy Physics, 2000, ICHEP 2000, Osaka, Japan*; B. T. Cleveland *et al.*, Astrophys. J. **496**, 505 (1998); R. Davis, Prog. Part. Nucl. Phys. **32**, 13 (1994); K. Lande, in *Proceedings of the XIX International Conference on Neutrino Physics and Astrophysics, Sudbury, Canada, 2000*; http://nu2000.sno.laurentian.ca/.
6. J. N. Abdurashitov *et al.* (SAGE Collab.), Phys. Rev. C **60**, 055801 (1999); V. Garvin, in *Proceedings of the XIX International Conference on Neutrino Physics and Astrophysics, Sudbury, Canada, 2000*; http://nu2000.sno.laurentian.ca/; W. Hampel *et al.* (GALLEX Collab.), Phys. Lett. B **447**, 127 (1999); E. Belloti, in *Proceedings of the XIX International Conference on Neutrino Physics and Astrophysics, Sudbury, Canada, 2000*; http://nu2000.sno.laurentian.ca/; F. Ronga, hep-ex/0001058.
7. M. Pontecorvo, Zh. Éksp. Teor. Fiz. **33**, 549 (1957) [Sov. Phys. JETP **6**, 429 (1958)]; Zh. Éksp. Teor. Fiz. **34**, 247 (1958) [Sov. Phys. JETP **7**, 172 (1958)]; V. N. Gribov and B. M. Pontecorvo, Phys. Lett. **288**, 483 (1969); S. M. Bilenky and B. Pontecorvo, Phys. Rep. **41**, 225 (1978).
8. Z. Berezhiani and A. Rossi, Phys. Lett. B **367**, 219 (1996); Z. Berezhiani and A. Rossi, hep-ph/9811447; R. Barbieri, L. Hall, and A. Strumia, hep-ph/9808333.
9. Z. Maki, M. Nakagava, and S. Sakata, Prog. Theor. Phys. **28**, 870 (1962).
10. Particle Data Group E and C, Eur. Phys. J. C **3**, 1 (1998); Particle Phys. Booclet, VII/2000, pp. 157–159.
11. M. C. Gonzalez-Garsia, M. Maltoni, C. Peña-Garay, and J. W. F. Valle, hep-ph/0009350.
12. J. Bahcall, P. Krastev, and A. Smirnov, hep-ph/9807216; S. P. Mikheyev and A. Yu. Smirnov, Yad. Fiz. **42**, 1441 (1985) [Sov. J. Nucl. Phys. **42**, 913 (1985)]; L. Wolfenstein, Phys. Rev. D **17**, 2369 (1978).
13. K. A. Ter-Martirosyan, Is there difference in the oscillations of Majorana and Dirac neutrinos?, Phys. Lett. (in press).

Translated by R. Tyapaev

JETP Letters, Vol. 74, No. 3, 2001, pp. 144–148. Translated from Pis'ma v Zhurnal Éksperimental'noĭ i Teoreticheskoĭ Fiziki, Vol. 74, No. 3, 2001, pp. 162–166.

Influence of the Spatial Rotation of a Polarization Plane on the Radiative Friction Force in Light Fields with Polarization Gradients

A. V. Bezverbnyĭ

Far East State Marine Academy, Vladivostok, 690059 Russia

e-mail: alexb@fesma.ru

Received June 14, 2001

Simple atomic models (1/2 ⟶ 1/2 and 1/2 ⟶ 3/2 transitions) were taken as an example to consider, in the sub-Doppler cooling approximation, influence of the spatial rotation of a polarization plane on the radiative friction force at arbitrary field configurations of dimensionality $D > 1$. Spatial gradients of the angles determining this rotation additionally contribute to the friction force. This contribution is comparable in magnitude with other forces if the detuning δ is on the order of the radiative relaxation constant γ. For the $j \longrightarrow j + 1$ transitions, the contribution promotes sub-Doppler cooling at $\delta < 0$, whereas for the $j \longrightarrow j$ transitions (half-integer j) it induces anisotropic heating and cooling processes. © *2001 MAIK "Nauka/Interperiodica".*

PACS numbers: 32.80.Lg; 42.50.Vk

1. The kinetics of atomic ensembles in light fields with polarization gradients is governed by the correlation of the atomic translational and internal degrees of freedom; the processes of atomic optical orientation and momentum transfer from the field to atoms through the spontaneous and induced radiation give rise, in combination with the translational motion of atoms, to new kinetic phenomena such as sub-Doppler cooling and formation of light-induced atomic gratings. The major mechanisms of sub-Doppler cooling are considered in [1] using simple one-dimensional field configurations *lin* ⊥ *lin* [with only the spatial gradient of field ellipticity $\varepsilon(\mathbf{r})$] and σ_+-σ_- [with only the spatial gradient of the rotation angle $\phi(\mathbf{r})$ of the polarization ellipse] as an example. Some other kinetic aspects of one-dimensional field configurations with the spatial gradients of several field parameters [ellipticity, ellipse rotation angle, field amplitude $\mathscr{E}(\mathbf{r})$, and field phase $\Phi(\mathbf{r})$] are considered in [2]. However, in addition to these gradients, gradients caused by the spatial rotation of field polarization plane appear in the field configurations of higher dimensionality. As is known, such configurations are used intensively in the experiments on grating formation. In this work, a simple two-level model of atoms with the total angular momentum $j_g = 1/2$ in the ground state is taken in an arbitrary non-one-dimensional field configuration to analyze the contribution to the cooling kinetics from new gradients, which are absent in the one-dimensional configurations and have not been considered so far.

2. Field configuration of dimensionality $D > 1$ is formed by $s \geq 3$ noncollinear (at least one pair of wave vectors is such that $[\mathbf{k}_n \times \mathbf{k}_{n'}] \neq 0$, and $\sum_{n=1}^{s} \mathbf{k}_n = 0$) coherent monochromatic plane waves with identical frequency ω and can be represented, in the general case, as

$$\begin{aligned}\mathbf{E}(\mathbf{r}, t) &= \sum_{n=1}^{s} (e^{-i\omega t + i\mathbf{k}_n\mathbf{r}}\mathbf{E}_n + \text{c.c}) \\ &= (e^{-i\omega t}\mathbf{E}(\mathbf{r}) + e^{i\omega t}\mathbf{E}^*(\mathbf{r})),\end{aligned} \tag{1}$$

where $(\ldots)^*$ stands for the complex conjugation, and $\mathbf{E}(\mathbf{r}) = |\mathscr{E}|e^{i\Phi}\mathbf{e}$ and $\mathbf{E}^*(\mathbf{r})$ are the negative- and positive-frequency field components, respectively. Here, $\mathbf{e}$ is the unit polarization vector. Let us consider a small variation of these components upon passing to $\mathbf{r} + \delta\mathbf{r}$. For example, the variation $\delta\mathbf{E} = \mathbf{E}(\mathbf{r} + \delta\mathbf{r}) - \mathbf{E}(\mathbf{r})$ is expressed through the field gradients as follows:

$$\begin{aligned}\delta\mathbf{E} &= \left(\delta\mathbf{r} \cdot \left[\frac{\nabla|\mathscr{E}|}{|\mathscr{E}|} + i\nabla\Phi + \frac{l\nabla\varepsilon - i\nabla\phi}{\mathscr{A}}\right]\right)\mathbf{E}(\mathbf{r}) \\ &+ \left(\delta\mathbf{r} \cdot \frac{il\nabla\phi - \nabla\varepsilon}{\mathscr{A}}\right)e^{2i\Phi}\mathbf{E}^*(\mathbf{r}) + (\mathbf{e}_0 \cdot (\delta\mathbf{r} \cdot \nabla)\mathbf{E})\mathbf{e}_0,\end{aligned} \tag{2}$$

where $l = \cos 2\varepsilon$ (domain of variability $0 \leq l \leq 1$) and $\mathscr{A} = \sin 2\varepsilon$ (domain of variability $-1 \leq \mathscr{A} \leq 1$) are connected with the degrees of linear $L = l^2$ and circular $A = \mathscr{A}^2$ field polarizations [3] ($A + L = 1$ for the coherent fields), and vector $\mathbf{e}_0 = -i[\mathbf{e} \times \mathbf{e}^*]/\mathscr{A}$ is perpendicular to the local polarization plane. The last contribution in Eq. (2) describes small spatial rotation of the $\mathbf{E}$ vector out of the initial polarization plane. It is inevitably present in the field configurations with $D > 1$. The angles of rotation α and β of the principal axes of the polarization ellipse in the directions perpendicular to

the initial plane are chosen as parameters of this rotation (Fig. 1). The unit vectors specifying the positions of the principal axes are defined in an invariant fashion as

$$\mathbf{e}_a = (\mathbf{e} + \mathbf{e}^*)/\sqrt{2(1+l)};$$
$$\mathbf{e}_b = -i(\mathbf{e} - \mathbf{e}^*)/\sqrt{2(1-l)}. \quad (3)$$

It should be noted that the constant phase is chosen for $\mathbf{e}$ and $\mathbf{e}^*$ so that $(\mathbf{e}\cdot\mathbf{e}) = (\mathbf{e}^*\cdot\mathbf{e}^*) = l$, which corresponds to the total field phase $e^{4i\Phi} = (\mathbf{E}(\mathbf{r})\cdot\mathbf{E}(\mathbf{r}))/(\mathbf{E}^*(\mathbf{r})\cdot\mathbf{E}^*(\mathbf{r}))$. For the field configurations with $D > 1$, the problem of determining the directions of $\mathbf{e}_a$, $\mathbf{e}_b$, and $\mathbf{e}_0$ in the regions with linear polarization is solved by passing to the limit $l \longrightarrow 1$, because the dimensionality of these regions is no higher than $D - 1$. In this case, $\mathbf{e}_a$ specifies the position of the major axis, $\mathbf{e}_b$ specifies the position of the minor axis of the polarization ellipse, and the gradients of angles α and β are defined as

$$\nabla\alpha = \nabla(\underline{\mathbf{e}_a}\cdot\mathbf{e}_0); \quad \nabla\beta = \nabla(\underline{\mathbf{e}_b}\cdot\mathbf{e}_0). \quad (4)$$

Hereafter, the differentiated quantities are underlined.

3. Let us consider the influence of gradient (4) on the processes of optical orientation taking, as an example, a simple model of two-level atoms with the ground-state total angular momentum $j_g = 1/2$ in the standard conditions of sub-Doppler cooling. Specifically, the saturation of the resonant dipolar transition is small, $S = |\Omega|^2/(\gamma^2/4 + \delta^2) \ll 1$, where $\Omega = d|\mathscr{E}|e^{i\Phi}/\hbar$ (d is the reduced dipole transition moment) is the Rabi frequency, γ is the radiative spontaneous decay constant in the excited state, and $\delta = \omega - \omega_0$ is the detuning from the resonance; the atoms are slow, $kv \ll \gamma S$, where $k = |\mathbf{k}_n|$; and the interatomic collisions are ignored. Under these conditions, the problem of optical pumping reduces to the analysis of the ground-state density matrix $\hat{\rho}^g$. In the representation of the eigenstates of the angular momentum operator Jm, the diagonal components $\hat{\rho}^g_{\mu\mu'}$ specify the populations of Zeeman sublevels, while the nondiagonal components correspond to the coherence in these sublevels. In the irreducible tensor representation, $\hat{\rho}^g_{\kappa q}$ are the multipole moments of rank $0 \le \kappa \le 2j_g$. For the states with $j_g = 1/2$, the anisotropy is described only by the first-rank moment $\hat{\rho}^g_1$, and, to the zero order in the recoil parameter $\hbar k/\Delta p$ and first order in the field intensity, the closed equation for the evolution of $\hat{\rho}^g$ is equivalent to the equation for the optical orientation vector $\mathbf{J} = \hbar\sqrt{2}\hat{\rho}^g_1$ [4]:

$$(\partial_t + \mathbf{v}\cdot\nabla)\mathbf{J} = (\gamma S/9N_e)$$
$$\times(2\hbar\mathscr{A}\mathbf{e}_0 - 2\mathbf{J} - (1+l)(\mathbf{e}_a\cdot\mathbf{J})\mathbf{e}_a \quad (5)$$
$$-(1-l)(\mathbf{e}_b\cdot\mathbf{J})\mathbf{e}_b + (-1)^{N_e/2}6\tilde{\delta}\mathscr{A}[\mathbf{J}\times\mathbf{e}_0]).$$

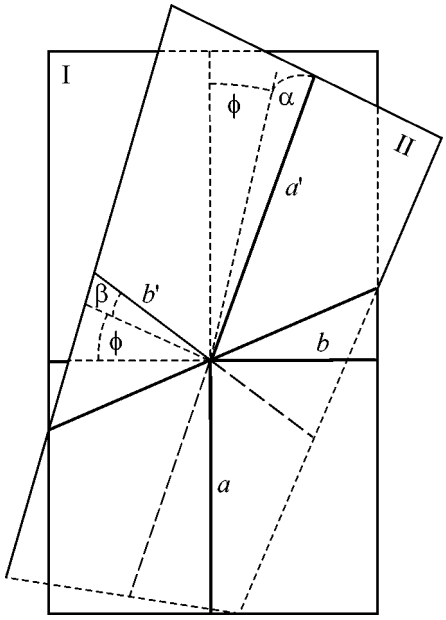

Fig. 1. Spatial rotation of the polarization plane from position I to position II; ϕ is the rotation angle of the polarization ellipse in the initial plane I; α and β are the rotation angles of the major and minor axes a and b from the initial plane to the final positions a' and b'.

Hereafter, the notation $\tilde{\delta} = \delta/\gamma$ and $N_e = 2j_e + 1$ is introduced. The total angular momentum of the excited state can be either $j_e = 1/2$ or $j_e = 3/2$, depending on the type of transition.

Let us use the approximation of slow atoms $kv \ll \gamma S$ and consider the steady-state pumping regime ($\partial_t\mathbf{J} = 0$). For the quiescent atoms, the well-known result $\mathbf{J}^{(0)} = \hbar\mathscr{A}\mathbf{e}_0$ is straightforward, indicating that the ground-state Zeeman sublevels $\mu = \pm 1/2$ are differently populated in the local basis with the quantization axis directed along $\mathbf{e}_0$; the $\mathbf{J}$ projection onto this axis is proportional to the difference in the populations of these sublevels, $(\mathbf{J}\cdot\mathbf{e}_0) = \hbar\Pi = \hbar(\hat{\rho}^g_+ - \hat{\rho}^g_-)$; it is independent of the field intensity and determined only by the $\mathscr{A}$ value. The remaining projections are proportional to the coherence elements $\hat{\rho}^g_{+-}$ and $\hat{\rho}^g_{-+}$ and vanish in this approximation. The next order in small parameter $kv/\gamma S < 1$, $\mathbf{J}^{(1)}$, is linear in atomic velocity and has all three nonzero projections in the local basis $\{\mathbf{e}_0, \mathbf{e}_a, \mathbf{e}_b\}$:

$$\mathscr{J}_0 = (\mathbf{e}_0\cdot\mathbf{J}^{(1)}) = -9N_e(2\gamma S)^{-1}\hbar(\mathbf{v}\cdot\nabla)\mathscr{A}$$
$$= -9N_e(\gamma S)^{-1}\hbar l(\mathbf{v}\cdot\nabla)\varepsilon; \quad (6)$$

$$\mathscr{J}_a = (\mathbf{e}_a\cdot\mathbf{J}^{(1)}) = 9N_e(N\gamma S)^{-1}\hbar\mathscr{A}$$
$$\times((3-l)(\mathbf{v}\cdot\nabla)\alpha - (-1)^{N_e/2}6\tilde{\delta}\mathscr{A}(\mathbf{v}\cdot\nabla)\beta); \quad (7)$$

$$\mathcal{J}_b = (\mathbf{e}_b \cdot \mathbf{J}^{(1)}) = 9N_e(N\gamma S)^{-1}\hbar\mathcal{A} \times ((3+l)(\mathbf{v}\cdot\nabla)\beta + (-1)^{N_e/2}6\tilde{\delta}\mathcal{A}(\mathbf{v}\cdot\nabla)\alpha), \quad (8)$$

where $N = 9 - l^2 + 36(\tilde{\delta}\mathcal{A})^2$. Note that Eqs. (6)–(8) are completely unusable in the region of field nodes $|\mathcal{E}| = 0$, where the condition $kv/\gamma S < 1$ breaks for any velocity $v \neq 0$. We leave aside this issue, because it is of no importance for our further consideration.

The $\mathbf{J}_\parallel^{(1)} = \mathcal{J}_0\mathbf{e}_0$ component accounts for the retardation effect in optical pumping. This effect results in a population difference transfer if the local quantization axis is chosen along $\mathbf{e}_0$. With this choice, the other component $\mathbf{J}_\perp^{(1)} = \mathcal{J}_a\mathbf{e}_a + \mathcal{J}_b\mathbf{e}_b$ is nonzero only in the field configurations with $D > 1$, where it describes the coherence in the Zeeman sublevels –1/2 and +1/2. It is comparable with (6) at small detunings $|\delta| \le \gamma$ and decreases as $\tilde{\delta}^{-1}$ at large detunings. Let us estimate the contribution of this component to the radiative force acting on atoms.

4. In the approximation of sub-Doppler cooling, the light-induced force is written, according to [5], as

$$\mathbf{F} \approx -i\hbar(\gamma/2 + i\delta)^{-1}\mathrm{Tr}[\hat{\rho}^g\Omega^*\tilde{V}^\dagger\nabla(\Omega\tilde{V})] + \text{c.c.}, \quad (9)$$

where $\tilde{V}$ is the reduced (dimensionless) operator of dipolar interaction and $\tilde{V}^\dagger$ is its Hermitian conjugate. The density matrix $\hat{\rho}^{g,(0)}$ of the quiescent atoms allows one to determine the light-pressure force and the gradient force [5] acting on the atom in the fields with polarization gradients, while the correction $\hat{\rho}^{g,(1)}$, linear in velocity, contributes to the radiative friction force and the force of the Lorentzian type. For $j_g = 1/2$, this contribution can be represented as [4]

$$\mathbf{F}^{(1)} \approx -(-1)^{N_e/2}S(\gamma/2 - i\delta)/(3N_e|\mathcal{E}|^2) \times \nabla(\mathbf{J}^{(1)} \cdot [\underline{\mathbf{E}} \times \mathbf{E}^*]) + \text{c.c.} \quad (10)$$

Note that force (10) includes basically different contributions. The component $\mathbf{J}_\parallel^{(1)}$ corresponds to the contribution

$$\mathbf{F}_\parallel^{(1)} = 3\hbar l(-1)^{N_e/2}(\mathbf{v}\cdot\nabla)\varepsilon \times [2\tilde{\delta}(\mathcal{A}\nabla\ln|\mathcal{E}| + l\nabla\varepsilon) - (\mathcal{A}\nabla\Phi + \nabla\phi)], \quad (11)$$

from the gradients of ellipticity ε, amplitude $|\mathcal{E}|$, total phase Φ, and angle of rotation φ of the polarization ellipse.

The contribution

$$\mathbf{F}_\perp^{(1)} = \hbar(\mathbf{v}\cdot\nabla)\alpha(\tilde{\mathfrak{F}}_{\alpha\alpha}\nabla\alpha + \tilde{\mathfrak{F}}_{\alpha\beta}\nabla\beta) + \hbar(\mathbf{v}\cdot\nabla)\beta(\tilde{\mathfrak{F}}_{\beta\alpha}\nabla\alpha + \tilde{\mathfrak{F}}_{\beta\beta}\nabla\beta), \quad (12)$$

from the component $\mathbf{J}_\perp^{(1)}$ is due only to gradients (4). The dimensionless coefficients $\tilde{\mathfrak{F}}$ in Eq. (12) are:

$$\tilde{\mathfrak{F}}_{\alpha\alpha} = 12\tilde{\delta}\mathcal{A}^2 l/N,$$

$$\tilde{\mathfrak{F}}_{\beta\alpha} = 3\mathcal{A}(l+1)((12\tilde{\delta}^2 - 1)l - (3 + 12\tilde{\delta}^2))/2N;$$

$$\tilde{\mathfrak{F}}_{\beta\beta} = -\tilde{\mathfrak{F}}_{\alpha\alpha},$$

$$\tilde{\mathfrak{F}}_{\alpha\beta} = 3\mathcal{A}(1-l)((12\tilde{\delta}^2 - 1)l + (3 + 12\tilde{\delta}^2))/2N$$

for $j_e = 1/2$ and

$$\tilde{\mathfrak{F}}_{\alpha\alpha} = 6\tilde{\delta}\mathcal{A}^2(3+l)/N,$$

$$\tilde{\mathfrak{F}}_{\beta\alpha} = 3\mathcal{A}(l+1)((12\tilde{\delta}^2 + 1)l - (12\tilde{\delta}^2 - 3))/2N;$$

$$\tilde{\mathfrak{F}}_{\beta\beta} = 6\tilde{\delta}\mathcal{A}^2(3-l)/N,$$

$$\tilde{\mathfrak{F}}_{\alpha\beta} = 3\mathcal{A}(1-l)((12\tilde{\delta}^2 + 1)l + (12\tilde{\delta}^2 - 3))/2N$$

for $j_e = 3/2$.

Let us consider the properties of force (12)

5. At large detunings $|\delta| \gg \gamma$, the terms with nondiagonal components $\tilde{\mathfrak{F}}_{\alpha\beta} \approx -\tilde{\mathfrak{F}}_{\beta\alpha} \approx \mathcal{A}/2$ become dominant in Eq. (12), so that the asymptotic expression for the force has the Lorentzian form $\mathbf{F}_\perp^{(1)} \approx [\mathbf{v} \times \mathbf{B}_{\text{eff}}]$, with $\mathbf{B}_{\text{eff}} = (\hbar\mathcal{A}/2)[\nabla\beta \times \nabla\alpha]$. Analysis of the more complex transitions shows that this property is independent of the transition type and that for the so-called "bleaching" transitions $j \longrightarrow j - 1$ and $j \longrightarrow j$ (integer j) the force $\mathbf{F}_\perp^{(1)}$ always has the Lorentzian form. Evidently, at large detunings the dynamics of slow atoms is properly described in the adiabatic approximation. In this case, Lorentzian-type forces are induced by the spatial gradients of the internal (adiabatic) atomic state [6].

In the remaining cases, the coefficients $\tilde{\mathfrak{F}}$ for the $1/2 \longrightarrow 1/2$ and $1/2 \longrightarrow 3/2$ transitions are cardinally different. Let us consider the diagonal components $\tilde{\mathfrak{F}}_{\beta\beta}$ and $\tilde{\mathfrak{F}}_{\alpha\alpha}$ in Eq. (12) and the symmetric component $\tilde{\mathfrak{F}}_{\beta\alpha} + \tilde{\mathfrak{F}}_{\alpha\beta}$, which contribute to the radiative friction tensor [4] governing the anisotropic atom heating and cooling kinetics in the field configurations with $D > 1$. It is worth noting that the diagonal components do not change their sign and are even functions over the entire range of the ellipticity parameter $-\pi/4 \le \varepsilon \le \pi/4$, whereas $\tilde{\mathfrak{F}}_{\beta\alpha} + \tilde{\mathfrak{F}}_{\alpha\beta}$ is an asymmetric function of ε. When estimating the integral effect of the $\mathbf{F}_\perp^{(1)}$ force through averaging over a certain spatial period of field (1), the latter contribution can be ignored, while the remaining contributions induce the cooling (heating) effect accumulating with time. However, the coefficients $\tilde{\mathfrak{F}}_{\alpha\alpha}$ and $\tilde{\mathfrak{F}}_{\beta\beta}$ for the $1/2 \longrightarrow 1/2$ transition differ in sign. This signifies, e.g., that the α gradient induces cooling while the β gradient induces heating at $\delta < 0$. For the

1/2 ⟶ 3/2 transition, the coefficients $\mathfrak{F}_{\alpha\alpha}$ and $\mathfrak{F}_{\beta\beta}$ have the same sign. It should be emphasized that these coefficients are similar to $\mathfrak{F}_{\varepsilon\varepsilon} = 6\tilde{\delta}l^2$ [see Eq. (11)] in that their signs are identical and constant over the entire ellipticity range $-\pi/4 \le \varepsilon \le \pi/4$ and all of them are odd functions of detuning δ. In other words, for the detunings $\delta < 0$ corresponding to cooling by the Sisyphean mechanism [1], the α and β gradients favor this process.

$\mathfrak{F}_{\alpha\alpha}$, $\mathfrak{F}_{\beta\beta}$, and $\mathfrak{F}_{\varepsilon\varepsilon}$ are odd functions of δ, have the same sign, and do not change it over the entire range of ε values also for the more complex transitions of the $j \longrightarrow j+1$ type (Fig. 2), whereas no such behavior is observed for the $j \longrightarrow j$ (half-integer j) transitions. A comparison of the contribution from the cooling due to the α and β gradients with the known forces indicates that $\mathfrak{F}_{\alpha\alpha}$ and $\mathfrak{F}_{\beta\beta}$ reach their maxima at small detunings $|\delta| \sim \gamma/2$, whereupon they slowly decrease with increasing $|\delta|$, and are usually an order of magnitude smaller than, e.g., $\mathfrak{F}_{\varepsilon\varepsilon}$ or $\mathfrak{F}_{\mathscr{E}\varepsilon}$. Nevertheless, the role of these gradients in the sub-Doppler cooling kinetics may be substantial. One can see in Fig. 2 that $\mathfrak{F}_{\alpha\alpha}$ and $\mathfrak{F}_{\beta\beta}$ are finite in the regions of circularly polarized field, $|\varepsilon| = \pi/4$ ($l = 0$), whereas the remaining forces in Eq. (11) disappear in these regions. These regions are of particular importance because they correspond to the minima of light-induced potentials [1, 5], where particles are, most likely, accumulated in the course of formation of optical atomic gratings; i.e., the action of the force $\mathbf{F}_{\perp}^{(1)}$ on the trapped atoms may become comparable with the action of $\mathbf{F}_{\parallel}^{(1)}$.

6. Let us consider the reasons for such different manifestations of the $\mathbf{F}_{\perp}^{(1)}$ force in the $j \longrightarrow j$ (half-integer j) and $j \longrightarrow j+1$ transitions. To this end, let us separate the terms corresponding to the corrections to the gradient force $\mathbf{F}_g^{(1)} \sim i\delta\nabla(\mathbf{J}^{(1)} \cdot [\underline{\mathbf{E}} \times \underline{\mathbf{E}}^*])$ and to the light-pressure force $\mathbf{F}_p^{(1)} \sim \gamma\nabla(\mathbf{J}^{(1)} \cdot ([\underline{\mathbf{E}} \times \mathbf{E}^*] - [\mathbf{E} \times \underline{\mathbf{E}}^*]))$ from the initial force definition (10) and take into account that $[\mathbf{E} \times \mathbf{E}^*] = i\mathscr{A}|\mathscr{E}|^2\mathbf{e}_0$. Then the correction to the gradient force takes the form

$$\mathbf{F}_g^{(1)} = \mathscr{J}_0\nabla\Delta_S + \Delta_S\nabla(\mathbf{J}^{(1)} \cdot \underline{\mathbf{e}_0}) = \mathbf{F}_S + \mathbf{F}_{ad,1}, \quad (13)$$

where $\hbar\Delta_S = -(-1)^{N_e/2}\hbar\delta S\mathscr{A}/3N_e$ is the dynamic Stark shift (written to a constant) of the $\mu = +1/2$ sublevel (quantization axis along $\mathbf{e}_0$). For the $\mu = -1/2$ sublevel, it is equal to $-\hbar\Delta_S$. Since the projection $\mathscr{J}_0 = \hbar\Pi^{(1)}$ appears as a correction to the population difference of sublevels, the force $\mathbf{F}_S$, being equal to the contribution from the ellipticity and amplitude gradients in Eq. (11), is responsible for the known Sisyphean cooling mechanism [1], which is based on the influence of the retardation in the ground-state optical pumping on the motional dynamics of atoms in the light-induced potentials caused by the induced photon emission and absorption processes. In this case, the cooling by the $\mathbf{F}_S$ force occurs at $\delta < 0$ for the 1/2 ⟶ 3/2 transition and at $\delta > 0$ for the 1/2 ⟶ 1/2 transition [7], because the optical shifts for these transitions have different signs. The new force $\mathbf{F}_{ad,1} = -\Delta_S(\mathscr{J}_a\nabla\alpha + \mathscr{J}_b\nabla\beta)$ in Eq. (13) is also due to the retardation effect, which, however, manifests itself not in the spatial population difference transfer but in the appearance of a coherence (proportional to $\mathscr{J}_a$ and $\mathscr{J}_b$) in the ground-state sublevels as a result of changing spatial position of the quantization axis $\mathbf{e}_0$. When averaged over the field period, this force induces cooling under the same conditions as the force $\mathbf{F}_S$, but its direction in space is determined not by the gradient of light-induced potential $\hbar\Delta_S$, but by the gradient of geometric potential associated with the internal (adiabatic) atomic state [6].

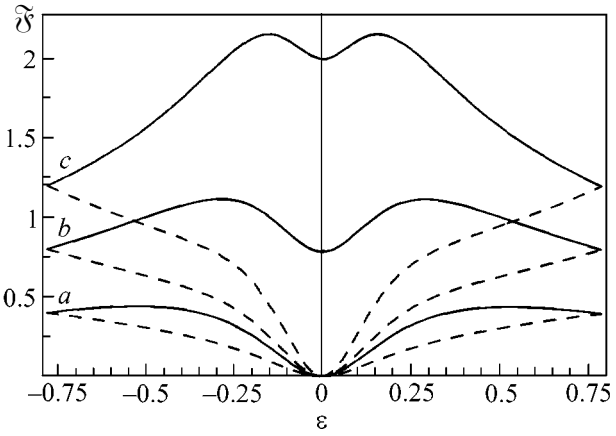

Fig. 2. (solid lines) $\mathfrak{F}_{\alpha\alpha}(\varepsilon)$ and (dashed lines) $\mathfrak{F}_{\beta\beta}(\varepsilon)$ functions for the transitions (*a*) 1/2 ⟶ 3/2, (*b*) 1 ⟶ 2, and (*c*) 3/2 ⟶ 5/2 at the detunings $|\delta| = \gamma$.

The correction to the light-pressure force can be represented as the sum

$$\mathbf{F}_p^{(1)} = \mathbf{F}_{sp} + \mathbf{F}_{ad,2}, \quad (14)$$

where $\mathbf{F}_{sp} = \mathbf{F}_+\hat{\rho}_+^{(1)} + \mathbf{F}_-\hat{\rho}_-^{(1)} = \mathbf{F}_+\Pi^{(1)}$ is the correction to the averaged light-pressure force. Here, $\mathbf{F}_+ = -\mathbf{F}_- = (-1)^{N_e/2}\hbar\gamma S(\mathscr{A}\nabla\Phi + \nabla\phi)/3N_e$ is the light-pressure force acting on the atom in the $\mu = +1/2$ ($\mu = -1/2$) state and caused by the recoil effect accompanying the photon absorption and its spontaneous emission by the excited atom [8]; $\hat{\rho}_+^{(1)}$ and $\hat{\rho}_-^{(1)}$ are the corrections to the sublevel populations. This force appears in Eq. (11) as a contribution from the $\nabla\Phi$ and $\nabla\phi$ gradients. For the models with $j_g = 1/2$, it is independent of the field detuning; its possible influence on the atom cooling is considered in [2]. Contrary to $\mathbf{F}_{sp}$, the new force $\mathbf{F}_{ad,2} = \gamma S(-1)^{N_e/2}((1+l)\mathscr{J}_b\nabla\alpha - (1-l)\mathscr{J}_a\nabla\beta)/6N_e$ in Eq. (14)

depends on the detuning; the component that does not disappear upon averaging over the spatial period of the light field is an odd function of δ and identical for both types of transition:

$$\mathbf{F}_{ad,2d} = 9\hbar\delta\mathcal{A}^2((1+l)(\mathbf{v}\cdot\nabla)\alpha\nabla\alpha + (1-l)(\mathbf{v}\cdot\nabla)\beta\nabla\beta)/\gamma N.$$

This component contributes to the cooling at $\delta < 0$ analogously to the well-known Doppler cooling mechanism [8].

Therefore, the α and β gradients introduce corrections to both gradient and light-pressure forces, thereby contributing to the anisotropic atom heating and cooling processes. However, the effect of the $\mathbf{F}_{ad,1}$ correction depends on the sign of optical shift Δ_S, whereas the $\mathbf{F}_{ad,2}$ correction always leads to cooling at $\delta < 0$. For this reason, these corrections act in parallel with each other and with the Sisyphean cooling mechanism for the $j \longrightarrow j+1$ transitions, whereas, for the $j \longrightarrow j$ transitions (half-integer j), the contribution to cooling from one correction is accompanied by a comparable contribution to heating from the other correction.

The following important aspects of influence of the α and β gradients on the kinetics of atomic ensemble are also noteworthy: the space symmetry of vector field $\mathbf{F}_{\perp}^{(1)}$ differs from that of $\mathbf{F}_{\parallel}^{(1)}$ (an example is given in [4]); the contribution from the $\mathbf{F}_{\perp}^{(1)}$ fluctuations to the diffusivity tensor in momentum space may be comparable with the contributions from the other field gradients at detunings $|\delta| \sim \gamma$.

REFERENCES

1. J. Dalibard and C. Cohen-Tannoudji, J. Opt. Soc. Am. B **6**, 2023 (1989).
2. O. N. Prudnikov, A. V. Taĭchenachev, A. M. Tumaĭkin, *et al.*, Pis'ma Zh. Éksp. Teor. Fiz. **70**, 439 (1999) [JETP Lett. **70**, 443 (1999)].
3. L. D. Landau and E. M. Lifshitz, *The Classical Theory of Fields* (Nauka, Moscow, 1988; Pergamon, Oxford, 1975).
4. A. V. Bezverbnyĭ, Zh. Éksp. Teor. Fiz. **118**, 1066 (2000) [JETP **91**, 921 (2000)].
5. A. V. Bezverbnyi, G. Nienhuis, and A. M. Tumaikin, Opt. Commun. **148**, 151 (1998).
6. P. M. Visser and G. Nienhuis, Phys. Rev. A **57**, 4581 (1998).
7. V. Finkelstein, P. R. Berman, and J. Guo, Phys. Rev. A **45**, 1829 (1992).
8. V. G. Minogin and V. S. Letokhov, *The Pressure of Laser Radiation on Atoms* (Nauka, Moscow, 1986).

Translated by V. Sakun

JETP Letters, Vol. 74, No. 3, 2001, pp. 149–153. Translated from Pis'ma v Zhurnal Éksperimental'noĭ i Teoreticheskoĭ Fiziki, Vol. 74, No. 3, 2001, pp. 167–171.

Reflection of Atto- and Femtosecond X-ray Pulses from Aperiodic Multilayer Mirror

I. L. Beĭgman, A. S. Pirozhkov, and E. N. Ragozin*

Lebedev Physical Institute, Russian Academy of Sciences, Leninskiĭ pr. 53, Moscow, 119991 Russia

** e-mail: ragozin@sci.lebedev.ru*

Received June 29, 2001

The reflection of femto- and attosecond soft and hard X-ray pulses from multilayer structures (MSs) was investigated. The conditions are formulated under which the pulse shape and duration barely change upon reflection. The MSs are optimized for the reflection of extremely short pulses, and the possibility of compressing chirped pulses is considered. It is shown that the power reflection coefficient can be appreciably larger than unity. The aperiodic MSs capable of effectively reflecting pulses containing no more than three wave periods are calculated. © *2001 MAIK "Nauka/Interperiodica".*

PACS numbers: 41.50.+h; 07.85.Fv

In recent years, interest has been growing in the generation of femto- and attosecond X-ray pulses. These pulses can be generated upon the resonant interaction of laser and counter propagating relativistic ion beams [1]. The idea was proposed that the subfemtosecond (~0.1 fs) soft X-ray pulses can be obtained through the coherent generation of high laser harmonics, and numerical simulation of this process was accomplished in [2]. Recently, the high-harmonic generation efficiency of femtosecond laser was enhanced substantially (~1 nJ per pulse, $\hbar\omega \sim 45$–50 eV), and the femtosecond soft X-ray pulses (1.8 fs) were obtained [3–5].

Multilayer structures (MSs) are among the most efficient elements of X-ray optics, because they effectively reflect the soft X-ray radiation at normal incidence and the hard X-ray radiation at not-too-small angles of grazing incidence. In this work, we consider the reflection of atto- and femtosecond X-ray pulses from an MS and place particular emphasis on the reflection of extremely short pulses including no more than a few wave periods. The following two points should be taken into account in this respect.

First, the minimal relative width of the pulse spectrum is approximately equal to the ratio of wave period to pulse duration $\delta\omega_p/\omega_0 \sim T/\tau$ (ω_0 is the carrier frequency, $\delta\omega_p$ is the spectral width, T is the wave period, and τ is the pulse duration). For instance, the spectral width of a few-cycle pulse is comparable to the carrier frequency. Since the reflection from periodic MSs displays resonance dependence on frequency ($\Delta\omega/\omega_0 \sim 0.05$–$0.01$), the efficient reflection is possible only for pulses containing no less than several tens of wave periods. For the reflection of extremely short X-ray pulses, MSs with a broad reflectivity spectrum should be used; this becomes possible with the class of aperiodic MSs [6–8]. One such MS with the reflectivity band at 125–250 Å was calculated, synthesized, and tested in a recent work [9].

Second, the reflection of different spectral components of a signal occurs, so to speak, at different MS depths. This causes pulse delay and a change in the temporal pulse shape upon reflection. In other words, the group delay t_g causes the reflected pulse delay relative to the incident pulse, while its dispersion distorts and lengthens the reflected pulse. At the same time, this fact can be utilized to shorten chirped pulses and increase their power with the help of a broadband aperiodic MS of special type.

Let us consider the reflection of a comparatively long, bandwidth-limited pulse with carrier frequency ω_0 and spectral width $\delta\omega_p$ much narrower than the MS reflectivity band, $\delta\omega_p \sim 2\pi/\tau \ll \Delta\omega$. Let $r(\omega) = |r(\omega)|\exp[i\Phi(\omega)]$ be the complex amplitude reflection coefficient of any (not necessarily periodic) MS and $\Phi(\omega)$ be its phase. Then the reflected pulse delay relative to the incident pulse is $t_g = d\Phi(\omega)/d\omega|_{\omega = \omega_0}$, and the "spreading" in time is determined by the dispersion of group delay and its spectral width: $\sim(dt_g/d\omega)\delta\omega_p$. The pulse spreading may be particularly large for the broadband mirrors unless the requirement that the group delay be constant is imposed when solving the inverse problem of multilayer optics. The time t_g can be expressed through the effective depth L_{eff} at which the reflection occurs, $t_g = mN_{\text{eff}}T/2$, where N_{eff} is the monolayer number corresponding to L_{eff} and m is the order of

0021-3640/01/7403-0149$21.00 © 2001 MAIK "Nauka/Interperiodica"

reflection, usually equal to unity. The requirement that the number of MS layers be less than N_{eff} is dictated by the efficiency loss and cannot be regarded as the cardinal solution of the problem.

The purpose of this work is to study the reflection of atto- and femtosecond pulses from MSs by numerical methods. The ways of overcoming restrictions on the reflection of extremely short signals will be considered. The key idea consists in a search for aperiodic MSs possessing simultaneously a broad ($\Delta\omega/\omega \sim 1/2$) reflectivity spectrum and the appropriate dependence of group delay on frequency. Such a statement of the problem corresponds to the inverse problem of multilayer optics which takes into account the modulus and phase of $r(\omega)$.

The computing method is partially described in [7]. It is assumed that the MS consist of N alternating layers of materials A and B. The simulation of pulse reflection from a given MS includes the following principal steps:

Calculation of the complex amplitude reflection coefficient $r(\omega)$ as a function of frequency by the recurrent relation method [10]. The complex dielectric constants are expressed through the atomic scattering factors $f_{1,2}$ [11];

Spectral decomposition of the incident pulse field $E_0(t)$, multiplying each Fourier component $E_0(\omega)$ by $r(\omega)$, and inverse Fourier transform with the object of determining the reflected pulse field $E(t)$:

$$E_0(\omega) = \int_{-\infty}^{\infty} E_0(t)\exp(-i\omega t)dt, \tag{1}$$

$$E(t) = \frac{1}{2\pi}\int_{-\infty}^{\infty} E(\omega)\exp(i\omega t)d\omega, \quad \text{where } E(\omega) = E_0(\omega)r(\omega). \tag{2}$$

Here, $E_0(\omega)$ and $E(\omega)$ are the Fourier transforms of the incident and reflected field. The index "0" refers to the incident pulse. To determine the modulus and phase of each Fourier component for the reflected signal, both the modulus and the phase of $r(\omega)$ were used. The reflected pulse field obtained by procedure (1) and (2) carries information about a change in the amplitude and shape of the reflected pulse and about its time delay relative to the incident pulse.

The incident pulses were assumed to be Gaussian with parameters τ_0, ω_0, and b:

$$E_0(t) = \exp\left[-\frac{\pi}{2}(t/\tau_0)^2\right]\cos(\omega_0 t + bt^2), \quad I_0(t) = E_0(t)^2, \tag{3}$$

where b is the chirp parameter. By the pulse duration τ is meant the effective width of intensity envelope $\tilde{I}(t)$:

$$\tau = \int_{-\infty}^{\infty} \tilde{I}(t)dt/I_{\max}.$$

The pulse reflection coefficient is defined as the reflected-to-incident pulse energy ratio,

$$R = \int_{-\infty}^{\infty} I(t)dt/\int_{-\infty}^{\infty} I_0(t)dt.$$

The power reflection coefficient, defined as $R_P = R(\tau_0/\tau)$, virtually coincides with the peak intensity ratio $I_{\max}/I_{0\max}$ and plays an important role.

Below, the periodic MSs are considered by the examples of two normal-incidence Mo/Si mirrors optimized to maximal $|r(\omega_0)|^2$ for photons with energy $\hbar\omega_0 = 77.6$ eV (wave period $T = 0.053$ fs) (Table 1) and two grazing-incidence Ni/C and Os/C mirrors for $\hbar\omega_0 = 20$ keV (Table 2); $\tau_{\min} = T(\omega_0/\Delta\omega)$ is the expected minimal duration of a pulse reflected without sizable loss of efficiency, as compared to the reflection of a narrowband pulse.

Figure 1 shows the intensity envelopes of the reflected pulses for unchirped ($b = 0$) pulses (3) incident on MS-1. Zero time corresponds to the maximal intensity of incident pulse.

In Fig. 2, the energy reflection coefficients of MS are shown as functions of the reflected pulse duration. The pulses longer than 1 fs are reflected from MS-1 practically like the infinitely long ones. For a pulse duration shorter than ~0.9 fs, the pulse spectrum becomes broader than the MS reflectivity spectrum, and the reflection coefficient starts to decrease. If one specifies a certain minimal allowable reflection coefficient, i.e., 0.2, then the duration of the shortest reflected pulse will be $\tau = 0.38$ fs. The duration of the corresponding initial pulse is $\tau_0 = 0.12$ fs, and the loss of power is ~16 ($R_p = 0.06$).

For the MS-2, $|r(\omega_0)|^2$ is several times smaller, but the reflectivity spectrum is 2.5 times broader. Because of this, the MS-2 becomes more efficient for the pulses with $\tau < 0.4$ fs than MS-1, and it can reflect pulses of duration up to $\tau = 0.25$ fs without noticeable efficiency loss. For the reflected pulse of duration $\tau = 0.25$ fs, $R_p = 0.14$ and $|r(\omega_0)|^2 = 0.19$ ($\tau_0 = 0.18$ fs).

Let us now consider the reflection of hard X-ray pulses (Table 2). In this case, the relative reflectivity bands of the periodic grazing-incidence MSs lie in the range 0.01–0.04. Because of this, the duration of the shortest pulses reflected from the mirrors is equal to several tens of light periods. Figure 3 shows the energy reflection coefficients of periodic MSs for the photon

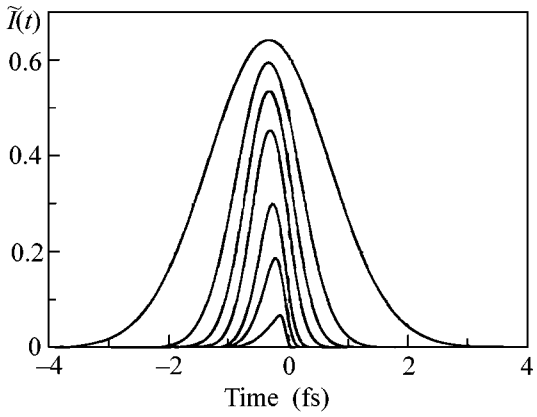

Fig. 1. Envelopes of the pulses reflected from the periodic MS-1. In order of increasing duration of the incident pulse: τ_0 = 0.1, 0.2, 0.3, 0.5, 0.7, 1, and 2 fs.

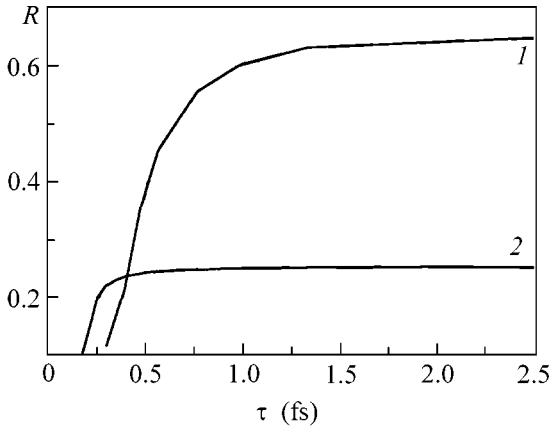

Fig. 2. Energy reflection coefficient of the periodic MS as a function of the reflected pulse duration: (*1*) MS-1 and (*2*) MS- 2.

energy $\hbar\omega_0$ = 20 keV (T = 0.21 as) and a grazing angle of 0.01 rad.

Although possessing smaller $|r(\omega_0)|^2$, the MS based on Os/C better reflects the pulses shorter than 60 as, but its efficiency decreases drastically for the pulses shorter than 10 as. Thus, the periodic MSs are unsuitable for the durations shorter than ~$1/\Delta\omega$.

The aperiodic MSs offer new possibilities. For them, the spectral width ceases to be the major constraint. The pulses lengthen upon the reflection from the aperiodic MSs primarily because of a large difference in the group delays $\Delta t_g \sim (d^2\Phi/d\omega^2)\Delta\omega$. The higher the frequency, the longer the path traversed by radiation, which results in pulse smearing.

However, this effect can be used for shortening the chirped pulses with higher frequency at their leading edge. (The transformations of this type have been employed in the visible region over the last several years [12]). It was shown, both theoretically [6–8] and experimentally [9], that aperiodic MSs can have a broad and uniform reflectivity band. The band broadening leads to a considerable increase in the integral reflectivity

$$\mathcal{I} = \int |r(\omega)|^2 d\omega.$$

In particular, we calculated the aperiodic grazing-incidence MS (Mo/Si) with the uniform reflectivity $|r(\omega)|^2 = 0.23$ in the range 65–95 eV. Figure 4 shows the $|r(\omega)|^2$ and $\Phi(\omega)$ functions for this aperiodic MS. The ratio $\omega_0/\Delta\omega \approx 2.5$ corresponds to the minimal pulse duration on the order of $2.5T \approx 0.13$ fs, provided that the spectral components of the reflected pulse are completely phased. The behavior of the $\Phi(\omega)$ phase in the vicinity of ω_0 resembles the function

$$\Phi(\omega) = c_0 + c_1(\omega - \omega_0) + c_2(\omega - \omega_0)^2. \qquad (4)$$

The resulting group delay $d\Phi/d\omega = c_1 + 2c_2(\omega - \omega_0)$ depends linearly on the difference $\omega - \omega_0$. One can thus expect that the simple linear chirp of form (3) with $b = 1/4c_2$ will provide a good pulse compression upon the reflection from the indicated aperiodic MS (Fig. 4). Figure 5 shows the envelopes of the incident and (dot-

Table 1. Characteristics of periodic normal-incidence Mo/Si MSs ($\hbar\omega_0$ = 77.6 eV)

	Number of layers N	Period d, Å	Mo fraction, γ	$\lvert r(\omega_0)\rvert^2$	$\omega_0/\Delta\omega$ (N_{eff})	$\tau_{\min}$, fs
MS-1	80	82.6	0.32	0.65	16(13)	0.9
MS-2	10	85.6	0.50	0.25	6(5)	0.3

Table 2. Characteristics of periodic grazing-incidence MSs ($\hbar\omega_0$ = 20 keV)

	Number of layers N	Period d, Å	Ni(Os) fraction, γ	$\lvert r(\omega_0)\rvert^2$	$\omega_0/\Delta\omega$ (N_{eff})	$\tau_{\min}$, as
Ni/C	800	31.4	0.16	0.967	85(76)	18
Os/C	140	31.5	0.24	0.898	27(30)	6

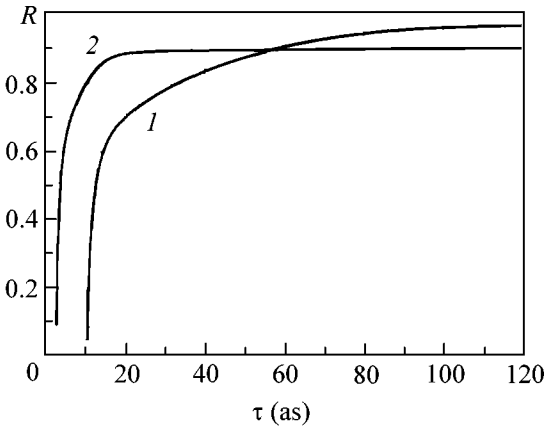

Fig. 3. Energy reflection coefficient of the periodic MS (Table 2) as a function of the reflected pulse duration: (*1*) Ni/C and (*2*) Os/C.

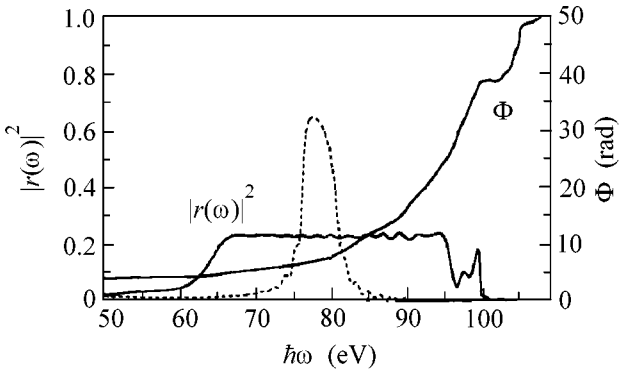

Fig. 4. Reflectivity $|r(\omega)|^2$ and phase $\Phi(\omega)$ of an aperiodic MS optimized to maximal uniform reflectivity in the range 65–95 eV. The dotted line is the reflectivity of the periodic MS-1.

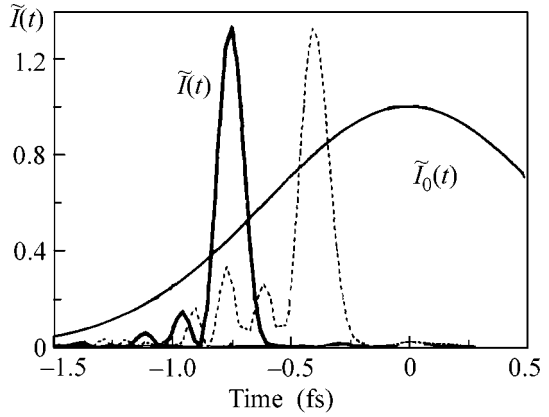

Fig. 5. Envelopes of the incident chirped pulse $\tilde{I}_0(t)$ and the pulses reflected from aperiodic MSs optimized to maximal uniform reflectivity in the range 65–95 eV (solid line) with and (dotted line) without taking into account the phase of the complex reflection coefficient.

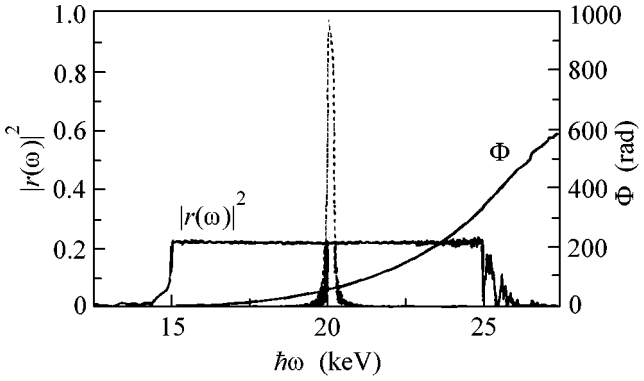

Fig. 6. Reflectivity and phase of the aperiodic MS (Ni/C, 800 layers) optimized to the maximal uniform reflectivity in the range 15–25 keV for a grazing incidence angle of 0.01 rad. The dotted line is the reflectivity of a periodic MS (Table 2).

ted line) reflected pulses for the optimal chirp parameter. The effective duration of the reflected pulse is 0.21 fs. Therefore, the aperiodic MS provides sevenfold compression of a pulse ~1.5 fs in duration with power reflection coefficient of 1.3.

Let us now require that, along with the uniform reflectivity in the range 65–95 eV, the phase $\Phi(\omega)$ of the aperiodic MS be approximated by function (4) over the entire range. The aperiodic MS thus obtained possesses slightly lower reflectivity $|r(\omega)|^2 = 18.5\%$. The effective duration of the reflected pulse (solid line in Fig. 5) is equal to 0.15 fs (three wave periods), signifying that the fundamental duration limit corresponding to the reflectivity band of aperiodic MS is achieved.

As a rule, N_{eff} in the MSs designed for the operation in the hard X-ray region is appreciably larger than in the structures for the soft X-ray region. This is precisely the reason why the aperiodic MSs for the hard X-ray region should be capable of compressing many fold the chirped pulses. Figure 6 shows the reflectivity and the phase of an aperiodic MS (Ni/C; 800 monolayers) optimized to the maximum uniform reflectivity in the range 15–25 keV for a grazing incidence angle of 0.01 rad. The optimal chirp parameter was found to be $b = 8.84\ \text{as}^{-2}$, allowing the pulse with $\tau_0 = 50$ as to be compressed to 4.3 as with a power reflection coefficient of 2.45 and energy reflection coefficient of 21%. The reflectivity of the aperiodic Ni/C MS optimized simultaneously for the reflectivity and phase $\Phi(\omega)$ of form (4) is lower and equal to 17.4%. Nevertheless, this MS provides much better compression of the chirped pulse and a power reflection coefficient greater than 6.3 (Fig. 7). The duration of the initial pulse is 25 as, while the duration of the reflected pulse is 0.69 as (28-fold compression). The duration of the reflected pulse is

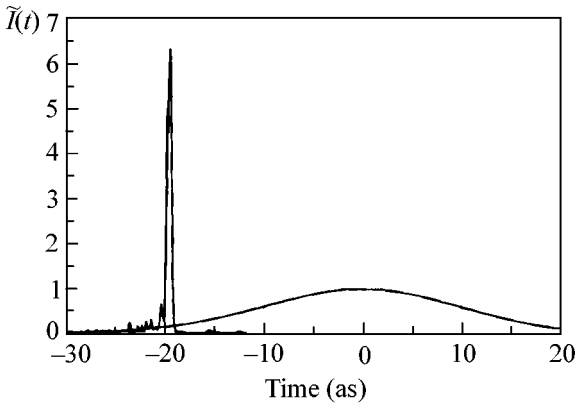

Fig. 7. Envelopes of the incident chirped pulse and the pulse reflected from the aperiodic MS optimized to maximal uniform reflectivity in the range 15–25 eV, as calculated with allowance made for the phase of the complex reflection coefficient.

equal to three wave periods, which is close to the fundamental limit for this MS.

Thus, for the MSs commonly used in the soft X-ray region, a decrease in the pulse reflection coefficient and pulse shape distortion are observed for the pulses of femtosecond duration and shorter. However, one can construct special aperiodic MSs that are capable of reflecting pulses containing only three wave periods (0.15 fs in the soft X-ray region and less than 1 as in the hard X-ray region). The chirped pulses can be strongly compressed, and the corresponding power reflection coefficients can be higher than unity. The optimal aperiodic MSs can be calculated by solving the inverse problem of multilayer X-ray optics with account taken of the amplitude and phase of the complex reflection coefficient.

This work was supported by the Russian Foundation for Basic Research, project nos. 00-02-17717 and 00-02-17825.

REFERENCES

1. N. G. Basov, A. N. Oraevskiĭ, and B. N. Chichkov, Zh. Éksp. Teor. Fiz. **89**, 66 (1985) [Sov. Phys. JETP **62**, 37 (1985)].
2. V. T. Platonenko, V. V. Strelkov, and F. V. Ignatovich, Kvantovaya Élektron. (Moscow) **28**, 43 (1999).
3. A. Rundquist, C. G. Durfee III, Z. Chang, *et al.*, Science **280**, 1412 (1998).
4. R. Fitzgerald, Phys. Today **53** (9), 24 (2000).
5. *Shortcut for X-ray Pulses*, Phys. World **14** (March), 3 (2001).
6. N. N. Kolachevskiĭ, A. S. Pirozhkov, and E. N. Ragozin, Kratk. Soobshch. Fiz., No. 12, 55 (1998).
7. E. Ziegler, I. N. Bukreeva, I. V. Kozhevnikov, *et al.*, Proc. SPIE **3737**, 386 (1999).
8. N. N. Kolachevskiĭ, A. S. Pirozhkov, and E. N. Ragozin, Kvantovaya Élektron. (Moscow) **30**, 428 (2000).
9. V. V. Kondratenko, V. E. Levashov, Yu. P. Pershin, *et al.*, Kratk. Soobshch. Fiz., No. 7 (in press).
10. A. V. Vinogradov, I. A. Brytov, A. Ya. Grudskiĭ, *et al.*, *Mirror X-ray Optics* (Mashinostroenie, Leningrad, 1989).
11. R. Soufli and E. M. Gullikson, Proc. SPIE **3113**, 222 (1997); http://cindy.lbl.gov/opticalconstants/.
12. R. Szipöcs, K. Ferencz, C. Spielmann, and F. Krausz, Opt. Lett. **19**, 201 (1994).

Translated by V. Sakun

JETP Letters, Vol. 74, No. 3, 2001, pp. 154–158. Translated from Pis'ma v Zhurnal Éksperimental'noĭ i Teoreticheskoĭ Fiziki, Vol. 74, No. 3, 2001, pp. 172–176.

Influence of a Magnetic Field on the Light-Induced Ion Drift

A. I. Parkhomenko

Institute of Automatics and Electrometry, Siberian Division, Russian Academy of Sciences, Universitetskiĭ pr. 1, Novosibirsk, 630090 Russia

e-mail: par@iae.nsk.su

Received May 3, 2001; in final form, July 2, 2001

It is shown that the velocity component transverse to the radiation propagation direction can arise in the light-induced ion drift (LIID) after applying an external magnetic field to a weakly ionized gas. It is predicted that the projection of the ion drift velocity onto the radiation direction changes its sign with an increase in the magnetic field, resulting in the anomalous LIID. *© 2001 MAIK "Nauka/Interperiodica".*

PACS numbers: 32.80.Lg; 42.50.Vk

Among the known radiation effects on the translational motion of particles, light-induced drift (LID) is one of the strongest [1, 2]. The essence of this effect is that the macroscopic motion of particles absorbing radiation in a mixture with buffer particles becomes directed. Let us recall the origin of this phenomenon. Due to the Doppler effect, the light action on the absorbing particles is velocity-selective, resulting in the oppositely directed effective "beams" of particles in the excited and ground states. In the buffer gas atmosphere, these beams experience different drags because of the difference in the transport collision frequencies of the excited and unexcited particles. As a result, gas of absorbing particles, as a whole, acquires directed motion. The drift velocity is proportional to the relative difference $(\nu_n - \nu_m)/\nu_n$ in the transport frequencies of the ground-state (ν_n) and excited- state (ν_m) resonant particles in their collisions with the buffer particles.

Under optimum conditions, the LID effect can surpass the well- known light-pressure effect by several orders of magnitude. Theoretically, the LID velocity can reach a value of thermal velocity upon laser excitation [3]. It has been demonstrated experimentally that, under the action of LID, the atoms can drift with velocities on the order of several tens of meters per second [4].

The vast majority of theoretical and experimental works on LID were devoted to studying the drift of atoms and molecules in gaseous media (see, e.g., [3–11] and bibliography cited therein). The theoretical description of the LID of neutral atoms applies equally to the ions in a weakly ionized gas in the absence of external electric and magnetic fields [12].

It is easy to understand from simple physical considerations that the external magnetic field can strongly affect the LID of atoms, molecules, and ions. Two aspects of this influence can be distinguished: spectral and force. The spectral aspect of the influence of a magnetic field on the LID is caused by the Zeeman splitting of the absorption line; it is relevant to arbitrary (neutral or charged) particles. The force effect of a magnetic field on the LID occurs only for ions; it is caused by the Lorentz force acting on the drifting ions in a magnetic field.

Until now, the influence of a magnetic field on the LID has been poorly understood. The studies on this problem are limited to works [13–15]. The spectral aspect of the influence of a magnetic field on the LID was demonstrated in experimental work [13], where neutral atoms were spatially localized and accumulated using the LID effect. The force aspect of the influence of a magnetic field on the light-induced ion drift (LIID) was theoretically investigated in [14, 15]. Unfortunately, the results of these works cannot lay claim to reliability because the influence of a magnetic field on the LIID was incorrectly taken into account in the equations used therein.

Thus, in fact, no correct analysis of the force aspect of the effect of a magnetic field on the LIID has been carried out so far. It is the purpose of this work to partially fill this gap and explore theoretically the force aspect of the influence of a magnetic field on the LIID. It was found that the magnetic field cardinally modifies the pattern of the LIID effect.

Let us consider a three-component weakly ionized gas subjected to a static uniform magnetic field **B** and consisting of electrons, singly charged positive ions of the same sort, and neutral atoms. The collisions between the charged particles in a weakly ionized gas are immaterial because the collision frequencies of electrons and ions with neutrals are considerably higher than the collision frequencies between the charged particles (at a temperature of ~0.1 eV, this condition implies that the degree of gas ionization is $\lesssim 10^{-4}$ [16]). Let the radiation in the form of a traveling monochro-

0021-3640/01/7403-0154$21.00

matic wave be resonantly absorbed at the $m - n$ transition between the ground n and the first excited m ion levels. In what follows, I focus only on the force action of a magnetic field on the ion drift, so I will restrict myself to the consideration of the simplest situation where the Zeeman splitting of an absorption line can be ignored. For example, the line remains unsplit in the case of the normal Zeeman effect (the Landé g factors of the combining m and n states are identical) if the propagation direction of the radiation linearly polarized along magnetic field **B** is transverse to **B**.

Under these conditions, the interaction of radiation with two-level particles (ions) is governed by the following equations for the density matrix [5, 17]:

$$\begin{aligned}
&\left[\frac{d}{dt} + \Gamma_m\right]\rho_m(\mathbf{v}) = S_m(\mathbf{v}) + NP(\mathbf{v}),\\
&\frac{d}{dt}\rho_n(\mathbf{v}) = S_n(\mathbf{v}) + \Gamma_m\rho_m(\mathbf{v}) - NP(\mathbf{v}),\\
&\left[\frac{d}{dt} + \frac{\Gamma_m}{2} - i(\Omega - \mathbf{kv})\right]\rho_{mn}(\mathbf{v})\\
&\quad = S_{mn}(\mathbf{v}) + iG[\rho_n(\mathbf{v}) - \rho_m(\mathbf{v})],
\end{aligned} \tag{1}$$

where

$$\begin{aligned}
&\frac{d}{dt} \equiv \frac{\partial}{\partial t} + \mathbf{v}\frac{\partial}{\partial \mathbf{r}} + \omega_c[\mathbf{vh}]\frac{\partial}{\partial \mathbf{v}},\\
&NP(\mathbf{v}) = -2\mathrm{Re}[iG^*\rho_{mn}(\mathbf{v})],\\
&\omega_c = \frac{eB}{Mc}, \quad \mathbf{h} \equiv \frac{\mathbf{B}}{B}, \quad |G|^2 = \frac{B_{nm}I}{2\pi},\\
&B_{nm} = \frac{\lambda^2\Gamma_m}{4\hbar\omega}, \quad \Omega = \omega - \omega_{mn}.
\end{aligned} \tag{2}$$

Here, $\rho_i(\mathbf{v})$) is the ion velocity distribution for the ith ($i = m$ and n) level; N is the total concentration of ions; $S_m(\mathbf{v})$, $S_n(\mathbf{v})$, and $S_{mn}(\mathbf{v})$ are the collision integrals; ω, λ, and $\mathbf{k}$ are the radiation frequency, wavelength, and wave vector, respectively; Γ_m is the spontaneous decay rate in the excited state m; ω_{mn} is the m–n transition frequency; B_{nm} is the second Einstein coefficient for the m–n transition; I is the radiation intensity; $P(\mathbf{v})$ is the number of absorption events in unit time for the ion with velocity **v** in the unit velocity interval; ω_c is the ion cyclotron frequency; **B** is the magnetic field; e is the elementary electric (positive) charge; and M is the ion mass.

Equations (1) do not take into account the internal electric field **E** in the medium. This field can arise if the ions, as a whole, execute directed motion due to the LID effect, and it can safely be ignored if the concentration of charged particles is not high enough for the ionized gas to exhibit plasma properties (the Debye radius r_d characterizing the spatial separation of charged particles is considerably larger than the characteristic size L of the system). In plasma ($r_d \ll L$), the directed motion of ions induces directed motion of electrons because of the quasi-neutrality requirement. This gives rise to the internal electric field **E**, which compensates the friction force between the electrons and buffer particles (neutral atoms). An analysis shows that electrons under plasma conditions have no effect on the LIID [i.e., the field **E** can be ignored in Eqs. (1)] if the magnetic field is so weak that $\omega_c^2 \ll \nu_n\nu_e m/M$, where ν_n and ν_e are the average transport frequencies of the ions and electrons in their collisions with the buffer particles, and m is electron mass.

In cases where the particle velocity distribution functions differ only slightly from the Maxwellian distribution, kinetic Eq. (1) can adequately be solved by the Grad method (moments method) [16, 18]. In this work, these equations are solved using the simplest approximation of the Grad method, according to which the dependence of density matrix elements on the velocity is represented in Eqs. (1) as the sum of equilibrium distribution $N_iW(\mathbf{v})$ and the antisymmetric correction:

$$\rho_i(\mathbf{v}) = \left[N_i + \frac{2}{\bar{v}^2}\mathbf{v}\mathbf{j}_i\right]W(\mathbf{v}), \quad i = m, n, mn, \tag{3}$$

where

$$N_i = \int\rho_i(\mathbf{v})d\mathbf{v}, \quad \mathbf{j}_i = \int\mathbf{v}\rho_i(\mathbf{v})d\mathbf{v}. \tag{4}$$

Here, N_m and N_n are the ion concentrations in the states m and n, respectively; $\mathbf{j}_m$ and $\mathbf{j}_n$ are the ion flows in the states m and n, respectively; $\bar{v} = \sqrt{2k_BT/M}$ is the most probable ion velocity; T is temperature; and k_B is the Boltzmann constant. Representation (3) is valid if the ion interaction with radiation is low-velocity-selective, i.e., if the absorption line is homogeneously broadened, $\Gamma \gg k\bar{v}$, where Γ is the homogeneous halfwidth of the ion absorption line and $k\bar{v}$ is its Doppler width.[1]

The expression for the nondiagonal collision integral $S_{mn}(\mathbf{v})$ in Eq. (1) will be taken in the form that is often used in nonlinear spectroscopy [5, 17]:

$$S_{mn}(\mathbf{v}) = -\left(\Gamma - \frac{\Gamma_m}{2}\right)\rho_{mn}(\mathbf{v}), \tag{5}$$

which means that the phase of the oscillating dipole moment is completely lost upon collisions.

The inelastic collisions (ionization, recombination, etc.) are immaterial for the problem of interest (the effective ionization and recombination frequencies are small compared to the frequency of elastic collisions), so that only the elastic ion collisions with buffer parti-

[1] In the case of a broadband radiation with a smooth spectral shape within the width of an absorption line, approximation (3) is valid for an arbitrary ratio of Γ to $k\bar{v}$.

cles (neutral atoms) will be taken into account in what follows. For elastic collisions, the diagonal collision integrals in Eq. (1) obey the relationship $\int S_i(\mathbf{v})d\mathbf{v} = 0$, which implies the conservation of the total number of particles (ions in the state m or n).

For the first moment of diagonal collision integrals, the following relationship is valid in approximation (3) (see, e.g., [2]):

$$\int \mathbf{v} S_i(\mathbf{v})d\mathbf{v} = -\nu_i \mathbf{j}_i, \quad i = m, n, \tag{6}$$

where ν_i is the effective (average) transport collision frequency related to the diffusion coefficient D_i of ions in the state i by the simple formula $D_i = \bar{v}^2/2\nu_i$.

Under stationary and spatially homogeneous conditions, one finds from the solution to the system of equations for the first and second moments of Eqs. (1) that, in the case of the radiation propagation direction perpendicular to the magnetic field ($\mathbf{k} \perp \mathbf{B}$), the ion drift velocity is equal to the sum of two mutually perpendicular components $\mathbf{u}_\parallel$ and $\mathbf{u}_\perp$:

$$\mathbf{u} \equiv \frac{\mathbf{j}_m + \mathbf{j}_n}{N} = \mathbf{u}_\parallel + \mathbf{u}_\perp, \tag{7}$$

where the component $\mathbf{u}_\parallel$ is parallel to the wave vector $\mathbf{k}$, while the component $\mathbf{u}_\perp$ is perpendicular to $\mathbf{k}$ and $\mathbf{B}$:

$$\mathbf{u}_\parallel = \frac{\mathbf{k}}{k} u_\parallel, \quad \mathbf{u}_\perp = \frac{[\mathbf{kB}]}{kB} u_\perp. \tag{8}$$

For an arbitrary radiation intensity, the formulas for the projections $u_\parallel$ and $u_\perp$ of drift velocity are rather cumbersome, but they are greatly simplified in the limit of weak radiation intensity $I \ll 2\pi\hbar\omega\Gamma/\lambda^2$. In this limit, the formulas, to small terms on the order of $(k\bar{v}/\Gamma)^2 \ll 1$, take the form

$$u_\parallel = u_0 \left\{ 1 - \frac{\omega_c^2}{\nu_n(\Gamma_m + \nu_m)} \times \left[1 + \frac{(3\Gamma^2 + \omega_c^2 - \Omega^2)(\Gamma_m + \nu_m + \nu_n)}{2\Gamma(\Gamma^2 + \Omega^2)} \right] \right\}, \tag{9}$$

$$u_\perp = u_0 \frac{\omega_c(\Gamma_m + \nu_m + \nu_n)}{\nu_n(\Gamma_m + \nu_m)} \times \left\{ 1 + \frac{(3\Gamma^2 + \omega_c^2 - \Omega^2)[(\Gamma_m + \nu_m)\nu_n - \omega_c^2]}{2\Gamma(\Gamma^2 + \Omega^2)(\Gamma_m + \nu_m + \nu_n)} \right\}, \tag{10}$$

where

$$u_0 = \bar{v}\tau_\sigma P\varphi, \quad P = \frac{2|G|^2\Gamma}{\Gamma^2 + \Omega^2},$$

$$\tau_\sigma = \frac{\nu_n - \nu_m}{\left[\nu_n + \dfrac{\omega_c^2}{\nu_n}\right]\left[\Gamma_m + \nu_m + \dfrac{\omega_c^2}{\Gamma_m + \nu_m}\right]}, \tag{11}$$

$$\varphi = \frac{\Omega k \bar{v}(\Gamma^2 + \Omega^2)}{[\Gamma^2 + (\Omega + \omega_c)^2][\Gamma^2 + (\Omega - \omega_c)^2]},$$

and $P \equiv \int P(\mathbf{v})d\mathbf{v}$ is the number of absorption events in unit time. In the absence of magnetic field ($\omega_c = 0$), Eqs. (9)–(11), as expected, give the known expression for the LID velocity in the case of a homogeneously broadened absorption line [1, 2].

The projections $u_\parallel$ and $u_\perp$ of drift velocity calculated using Eqs. (9) and (10) are presented in Fig. 1. The quantity

$$u_{\max} = \bar{v}\frac{|\nu_n - \nu_m|}{\nu_n}\frac{k\bar{v}}{\Gamma_m + \nu_m}\frac{3\sqrt{3}|G|^2}{8\Gamma^2} \tag{12}$$

is taken as a velocity unit. It is equal to the maximal (at $|\Omega| = \Gamma/\sqrt{3}$) value of ion drift velocity in the absence of a magnetic field.

One can see from Fig. 1 that the projection $u_\parallel$ of drift velocity $\mathbf{u}$ onto the radiation direction changes sign with increasing the magnetic field. It is seen from Eq. (9) that this occurs in the range of cyclotron frequencies $\omega_c \sim \sqrt{\nu_n(\Gamma_m + \nu_m)}$.

The physical reasons for changing the direction of ion drift velocity with increasing magnetic field can be understood from the following qualitative considerations. In the absence of a magnetic field, the drift velocity $u_\parallel$ is proportional to the difference $\nu_n - \nu_m$ in the transport collision frequencies of ions in the ground and excited states. In the presence of a magnetic field, the field-transverse diffusion coefficient D_{iB} of ions in the state i is $D_{iB} = \bar{v}^2/2\nu_{iB}$, where the quantity $\nu_{iB} = \nu_i + \omega_c^2/\nu_i$ has a meaning of the effective transport collision frequency of ions in the state i colliding with the buffer particles in the presence of magnetic field [16]. Consequently, if a magnetic field is perpendicular to the direction of radiation propagation, one can expect that (estimatively) $u_\parallel \propto \nu_{nB} - \nu_{mB} \propto (\nu_m - \nu_n)(\omega_c^2 - \nu_m\nu_n)$. From this it follows that the projection of ion drift velocity onto the radiation direction changes sign with increasing magnetic field. A change in the drift direction is caused by the fact that the difference $\nu_{nB} - \nu_{mB}$ in the effective transport collision frequencies of ions changes its sign with increasing magnetic field.

Curves *1* and *3* in Fig. 1 correspond to the normal LIID effect with the characteristic dispersion-like frequency dependence of the drift velocity $u_{\|}(\Omega)$ (to a sign, derivative of the absorption line contour with respect to frequency) and one zero at zero value of detuning Ω from the radiation frequency. Curve *2* in Fig. 1a with three zeros corresponds to the so-called anomalous LID[2] [9–11] with the sharp deviation of the frequency dependence of drift velocity $u_{\|}(\Omega)$ from the dispersion-like curve. The anomalous LID arises at ion cyclotron frequencies where $\omega_c \sim \sqrt{\nu_n(\Gamma_m + \nu_m)}$. An analysis shows that the interval $\Delta\omega_c$ of cyclotron frequencies where the anomalous LID is observed equals $\Delta\omega_c \approx 0.2\nu_n$.

As was realized in a number of works (see, e.g., [19] and the bibliography cited therein), the anomalous LID in the absence of external fields is fully caused by the dependence of transport collision frequencies on the velocity v of resonant particles, and the anomaly can arise only if the difference in the transport collision frequencies for the combining (i.e., involved in the radiation absorption) levels as a function of v changes sign. The results of this work demonstrate that the anomalous LIID in an external field can arise even if the transport collision frequencies are independent of velocity.

Plots of the projection $u_\perp$ of drift velocity **u** onto the direction transverse to the wave vector **k** vs. the frequency detuning are shown in Fig. 1b for different magnetic fields. The absolute (with respect to Ω and ω_c) maximum of velocity $u_\perp$ occurs at $\omega_c \sim \nu_n/2$; it is close to the absolute maximum of velocity $u_{\|}$, which is achieved at $\omega_c \longrightarrow 0$ [it is seen from the comparison of curves *1* in Figs. 1a and 1b that $|(u_\perp)_{\max}| \approx 0.7|(u_{\|})_{\max}|$. The anomalous LIID in the direction transverse to the wave vector **k** arises at $\omega_c \gtrsim 3\nu_n$ (curve *2* in Fig. 1b).

Note that Eqs. (9) and (10), although derived for the ion drift under the influence of a traveling monochromatic light wave, can naturally be extended to the broadband radiation with an arbitrary spectral intensity $I(\omega)$. To do this, it will suffice to replace the radiation intensity I entering the $|G|^2$ factor in the expression for P in Eq. (11) by the frequency-dependent spectral intensity $I(\omega)$ and then integrate modified formulas (9) and (10) for the drift velocity $\mathbf{u}(\omega)$ over ω in infinite limits. The resulting formulas are also valid for the Doppler-broadened ($k\bar{v} \gg \Gamma$) absorption line if the spectrum of the broadband radiation is smooth within the absorption line width (see footnote 1).

[2] In 1992, a sharp deviation of the frequency dependence of drift velocity from the dispersion-like curve was unexpectedly observed in the LID of C_2H_4 molecules in a buffer Kr gas [9]; an anomalous profile with three zeros was observed for the LID velocity, instead of one zero, as might be expected according to the previous LID theory with velocity-independent transport collision frequencies. The deviation from the predictions of the theory was so strong that the effect was called the "anomalous" LID.

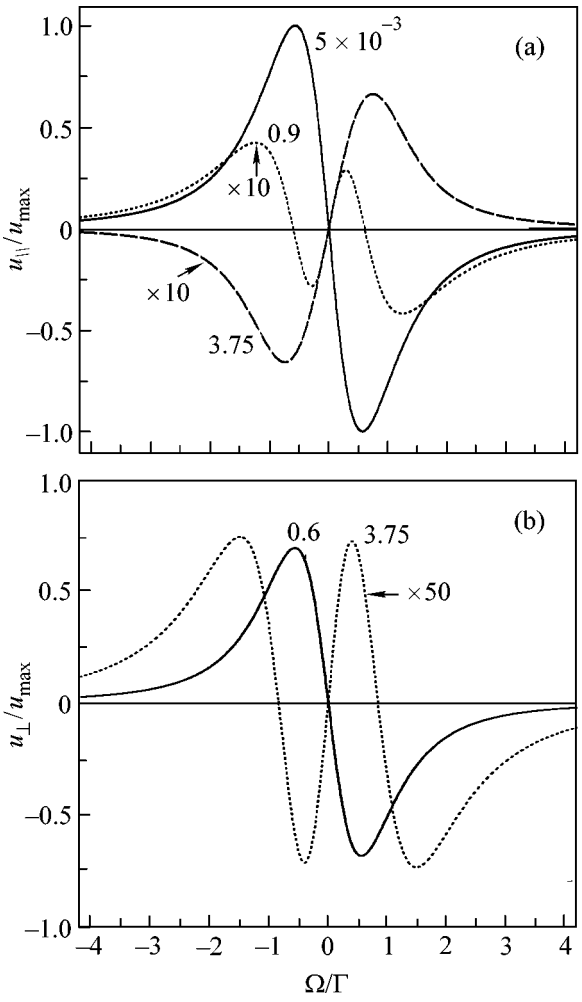

Fig. 1. Plots of projections $u_{\|}$ and $u_\perp$ of ion drift velocity **u** vs. radiation frequency detuning Ω for different values of ion cyclotron frequency. The values of ratio ω_c/ν_n are indicated near the curves.

Note also that the formulas deduced in this work for the drift velocity **u** can be applied (in compliance with the results of work [3]) to the particular case of broadband radiation with Lorentzian spectrum through the substitution $\Gamma \longrightarrow \Gamma + \delta$, where δ is the halfwidth of the radiation spectrum. In this case, the frequency detuning Ω in Eqs. (9) and (10) is the difference between the center of the Lorentzian radiation curve and the transition frequency ω_{mn}. The condition $\Gamma > k\bar{v}$ for the validity of Eqs. (9) and (10) then transforms to $\Gamma + \delta > k\bar{v}$; the latter can be satisfied for gas pressures as low as one likes if the radiation line halfwidth $\delta > k\bar{v}$. This fact is used below to estimate the magnitude of the magnetic field necessary for the experimental observation of some of the characteristic features of ion drift that are described in this work.

To observe a change in the drift direction along **k** and the anomalous (along **k**) LIID, a magnetic field

must provide cyclotron frequency $\omega_c \sim \sqrt{\nu_n(\Gamma_m + \nu_m)}$. For transitions in the visible region, one has $\Gamma_m \sim 10^8$ s^{-1}, and, for the transport collision frequency of ions $\nu_m \sim \nu_n \sim 10^6$ s^{-1} (this corresponds to a gas pressure of ~0.1 torr), one obtains the estimate $\omega_c \sim 10^7$ s^{-1}. With the ion mass $M \sim 20$ amu, this cyclotron frequency is achieved in magnetic fields $B \sim 2 \times 10^4$ G.

I am grateful to A.M. Shalagin for discussion and valuable remarks and to F.Kh. Gel'mukhanov and L.V. Il'ichev for discussion and attention to the work. This work was supported by the Russian Foundation for Basic Research, project no. 01-02-17433.

REFERENCES

1. F. Kh. Gel'mukhanov and A. M. Shalagin, Pis'ma Zh. Éksp. Teor. Fiz. **29**, 773 (1979) [JETP Lett. **29**, 711 (1979)].
2. F. Kh. Gel'mukhanov and A. M. Shalagin, Zh. Éksp. Teor. Fiz. **78**, 1674 (1980) [Sov. Phys. JETP **51**, 839 (1980)].
3. A. K. Popov, A. M. Shalagin, V. M. Shalaev, and V. Z. Yakhnin, Zh. Éksp. Teor. Fiz. **80**, 2175 (1981) [Sov. Phys. JETP **53**, 1134 (1981)].
4. S. N. Atutov, I. M. Ermolaev, and A. M. Shalagin, Zh. Éksp. Teor. Fiz. **92**, 1215 (1987) [Sov. Phys. JETP **65**, 679 (1987)].
5. S. G. Rautian and A. M. Shalagin, *Kinetic Problems of Nonlinear Spectroscopy* (North-Holland, Amsterdam, 1991).
6. P. L. Chapovskiĭ, Izv. Akad. Nauk SSSR, Ser. Fiz. **53**, 1069 (1989).
7. G. Nienhuis, Phys. Rep. **138**, 151 (1986).
8. H. G. C. Werij and J. P. Woerdman, Phys. Rep. **169**, 145 (1988).
9. G. J. van der Meer, J. Smeets, S. P. Pod'yachev, and L. J. F. Hermans, Phys. Rev. A **45**, R1303 (1992).
10. E. J. van Duijn, R. Nokhai, and L. J. F. Hermans, J. Chem. Phys. **105**, 6375 (1996).
11. F. Yahyaei-Moayyed and A. D. Streater, Phys. Rev. A **53**, 4331 (1996).
12. F. Kh. Gel'mukhanov and A. M. Shalagin, Kvantovaya Élektron. (Moscow) **8**, 590 (1981).
13. S. N. Atutov, S. P. Pod'yachev, and A. M. Shalagin, Opt. Commun. **83**, 307 (1991).
14. S. Dattagupta, R. Ghosh, and J. Singh, Phys. Rev. Lett. **83**, 710 (1999).
15. J. Singh, R. Ghosh, and S. Dattagupta, Phys. Rev. A **61**, 025402 (2000).
16. V. E. Golant, A. P. Zhilinskii, and I. E. Sakharov, *Fundamentals of Plasma Physics* (Atomizdat, Moscow, 1977; Wiley, New York, 1980).
17. S. G. Rautian, G. I. Smirnov, and A. M. Shalagin, *Nonlinear Resonances in Atomic and Molecular Spectra* (Nauka, Novosibirsk, 1979).
18. V. M. Zhdanov, *Transport Phenomena in Multicomponent Plasma* (Énergoizdat, Moscow, 1982).
19. A. I. Parkhomenko, Zh. Éksp. Teor. Fiz. **116**, 1587 (1999) [JETP **89**, 856 (1999)].

Translated by V. Sakun

JETP Letters, Vol. 74, No. 3, 2001, pp. 159–163. Translated from Pis'ma v Zhurnal Éksperimental'noĭ i Teoreticheskoĭ Fiziki, Vol. 74, No. 3, 2001, pp. 177–181.

Linear Nonreciprocal Dichroism in Boracite $Co_3B_7O_{13}I$

B. B. Krichevtsov

Ioffe Physicotechnical Institute, Russian Academy of Sciences, Politekhnicheskaya ul. 26, St. Petersburg, 194021 Russia

Received May 29, 2001

Linear nonreciprocal dichroism that is odd in magnetic field **B** was observed in the transverse geometry and studied for cubic (symmetry class T_d) phase of boracite $Co_3B_7O_{13}I$. Nonreciprocal dichroism was observed in the range of absorption bands corresponding to the transitions of the Co^{2+} ion in the energy range ΔE = 1.2–3.2 eV. The sign and magnitude of nonreciprocal dichroism depend on the mutual orientation of the magnetic field and crystallographic axes. Nonreciprocal dichroism refers to the phenomena of magnetically induced spatial dispersion, and its anisotropy is typical for the manifestation of the second-order magnetoelectric susceptibility in the optical range. © *2001 MAIK "Nauka/Interperiodica".*

PACS numbers: 75.80.+q; 78.20.Ls; 33.55.-b

1. It was shown in theoretical studies [1, 2] that the terms of the $\gamma_{ijkl}B_k k_l$ type in the expansion of the dielectric constant tensor $\epsilon_{ij}(\omega, \mathbf{k}, \mathbf{B})$ of noncentrosymmetric crystals are responsible for the linear nonreciprocal birefringence (NB) whose magnitude is proportional to the magnetic field **B**. The NB was experimentally studied in dielectrics and semiconductors [3–8]. It was recently observed in boracite single crystals $Co_3B_7O_{13}I$, $Cu_3B_7O_{13}Br$, and $Ni_3B_7O_{13}Br$, both in the transparent region [9, 10] and in the region of absorption bands [9]. These studies showed that the NB exhibits a pronounced resonant behavior near the strong absorption band due to the $Co^{2+}{}^4A_2(^4F) \longrightarrow {}^4E(^4P)$ transition in $Co_3B_7O_{13}I$ [9]. The NB anisotropy in different boracites is approximately the same and is described by the relationship $A \approx 2g$ between the parameters A and g of the γ_{ijkl} tensor [10]. Theoretical consideration showed that this relationship between the parameters is precisely that which is typical for the manifestation of the second-order magnetoelectric (ME) susceptibility G_{ijk} at optical frequencies in crystals of symmetry T_d [9]. This susceptibility relates the alternating magnetic moment $\delta\mathbf{M}^\omega$ (electric polarization $\delta\mathbf{P}^\omega$) to the electric $\mathbf{e}^\omega$ (magnetic $\mathbf{h}^\omega$) field of a light wave in crystal. Note that, generally, the NB can also be governed by the quadrupole mechanism, for which the relationship between the parameters A and g can be arbitrary.

Up to now, studies of the optical phenomena of magnetically induced spatial dispersion (MISD) in paramagnetic crystals were restricted to the NB and carried out by the laser polarimetric methods at certain wavelengths or in the frequency range corresponding to tunable lasers [6, 7, 9, 10]. This range proves to be insufficient if one intends to study the MISD phenomena in the range of certain optical transitions.

The purpose of this work was to develop methods for studying the energy dependences for the optical phenomenon associated with the manifestation of MISD in light absorption, namely, for the phenomenon of linear nonreciprocal dichroism (ND), and to study this phenomenon in the range of electronic transitions in boracite $Co_3B_7O_{13}I$.

Interest in these studies is due to the fact that the MISD phenomena can be caused by various mechanisms, e.g., by the manifestations of the second-order ME effect in the optical range and/or of the quadrupole mechanism. Certain conclusions about the contributions of these mechanisms to the local optical transitions can be drawn on the basis of the character of anisotropy of these phenomena. Note also that the manifestations of the ME effect and the quadrupole mechanism are due, respectively, to the interference of the electric dipole transition moment $\mathbf{d}_{ab}$ and the magnetic dipole $\mathbf{m}_{ab}$ (through the matrix elements of the type $\mathrm{Re}\,d^i_{ab}m^j_{ba}$) and the quadrupole Q^{jk}_{ab} ($\sim \mathrm{Im}\,d^i_{ab}Q^{jk}_{ba}$) moments, where a and b stand for the ground and excited state, respectively. By contrast, in the case of electric dipole transitions, the light absorption and the magnetooptic phenomena associated with the circular light polarization [Faraday effect or magnetic circular dichroism (MCD)] are determined by the electric dipole moment components of the $\mathrm{Re}\,d^i_{ab}d^j_{ba}$ and $\mathrm{Im}\,d^i_{ab}d^j_{ba}$ types [11, 12]. Therefore, the comparison of the absorption, MCD, and ND spectra can be used for estimating relative magnitudes of various moments (electric, magnetic, and quadrupole) for the individual optical transitions.

2. Experimental procedure and samples. The block diagram of a setup for measuring ND is shown in Fig. 1. The light from incandescent lamp *1* passed through monochromator *3* and polarizer *4* which polarized light at an angle of 45° to the vertical axis *Y* of the

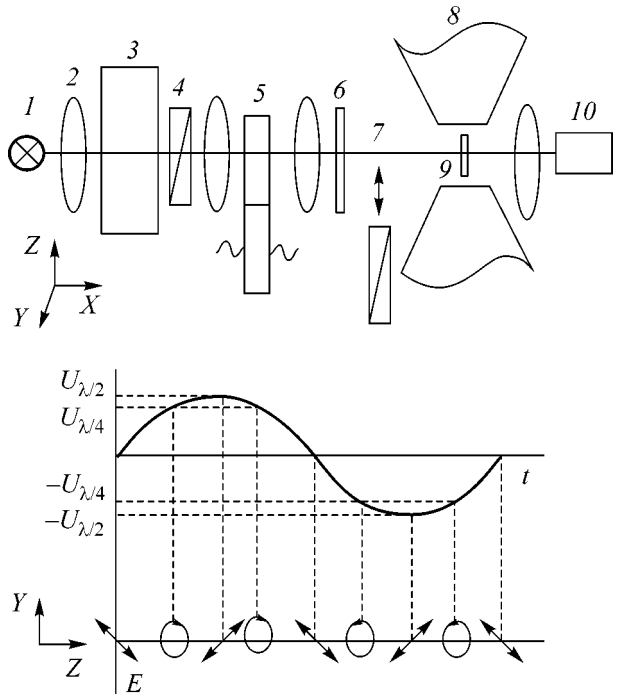

Fig. 1. Block scheme of a setup for measuring ND: (*1*) incandescent lamp (KGM-300); (*2*) lens; (*3*) monochromator (MDR-23); (*4*) polarizer; (*5*) elastooptical modulator; (*6*) compensator; (*7*) polarizer for calibration; (*8*) electromagnet; (*9*) sample; and (*10*) photodetector (FÉU-79). *XYZ* is the laboratory frame with the vertical *Y* axis. Variations in light polarization during one period of the modulating voltage are schematically shown below.

laboratory frame (E_{+45}), and then the polarization state was modulated by elastooptical modulator *5* with frequency Ω = 33 kHz. The time-varying light polarization is schematically shown in Fig. 1. The driving voltage of the modulator was chosen equal to the half-wave voltage $U_{\lambda/2}$, so that the light polarization changed four times from E_{+45} to E_{-45} during one period. Thus, if the difference $\Delta\alpha$ in the absorption coefficients of the $\mathbf{E}_{+45}$- and $\mathbf{E}_{-45}$-polarized lights was nonzero, this modulation was converted into the modulation of light intensity at the second harmonic 2Ω of the driving voltage. If crystal *9* displayed a circular dichroism, i.e., if the difference in the absorption coefficients of the clockwise and anticlockwise polarized lights was nonzero, it was converted into the modulation of light intensity at the first Ω and third 3Ω harmonics. This fact was used to attain maximal accuracy in orienting magnetic field **B**, created by electromagnet *8*, perpendicularly to the wave vector **k** so as to eliminate the undesirable effects associated with the possible manifestation of the MCD or Faraday effect. On the other hand, this made it possible to perform MCD measurements at small deviations (~2°) from the $\mathbf{B} \perp \mathbf{k}$ orientation.

For the second harmonic of driving voltage, the output voltage of photodetector *10* has the form $U_{2\Omega} = I_\circ SR\Delta\alpha d\exp(-\alpha d)$, where $I_\circ$ is the intensity of incident light; R is the reflectivity; α is the absorption coefficient; d is the crystal thickness; and S is the parameter allowing for the photodetector sensitivity, preamplifier gain, and reflection losses in the elements of an optical scheme. To eliminate the parameters $I_\circ$, R, S, and $\exp(-\alpha d)$, polarizer *7* crossed with polarizer *3* was included into the optical scheme ahead of the sample. The $\Delta\alpha d$ value was determined by the formula

$$\Delta\alpha d = T\frac{U_1^{2\Omega}}{U_2^{2\Omega}}, \qquad (1)$$

where T is the transmittance of polarizer *7*, $U_1^{2\Omega}$ is the second harmonic amplitude without polarizer *7*, and $U_2^{2\Omega}$ is the same with polarizer *7*. Polarizer *7* was also used in measuring the energy dependence of the absorption coefficient.

To eliminate spurious signals caused by the reflection from the elements of the scheme, compensator *6*; shaped like a thin (~100 μm) glass plate and forming angles ±45° with the *Z* axis was used it could rotate about the axes lying in the *ZY* plane. The use of the compensator allowed one to nullify $U_1^{2\Omega}$ in the absence of a magnetic field for any crystal azimuth and any light wavelength and to measure the $U_1^{2\Omega}(B)$ dependences within the amplifier sensitivity limits. To enhance sensitivity, a meander modulation with amplitude B_{max} = ±1 T and a period of 40 s was applied to the magnetic field. The response time of the selective amplifier was 3 s. The $U_1^{2\Omega}$ value was averaged over three modulation periods of the magnetic field. This allowed the sensitivity of ND measurements to be brought to $\Delta\alpha \approx 0.01$ cm^{-1}. The crystal could rotate in the magnet gap in the range from 0° to 360° with an accuracy of ~1°. Measurements were carried out over the energy range ΔE = 1.2–3.2 eV with a resolution of ~0.01 eV.

Single crystals of $Co_3B_7O_{13}I$ were cut as plates with an area of $\sim 2 \times 2$ mm^2 and a thickness d = 93 and 32 μm in the plane of the (110) type. The samples were oriented using X-ray radiography and by crystal faceting.

3. Experimental. In the range of absorption bands of $Co_3B_7O_{13}I$, the field dependence of $\Delta\alpha = \alpha(E_{-45}) - \alpha(E_{+45})$ is linear, with the magnitude and sign depending on the mutual orientation of magnetic field **B** and the crystallographic axes. Figure 2 shows the dependences of $\Delta\alpha/B$ on the angle θ between the magnetic field and the crystallographic direction of type [001] for different photon energies E. A change in θ by 180° results in changing the sign of $\Delta\alpha/B$, and the angular dependences of ND are described by a combination of the first-order ($\cos\theta$) and third-order ($\cos 3\theta$) harmon-

ics. Note that the anisotropy of $\Delta\alpha/B$ weakly depends on the photon energy in the energy range studied.

Figure 3 shows the energy dependence of $\Delta\alpha/B$ for $\theta = 60°$. For comparison, the absorption spectrum of $Co_3B_7O_{13}I$, similar to that obtained previously in [13, 14], is shown in the lower panel. The ND is observed in the absorption range and manifests itself as resonant bell-shaped bands. The ND magnitude is maximal near the $E = 2.1$ eV transition, where it equals $\Delta\alpha = 0.37$ cm^{-1} T^{-1}. In the energy range studied, the sign of $\Delta\alpha$ does not change at a fixed angle θ. The ratios of ND maxima near the bands at $E = 2.10$, 2.30, and 2.78 eV differ appreciably from those in the absorption spectrum. Contrary to the ND spectrum, in the MCD spectrum of $Co_3B_7O_{13}I$ these ratios are virtually the same as in the absorption spectrum.

4. Discussion. In the absorption range, the terms of the $\gamma_{ijkl}B_k k_l$ type can contribute to the anti-Hermitian symmetric part of the $\epsilon_{ij}(\omega, \mathbf{B}, \mathbf{k})$ tensor. In this range, the $\gamma_{ijkl} = \gamma'_{ijkl} + i\gamma''_{ijkl}$, where γ'_{ijkl} describes the nonreciprocal birefringence while γ''_{ijkl} describes the linear nonreciprocal dichroism. Since these tensors have identical transformation properties and are connected by the Kramers–Kronig relation, all conclusions of the phenomenological theory applied in [7] to the NB in crystals of symmetry T_d are also valid for the ND. In particular, the ND magnitude and anisotropy are determined by the independent parameters A'' and g'', which describe the contributions of the $\gamma''_{ijkl}B_k k_l$ terms, respectively, to the diagonal and nondiagonal components of ϵ''_{ij}. The principal directions in the ND rotate with a average angular velocity half as high as the rotation velocity of the magnetic field, and the NB and ND anisotropy in the plane of the (110) type is described by the first-order and third-order harmonics. The basic distinction between the NB and ND is that, at a given photon energy E, the NB is determined by the entire spectrum of optical transitions with energies higher than E, whereas the ND is due only to those transitions which contribute to the light absorption at the same energy. The NB anisotropy can, generally, differ from that of ND, excepting those cases where both phenomena are due to the same optical transition or where both are due to the manifestation of the second-order ME susceptibility and where the relationships $A' = 2g'$ and $A'' = 2g''$ hold true. It seems likely that both these cases apply to $Co_3B_7O_{13}I$. The ND anisotropy in the range of the $E = 2.1$ eV transition virtually coincides with the NB anisotropy obtained in [9] in the $E45B$ geometry. Note that this geometry was used in [9] to measure the difference in the refraction indices of lights polarized at angles $\pm 45°$ to the direction of the magnetic field. An analogous type of ND anisotropy is observed for other E values, e.g., near the $E = 2.3$ and 2.78 eV transitions (Fig. 2).

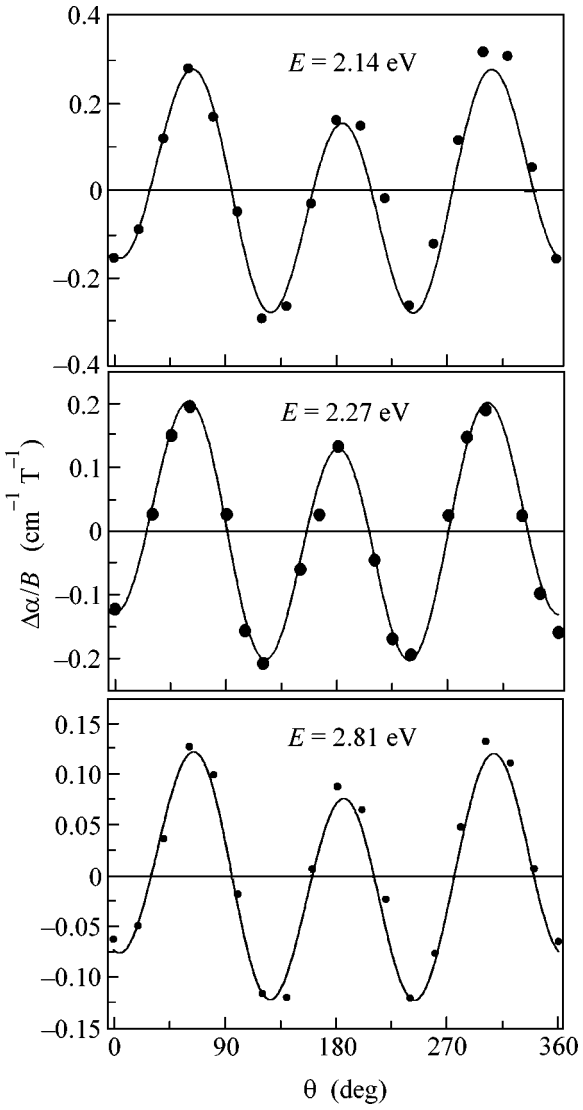

Fig. 2. Angular dependences of $\Delta\alpha/B$ in $Co_3B_7O_{13}I$ for different photon energies E. θ is the angle between the magnetic field and the crystallographic direction of the [001] type.

The NB and ND dispersions are different near the $E = 2.1$ eV transition. Whereas the NB is characterized by S-like dispersion, i.e., has different signs above and below the resonance energy [9], the ND is bell-shaped and can be described by Lorentzian curves. Assuming that the NB and ND are due only to the above-mentioned transition and that the difference in complex reflection indices can be written as

$$\Delta n^*_{\pm 45} = \Delta n' + i\Delta n'' = BD_{ab}\frac{E_{ab}^2 - E^2 + i\Gamma_{ab}E_{ab}}{(E_{ab}^2 - E^2)^2 - \Gamma_{ab}^2 E_{ab}^2}, \quad (2)$$

where E_{ab} is the resonance energy, Γ_{ab} is the damping parameter, and D_{ab} is the parameter depending on the

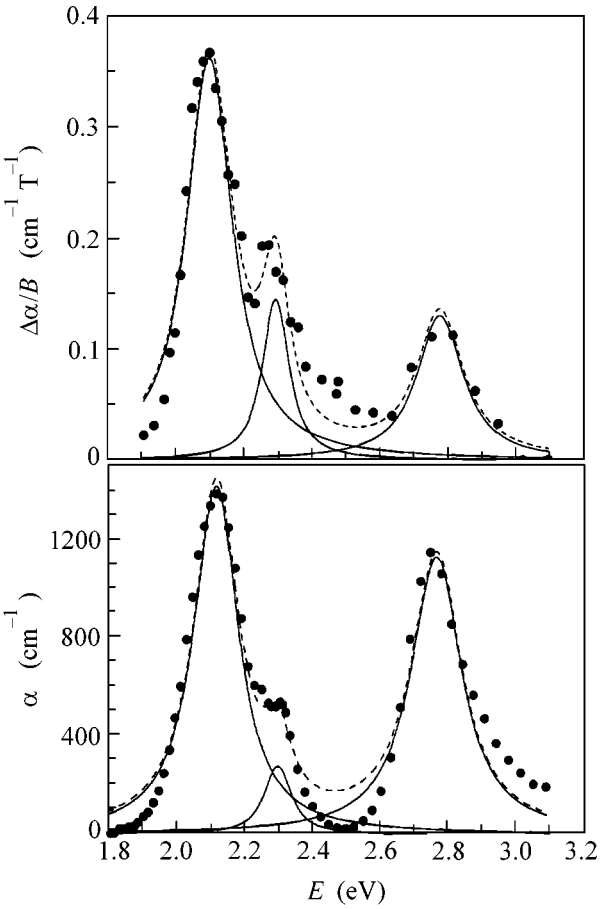

Fig. 3. Energy dependence of $\Delta\alpha/B$ for $\theta = 60°$. The absorption spectrum of $Co_3B_7O_{13}I$ is shown in the lower panel. Solid lines correspond to the contributions of individual Lorentzian curves.

transition matrix elements and temperature, one can compare the NB and ND magnitudes. Taking the ND magnitude equal to ~4 deg/(cm T) at $E = 2.05$ eV [9], one can readily arrive at a value of ~0.4 $cm^{-1} T^{-1}$ for the maximal ND magnitude at $E = 2.1$ eV, in agreement with the experimental value 0.37 $cm^{-1} T^{-1}$. The absorption coefficient at $E = 2.1$ eV is $\alpha \sim 1400$ cm^{-1} and the fractional ND magnitude in the field $B = 1$ T is $\Delta\alpha/\alpha \sim 2.6 \times 10^{-4}$.

In the energy range studied, the energy dependence of the absorption coefficient and the ND spectrum can be approximated by the sum of three Lorentzian curves. The resonance energies $E_1 = 2.10$ eV, $E_2 = 2.30$ eV, and $E_3 = 2.78$ eV and the damping parameters $\Gamma_1 = 0.16$ eV, $\Gamma_2 = 0.08$ eV, and $\Gamma_3 = 0.17$ eV are close in the absorption and ND spectra, while the ratios between the parameters D_i are noticeably different. The relative values D_i/D_1 ($i = 2, 3$) obtained from the absorption and ND spectra are given in the table. Whereas the parameters D_1 and D_3 for the $^4A_2(^4F) \longrightarrow {}^4E(^4P)$ transition at $E = 2.1$ eV and the $^4A_2(^4F) \longrightarrow {}^4A_2(^4P)$ transition at $E = 2.78$ eV are close in the absorption spectra, the parameter D_2 in the ND spectrum is smaller than D_1 by approximately a factor of four. At the same time, the ratio of parameter D_2 to parameter D_1 in the ND spectrum is approximately twice as large as in the absorption spectrum.

The D_2/D_i ratios derived from the absorption and ND spectra

	Absorption	ND
D_2/D_1	0.12	0.25
D_3/D_1	1.2	0.48

The fact that the ND anisotropy does not change upon the transition from one absorption band to the other and that it is characterized by the relationship $A'' \approx 2g''$ lends support to the conclusion that the ME mechanism is dominant in the MISD phenomena in boracites. In this case, the expression for the parameters A'' and g'' can be written as

$$A'' = 2g'' = S\sum_{a,\,b}\frac{\partial}{\partial B_x}[\rho_a Z''\mathrm{Re}(d^y_{ab}m^z_{ba} + \supset)], \quad (3)$$

where x, y, and z are the local axes of a paramagnetic ion, the z axis being aligned with the crystal axis $Z(S_4)$, while the x and y axes turned through an angle of f about the X and Y axes, respectively; ρ_a is the population of the ground level a, which is split into sublevels in a magnetic field; $Z'' = \Gamma_{ab}E/[E^2_{ab} - E^2)^2 + \Gamma^2_{ab}E^2]$; Γ_{ab} is the damping parameter; $\supset$ stands for the cyclic permutation of the x, y, and z indices; $S = 32\cos 2f(n^2 + 1)/3E\epsilon_\circ\Delta V$; n is the refraction index; and ΔV is the unit cell volume. The ND magnitude is determined by the matrix elements of the $\mathrm{Re}d^i_{ab}m^j_{ba}$ type, which are nonzero if the environment of paramagnetic ion is noncentrosymmetric. One can see from Eq. (3) that the bell-shaped (Lorentzian) ND dispersion can be obtained if the magnetic-field dependence is taken into account for the population $\rho_a(B)$ and for the transition matrix elements $\mathbf{d}_{ab}$ and $\mathbf{m}_{ab}$. The latter mechanism implies the mixing of different electronic states of the Co^{2+} ion in a magnetic field [12].

It is known that the absorption coefficient in the case of electric dipole transitions is determined by the matrix elements of the $\mathrm{Re}d^i_{ab}d^j_{ba}$ type, while the magnetic circular dichroism is described by the matrix elements of the $\mathrm{Im}d^i_{ab}d^j_{ba}$ type. A comparison of the absorption and MCD spectra of $Co_3B_7O_{13}I$ indicates that the electric dipole transition moments for $E = 2.1$ and 2.78 eV are close in magnitude. Moreover, the Re*dd*-to-Im*dd* ratios for the transitions at $E = 2.1$, 2.3, and 2.78 eV are approximately identical. By contrast, the ND spectrum gives evidence that the magnetic

dipole moments for these transitions can differ substantially from each other.

5. The main result of this work is that the linear nonreciprocal dichroism caused by the magnetically induced spatial dispersion was observed and studied in the range of absorption bands corresponding to the optical transitions of the paramagnetic ion in $Co_3B_7O_{13}I$. The method developed opens up new possibilities for studying the electronic 3*d* and 4*f* states of the ions in noncentrosymmetric crystals with the use of magnetoelectric spectroscopy.

I am grateful to N.F. Kartenko for X-ray structural studies, to A.Yu. Zyuzin for helpful discussions, and to A.I. Shelykh for assistance in measurements. This work was supported by the Russian Foundation for Basic Research (project no. 99-02-18028) and the program "Fundamental Spectroscopy."

REFERENCES

1. D. L. Portigal and E. Burstein, J. Phys. Chem. Solids **32**, 603 (1971).
2. V. M. Agranovich and V. L. Ginzburg, *Crystal Optics with Spatial Dispersion, and Excitons* (Nauka, Moscow, 1979; Springer-Verlag, New York, 1984).
3. V. A. Markelov, M. A. Novikov, and A. A. Turkin, Pis'ma Zh. Éksp. Teor. Fiz. **25**, 406 (1977) [JETP Lett. **25**, 378 (1977)].
4. O. V. Gogolin, V. A. Tsvetkov, and E. G. Tsitsishvili, Zh. Éksp. Teor. Fiz. **87**, 1038 (1984) [Sov. Phys. JETP **60**, 593 (1984)].
5. E. L. Ivchenko, V. P. Kochereshko, G. V. Mikhaĭlov, and I. N. Ural'tsev, Pis'ma Zh. Éksp. Teor. Fiz. **37**, 164 (1983) [JETP Lett. **37**, 164 (1983)]; Phys. Status Solidi B **121**, 221 (1984).
6. B. B. Krichevtsov, R. V. Pisarev, A. A. Rzhevsky, *et al.*, Phys. Rev. B **57**, 14611 (1998).
7. B. B. Krichevtsov, R. V. Pisarev, A. A. Rzhevskiĭ, *et al.*, Zh. Éksp. Teor. Fiz. **114**, 1018 (1998) [JETP **87**, 553 (1998)].
8. B. B. Krichevtsov, R. V. Pisarev, A. A. Rzhevskiĭ, and H.-J. Weber, Pis'ma Zh. Éksp. Teor. Fiz. **69**, 514 (1999) [JETP Lett. **69**, 551 (1999)].
9. B. B. Krichevtsov, A. A. Rzhevskii, and H.-J. Weber, Phys. Rev. B **61**, 10084 (2000).
10. B. B. Krichevtsov, Fiz. Tverd. Tela (St. Petersburg) **43**, 75 (2001) [Phys. Solid State **43**, 76 (2001)].
11. E. B. Graham and R. E. Raab, Proc. R. Soc. London, Ser. A **430**, 593 (1990).
12. A. K. Zvezdin and V. A. Kotov, *Modern Magnetooptics and Magnetooptical Materials* (Inst. of Physics Publ., Bristol, 1997).
13. R. V. Pisarev, V. V. Druzhinin, S. D. Prochorova, *et al.*, Phys. Status Solidi **35**, 145 (1969).
14. F. Smutný and Č. Koňák, Phys. Status Solidi A **31**, 151 (1975).

Translated by V. Sakun

JETP Letters, Vol. 74, No. 3, 2001, pp. 164–167. Translated from Pis'ma v Zhurnal Éksperimental'noĭ i Teoreticheskoĭ Fiziki, Vol. 74, No. 3, 2001, pp. 182–185.

Anisotropy of Magnetic Transport and Self-Organization of Corrugated Heterointerfaces in Selectively Doped Structures on GaAs(100) Substrates

A. A. Bykov*, A. K. Bakarov, A. V. Goran, A. V. Latyshev, and A. I. Toropov

Institute of Semiconductor Physics, Siberian Division, Russian Academy of Sciences, pr. Akademika Lavrent'eva 13, Novosibirsk, 630090 Russia

** e-mail: bykov@thermo.isp.nsc.ru*

Received June 28, 2001

The anisotropy of the longitudinal magnetoresistance has been found for a two-dimensional electron gas with a high mobility and concentration in GaAs quantum wells grown by molecular beam epitaxy on GaAs(100) substrates. The experimental data obtained are explained by the self-organization of spatially modulated heterointerfaces and are in agreement with the results of studying growth surfaces by atomic force microscopy. © *2001 MAIK "Nauka/Interperiodica".*

PACS numbers: 73.23.-b; 73.21.Fg

One of the physical reasons for the anisotropy of magnetic transport in a highly mobile two-dimensional electron gas (2DEG) in selectively doped structures is scattering from heteroboundary roughnesses. This mechanism is most pronounced in GaAs/AlGaAs heterojunctions grown by molecular beam epitaxy (MBE) on high-index GaAs substrate surfaces. As the concentration in these surfaces increases, the anisotropic scattering of charge carriers due to the morphology of heterointerfaces becomes dominant [1].

The scattering of 2DEG from heteroboundary roughnesses in conventional GaAs/AlGaAs heterojunctions grown on GaAs(100) substrates is insignificant compared to the scattering from the random potential of doping impurity. This fact is associated with the method that suppresses scattering from a random potential based on an increase in the distance between the conducting channel and the doping impurity. When this method is used, a high mobility of a 2DEG can be obtained only at a relatively low concentration of the order 3×10^{11} cm^{-2} and lower. For such concentrations, the effect of the morphology of heterointerfaces on 2DEG transport is small. At high concentrations, when scattering from roughnesses becomes significant, the scattering from a random potential also increases and remains dominating.

Recently, a new concept for the suppression of scattering from the random potential of a remote doping impurity has been proposed. Within this concept, both a high mobility and a high concentration of 2DEG can be obtained simultaneously [2]. In the proposed MBE structure, the 2DEG is located in a GaAs quantum well with AlAs/GaAs superlattice barriers. The *X* electrons arising in short-period AlAs/GaAs superlattice barriers smooth out the fluctuation potential of the doping impurity. As a result, the concentration of 2DEG in a GaAs quantum well with AlAs/GaAs superlattice barriers can be considerably increased without decreasing the mobility as compared to conventional GaAs/AlGaAs heterojunctions.

In this work, it is shown that the magnetoresistance of a 2DEG with high mobility and concentration exhibits an anisotropy due to the roughness of heterointerfaces in such MBE structures even when these structures are grown on GaAs(100) substrates. It is found that the reason for the anisotropy of magnetic transport in this case is the spatial modulation of heterointerfaces arising in the process of self-organization of growth surfaces [3].

The structures under study were grown on semiinsulating GaAs(100) substrates by the MBE technique. The active part of the structures represented a GaAs quantum well with a thickness of 10 nm. The quantum well was restricted on both sides by short-period superlattices composed of alternating AlAs and GaAs layers with a thickness of 1.1 and 2.3 nm, respectively. Two δ layers of Si with a concentration of 2.5×10^{12} cm^{-2} served as the sources of charge carriers. These layers were located in GaAs plates at a distance of 9 and 12.5 nm from the walls of the quantum well. The lower superlattice was separated from the substrate and the smoothing GaAs layer by an $Al_{0.3}Ga_{0.7}As$ layer with a thickness of 0.2 μm. The growth of GaAs was carried out under conditions characterized by the occurrence of As-stabilized surface (2×4) reconstruction, and the growth of $Al_{0.3}Ga_{0.7}As$ was characterized by (3×1) reconstruction.

0021-3640/01/7403-0164$21.00

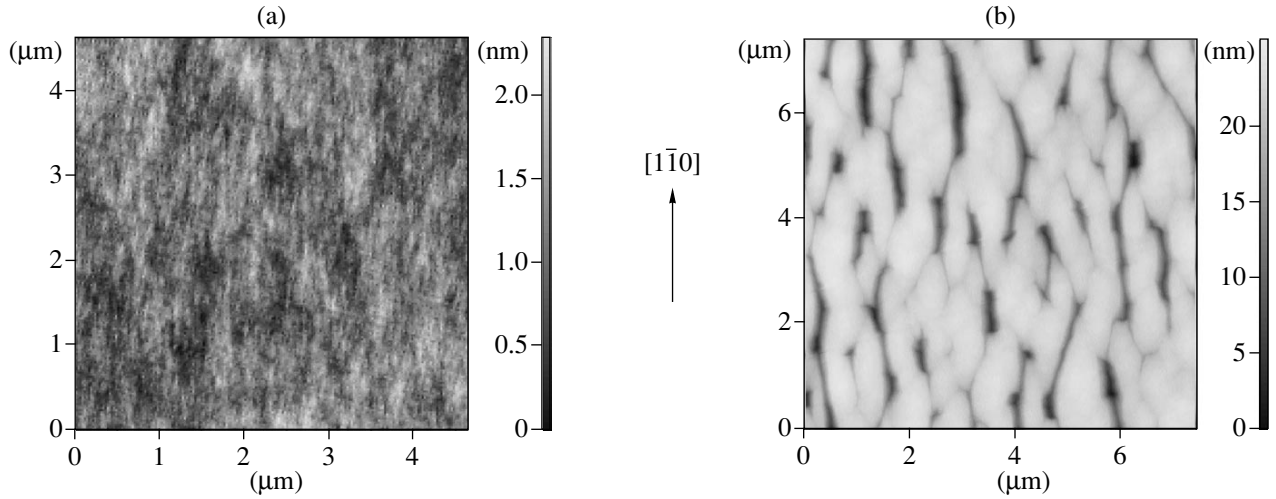

Fig. 1. AFM view of (a) "smooth" and (b) "corrugated" MBE structures.

The growth surfaces of MBE structures were analyzed by atomic force microscopy (AFM). An AFM view of an MBE structure is shown in Fig. 1a. The surface of this structure is characterized by the best smoothness that we managed to obtain. A typical view of an MBE structure with the corrugated surface is shown in Fig. 1b. The undulate character of the surface is manifested well. The ridges are predominantly oriented along the $[1\bar{1}0]$ direction. Figure 2 displays AFM profiles for "smooth" and "corrugated" surfaces in the [110] and $[1\bar{1}0]$ directions. These profiles demonstrate that spatial modulation is small in the first case and hardly distinguishable in the second case. Its period depends on the direction.

Based on the grown structures, Hall-effect bridges oriented along the $[1\bar{1}0]$ and [110] directions with a length of 100 μm and a width of 50 μm were manufactured by optical lithography and liquid etching. Magnetic transport measurements were performed at T = 4.2 K in magnetic fields of up to 2 T that were parallel and perpendicular to the substrate. The transport properties of the 2DEG in quantum wells were studied for various averaged heights h of the spatial modulation of heterointerfaces. Its value was varied from 0.5 to 15 nm, depending on the growth conditions. The lateral period of spatial modulation d in the MBE structures under study was 0.5–1.5 μm in the [110] direction. The 2DEG concentration in the initial structures was within the range $(1.1–1.8) \times 10^{12}$ cm^{-2}, and the mobility was $(1–5) \times 10^5$ cm^2 V^{-1} s^{-1}, depending on the orientation of the measuring current and on the d and h values.

The magnetic field dependence of the longitudinal resistance R_{xx} along the $[1\bar{1}0]$ and [110] directions in a magnetic field B perpendicular to the substrate is displayed in Fig. 3. It is evident that the values of R_{xx} in a zero magnetic field for a sweeping current oriented along various directions are different for both "smooth" and spatially modulated MBE structures. The anisotropy of conductivity increased with the increasing height of the spatial modulations of growth surfaces. However, we did not manage to obtain an anisotropy

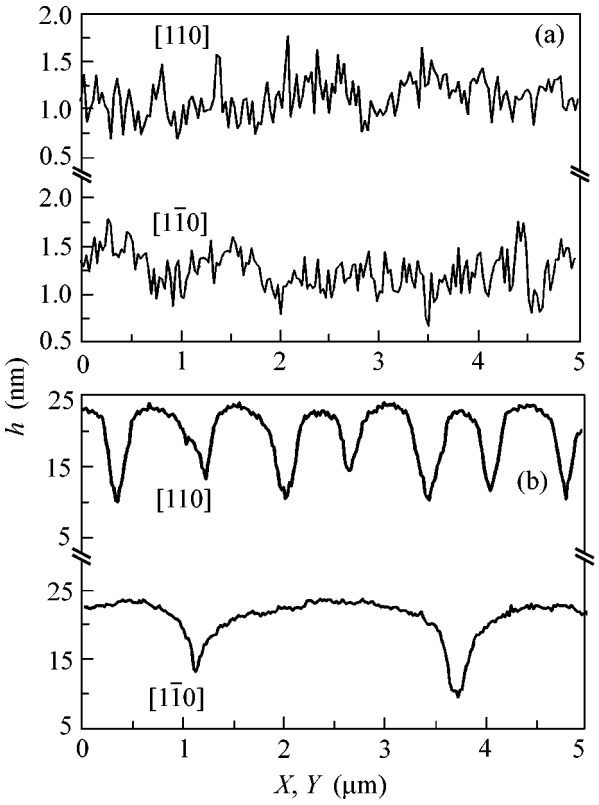

Fig. 2. AFM profiles in the [110] and $[1\bar{1}0]$ directions for (a) "smooth" and (b) "corrugated" MBE structures.

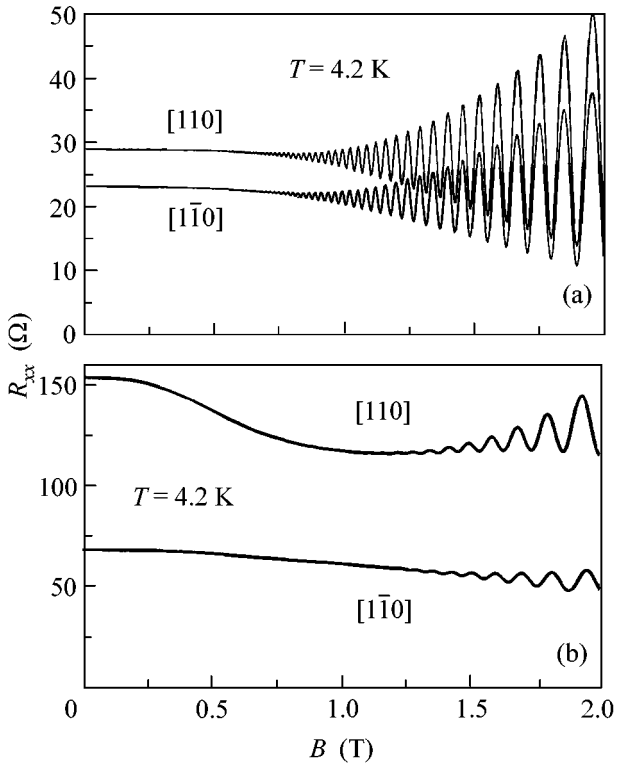

Fig. 3. Longitudinal resistance of a 2DEG in orthogonal directions in a perpendicular magnetic field for (a) "smooth" and (b) "corrugated" MBE structures.

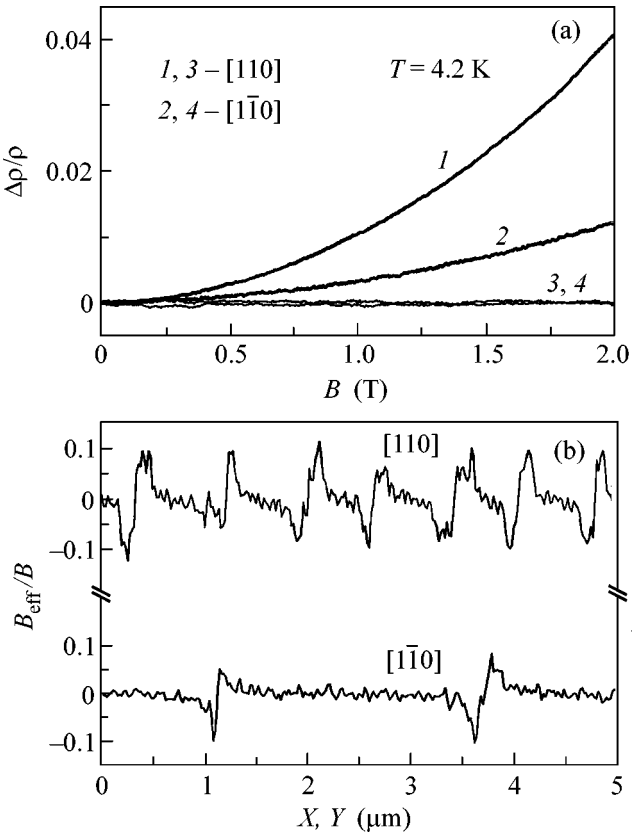

Fig. 4. (a) Longitudinal resistance of a 2DEG in orthogonal directions in a parallel magnetic field for (*1*, *2*) "corrugated" and (*3*, *4*) "smooth" MBE structures; (b) profiles of the effective magnetic field in orthogonal directions for the 2DEG in a "corrugated" MBE structure.

less than that shown in Fig. 3a for a conventionally "smooth" MBE structure. A typical negative magnetoresistance (MR) is observed for the MBE structure with the highest MR anisotropy in magnetic fields from 0 to 1 T ([110] direction, Fig. 3b). A negative MR was observed previously in MBE structures grown on high-index GaAs substrates [1] and on GaAs substrates with a relief formed in advance [4, 5].

The magnetic field dependence of R_{xx} in a magnetic field B parallel to the substrate and to the direction of the measuring current is shown in Fig. 4a. It is evident in the figure that the MR of an MBE structure with "smooth" heterointerfaces remains constant within experimental accuracy over the entire range of magnetic fields. However, an anisotropic positive MR is observed in a "corrugated" structure. The value of this MR depended on the spatial modulation of heterointerfaces: the larger the value of h, the greater the MR, all other things being equal.

The well pronounced anisotropy of the longitudinal resistance R_{xx} in a perpendicular magnetic field allows the conclusion that the MBE structures under study are characterized by the mechanism of scattering from roughnesses of heterointerfaces. The reason for the manifestation of this mechanism is associated with the fact that the surface of heterointerfaces of GaAs quantum wells forms as steps. Similar structures form in heterojunctions grown on high-index GaAs substrates [1]. This conclusion is in agreement with AFM profiles. It is evident that the scattering from steps will be lower in the direction in which the spatial modulation of heterointerfaces is virtually absent, because it proceeds predominantly when charge carriers "overcome ridges," that is, when the carriers move perpendicular to the steps.

The spatial modulation of heterointerfaces of GaAs quantum wells (in accordance with AFM profiles) means that the motion of charge carriers along such boundaries proceeds under periodically varying conditions. We believe that the geometrical parameters of steps and facets that form the corrugated surface also vary periodically in accordance with the spatial modulation of heterointerfaces. Such a simplified consideration allows the conclusion that the "large" negative MR in the MBE structures in hand is of a classical nature and is associated with the commensurable motion of charge carriers in the periodic lattice of scatterers [6]. Within this suggestion, the scatterers are steps and facets rather than antidots, as distinct from [6]. The absence of commensurable maxima in the magnetic field dependences in this case is due to the larger dispersion of the period of scatterers [7].

The direct evidence of the spatial modulation of the 2DEG in the samples under study is provided by the fact that a positive MR is observed in an external uniform magnetic field B parallel to the substrate [4, 8, 9]. In this case, charge carriers move in the effective nonuniform magnetic field B_{eff} either along the lines of the constant magnetic field $B_{\text{eff}} = B_{\text{const}}$ or by overcoming magnetic barriers [10, 11]. The profiles of B_{eff} calculated from AFM profiles for two mutually perpendicular directions of the parallel field B are presented in Fig. 4b. It is evident in the figure that the periods of the spatial modulation of B_{eff} and, correspondingly, that the number of magnetic barriers for B directed perpendicular and parallel to the ridges of "waves" differ by a factor of approximately five. This is the reason for the anisotropy of the positive MR.

Thus, it is shown experimentally that the 2DEG in GaAs wells with self-organized corrugated heterointerfaces is spatially modulated. Its magnetic transport properties in a perpendicular magnetic field are due to the motion of charge carriers in the anisotropic disordered lattice of scatterers, and those in a parallel magnetic field are due to the motion of charge carriers in the effective magnetic field whose spatial modulation may reach 20% of the external uniform parallel magnetic field.

The authors are grateful to G.M. Gusev for fruitful discussions of the results of this work.

This work was supported by the Russian Foundation for Basic Research, project nos. 01-02-16892 and 00-02-17896, and by the program "Physics of Solid-State Nanostructures" of the Ministry of Science of the Russian Federation, project no. 99-1132.

REFERENCES

1. A. C. Churchill, G. H. Kim, A. Kurobe, *et al.*, J. Phys.: Condens. Matter **6**, 6131 (1994).
2. K.-J. Friedland, R. Hey, H. Kostial, *et al.*, Phys. Rev. Lett. **77**, 4616 (1996).
3. A. Ballestad, B. J. Ruck, M. Adamcyk, *et al.*, Phys. Rev. Lett. **86**, 2377 (2001).
4. G. M. Gusev, J. R. Leite, A. A. Bykov, *et al.*, Phys. Rev. B **59**, 5711 (1999).
5. A. A. Bykov, G. M. Gusev, J. R. Leite, *et al.*, Phys. Rev. B **61**, 5505 (2000).
6. K. Ensslin and P. Petroff, Phys. Rev. B **41**, 12307 (1990).
7. G. M. Gusev, Z. D. Kvon, L. V. Litvin, *et al.*, Pis'ma Zh. Éksp. Teor. Fiz. **56**, 173 (1992) [JETP Lett. **56**, 170 (1992)].
8. M. L. Leadbeater, C. L. Foden, J. H. Burroughes, *et al.*, Phys. Rev. B **52**, R8629 (1995).
9. A. A. Bykov, G. M. Gusev, J. R. Leite, *et al.*, Physica B (Amsterdam) **298**, 79 (2001).
10. J. E. Muller, Phys. Rev. Lett. **68**, 385 (1992).
11. I. S. Ibrahim, V. A. Schweigert, and F. M. Peeters, Phys. Rev. B **56**, 7508 (1997).

Translated by A. Bagatur'yants

JETP Letters, Vol. 74, No. 3, 2001, pp. 168–172. Translated from Pis'ma v Zhurnal Éksperimental'noĭ i Teoreticheskoĭ Fiziki, Vol. 74, No. 3, 2001, pp. 186–190.

Dynamic Mixed State in Micron-size Bridges Based on $Bi_2Sr_2CaCu_2O_x$ Whiskers

S. G. Zybtsev, I. G. Gorlova*, and V. Ya. Pokrovskiĭ

Institute of Radio Engineering and Electronics, Russian Academy of Sciences, Moscow, 103907 Russia

** e-mail: gorl@mail.cplire.ru*

Received June 29, 2001

Measurements of the current–voltage characteristics of micron-size bridges made of $Bi_2Sr_2CaCu_2O_x$ single-crystal whiskers are carried out. It is found that, at temperatures below the superconducting transition temperature, the current–voltage characteristics exhibit quasi-periodic voltage jumps with segments of constant differential resistance whose value is proportional to the jump number. For the narrowest bridges (0.5–1 μm), up to ten voltage jumps are observed. The result of the experiment is explained by the formation of vortex lines under the current effect. © *2001 MAIK "Nauka/Interperiodica".*

PACS numbers: 74.25.Fy; 74.72.Hs

In superconductors, the process of superconductivity destruction under the effect of electric current is characterized by a spatial inhomogeneity and can be accompanied by interesting effects such as the formation of vortex lines [1, 2], hot spots [3–5], and phase-slip centers [6]. The dynamic mixed state that occurs in these cases (in the absence of a magnetic field) manifests itself in the current–voltage characteristics as quasi-periodic (in current) voltage jumps with segments of constant differential resistance. The effect was observed for superconducting bridges made from low-T_c superconductors [2, 3, 6]. The study of these bridges made it possible to determine the characteristic relaxation times, the viscosity coefficient, the velocity of the vortex motion, the pinning force, and other parameters. However, in homogeneous samples of high-T_c superconductors, multistep current–voltage characteristics have never been observed in the plane of superconducting layers.

This paper describes the study of the superconductivity destruction by current in BSCCO (2212) single-crystal whiskers and bridges made on their basis with the dimensions of about the effective magnetic penetration depth $\lambda_\perp$. The experimental curves showed a set of regular voltage jumps with varying current.

The BSCCO (2212) whiskers grown by the method described in [7] had the form of homogeneous, almost defect-free, single crystals [8], which is a necessary condition for the formation of vortex lines [1]. To obtain the maximal current density, bridge structures were prepared on the basis of these whiskers. The length l and width w of the bridges were both approximately equal to 0.5–5 μm, and their thickness d was 0.1–0.3 μm. In [1], it was shown that, in the case $\xi \ll d \ll l \ll w \ll \lambda_\perp$, where ξ is the coherence length and $\lambda_\perp = \lambda^2/d$ (λ is the magnetic penetration depth), a coherent single-line vortex motion is possible. For BSCCO, $\lambda \approx 0.3$ μm, and for our samples we obtain $\lambda_\perp \sim 1$ μm; i.e., $\xi \ll d \ll l \sim w \leq \lambda_\perp$. Hence, we deal with the boundary region and can expect the formation of vortex lines, in qualitative accordance with [1].

The bridges were fabricated by microetching using a pulsed (10 ns) focused scanning laser beam with a wavelength of 0.53 μm. The technique used for mounting the crystals on a substrate and making gold contacts by laser spraying of gold in vacuum is described in [7]. Figure 1a shows the arrangement of contacts on a wide whisker, and Fig. 1b shows a short micron-size bridge formed by etching in a part of the wide whisker. One side of the bridge is a natural face of the whisker.

To measure the current–voltage characteristics $V(I)$ and the temperature dependence of the resistance $R(T)$, we used the five-probe method. The measurements were simultaneously performed for two parts of the single crystal: one part with the bridge and the other without it. As a rule, the dependences $R(T)/R(300\ \mathrm{K})$ obtained for the bridge and for the crystal part without the bridge coincided, which testified to the unperturbing effect of the laser microetching. We also studied the destruction of the superconducting state in long narrow (~ 1 μm) whiskers, one of which is shown in Fig. 1c. Figure 1d presents the temperature dependences of the resistance for four samples: two bridges 0.5 and 3 μm wide and two whiskers 1.5 and 10 μm wide. One can see that the curves are almost coincident. The samples have a small residual resistance [which was obtained by the linear extrapolation of $R(T)$ observed for $T > 100$ K to $T = 0$ and reached ~ 10% of $R(300\ \mathrm{K})$] and represent single-phase crystals (T_c determined by the end of the transition, $R = 0$, was equal to 73–76 K). The transition width is 3–5 K, and the resistivity at room temperature

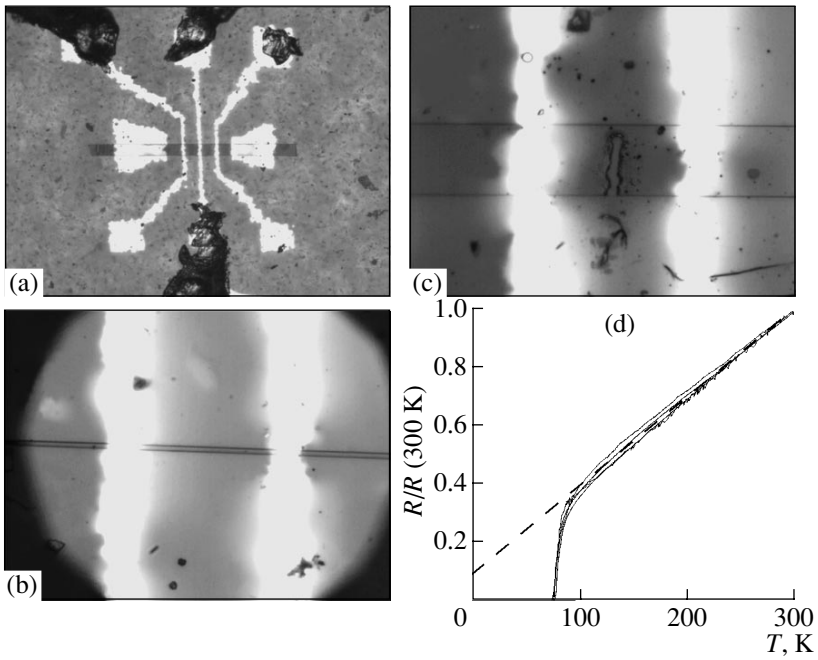

Fig. 1. (a) Five-probe measuring structure; (b) part of a whisker with a bridge; (c) 1-μm-wide whisker. The distance between the adjacent probes is 30 μm in all micrographs. (d) Temperature dependences of the resistance for a 10-μm-wide whisker, a 3-μm-wide bridge, a 0.5-μm-wide bridge, and a 1.5-μm-wide whisker. The dashed line shows the extrapolation of $R_n(T)$ to $T = 0$; $\rho(300\ \mathrm{K}) \approx 300\ \mu\Omega$ cm.

is $\rho(300\ \mathrm{K}) \approx 300\ \mu\Omega$ cm. All this testifies to the high quality of the crystals and bridges under consideration.

The measurements below T_c show that, for bridges whose width is $w < 4$ μm, voltage jumps appear in the current–voltage characteristics as the temperature decreases. For smaller w, the jumps are more regular and their number is greater. At $w = 0.5$ μm, the current–voltage characteristics exhibit up to ten voltage jumps.

Figure 2 shows the current–voltage characteristics of one of the bridges (with $T_c = 73.5$ K) at different temperatures. When $T \geq T_c$, the current–voltage characteristic follows the same power law $V \propto I^{\alpha}$ as was observed earlier for wide samples [9, 10]: at $T > T_c$, the exponent is $\alpha = 1$, and at $T = T_c$ (curve *6*), it increases to $\alpha = 3$. However, as the temperature decreases below T_c, periodic bends appear in the curves, and at $T = 63.4$ K (curve *9*), the current–voltage characteristic exhibits about ten pronounced voltage jumps (see the inset in Fig. 2). We note that the current–voltage characteristics do not depend on the direction of the current sweep, i.e., no current hysteresis is observed.

Figure 3 presents curve *9* from Fig. 2 on a linear scale. In the region $I > 1.5$ mA, the current–voltage characteristic exhibits voltage jumps that are quasi-periodic in current and are separated by segments with a constant differential resistance R_d. From Fig. 3, one can see that the extrapolation of the linear portions of the current–voltage characteristic to $V = 0$ yields approximately the same current $I_p = 1.2$ mA.

Figure 4 shows the dependence of R_d on N, where N is the order number of the linear portion of the current–voltage characteristic. The dependence $R_d(N)$ is almost linear; i.e., as N increases by unity, R_d increases by a constant value R_{d0}: $R_{dN} = R_{d0}N$, where R_{dN} is the

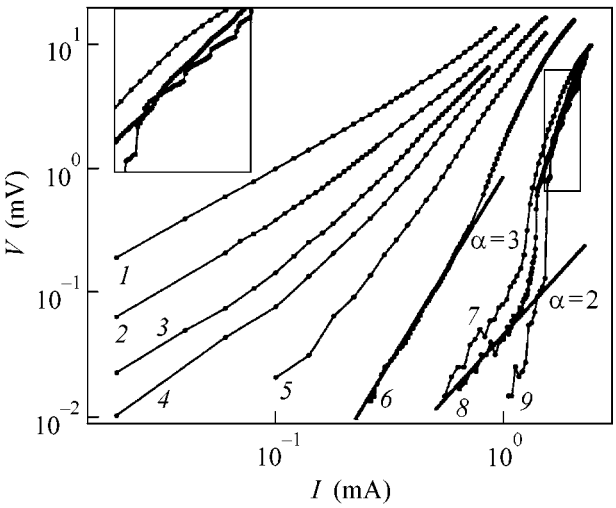

Fig. 2. Current–voltage characteristic of a bridge with dimensions $d = 0.22$ μm, $w = 0.5$ μm, and $l = 1$ μm ($T_c = 73.5$ K) at the temperatures: (*1*) 77.4, (*2*) 76.5, (*3*) 76.2, (*4*) 76.0, (*5*) 74.8, (*6*) 73.5, (*7*) 71.0, (*8*) 68.8, and (*9*) 63.4 K. The inset shows the part of the plot enclosed in the rectangle on an enlarged scale.

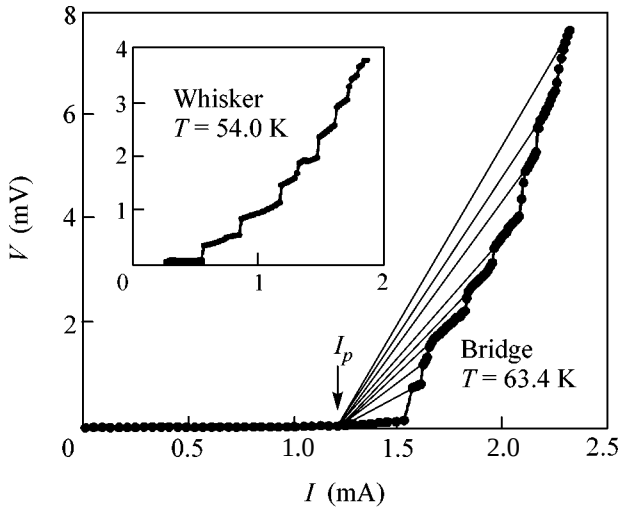

Fig. 3. Current–voltage characteristic of a bridge with dimensions $1 \times 0.5 \times 0.22$ μm (curve *9* in Fig. 2). The inset shows the current–voltage characteristic of a whisker with dimensions $30 \times 1 \times 0.13$ μm (T = 54 K). In both cases, one can see a regular stepped structure.

differential resistance of the Nth segment. A similar dependence is presented for the total resistance $R = V/I$.

Before analyzing the experimental results, we note that, in appearance, the dependence shown in Fig. 3 is similar to the current–voltage characteristics of long narrow bridges made from low-T_c superconductors with the transverse dimensions smaller than ξ. In this case, the stepped form of the current–voltage characteristics is explained by the formation of the phase-slip centers [6]. However, the width and thickness of our bridges considerably exceed the coherence length (for BSCCO, ξ ~ 50–100 Å). In [11], the voltage jumps observed for wide granular YBCO films were explained by the fact that the bridges were highly inhomogeneous and the condition of the phase-slip center formation could be satisfied in some of their parts. In our case, the bridge is made of a 2212 BSCCO single crystal. The form of $R(T)$ and the high critical currents of the bridges (>10^5 A/cm^2),which are as high as in perfect single crystals [7], testify to the homogeneity of our bridges. Thus, the steps observed by us in the current–voltage characteristics cannot be explained by the formation of phase-slip centers.

For wide films ($w, l > \lambda$), the resistive state is determined by the nucleation of rows of vortices at the edge. The current–voltage characteristics of such films are determined by a viscous vortex motion [12]. Under sufficiently strong currents, the formation of a flux-flow instability accompanied by thermal effects is possible, which results in the appearance of one or several voltage jumps in the current–voltage characteristic [3, 5, 12]. In this case, each jump corresponds to the formation of a resistive region (domain) with the dimensions of approximately the thermal length (for YBCO, this value is ~ 1 μm [5]). Our bridge can contain no more than one such domain. Besides, a local superheating is always accompanied by a hysteresis in the current–voltage characteristic. For our microbridges, this explanation also fails, because we observed multistep current–voltage characteristics without any hysteresis.

Several jumps in the current–voltage characteristic can appear in the case of an inhomogeneous distribution of the pinning force in the film [12], and, in principle, such an inhomogeneity can be introduced by laser radiation. However, this assumption is inconsistent with the observation of voltage jumps in the current–voltage characteristic of a narrow ($w \approx 1$ μm) homogeneous whisker (see the inset in Fig. 3).

As noted above, we have $d, w, l \leq \lambda_\perp$ for our microbridge, and, according to [1], the dynamic resistive state can be determined by the vortex motion in one or several lines [2]. The distinctive feature of this kind of resistive state is the quadratic dependence $V \propto I^2$ in the initial part of the current–voltage characteristic, when the line begins to be filled with vortices [1]. Such a dependence is observed in the experiment: as the temperature decreases, the exponent, after an increase to three in the small current region, decreases to two (curve *8* in Fig. 2). This is accompanied by the appearance of bends in the current–voltage characteristic, which precede the appearance of steps (the inset in Fig. 2).

As the current increases, the formation of the second and subsequent lines of vortices becomes possible. This must lead to periodic changes in the differential resistance R_d, which were observed earlier on tin bridges [2]. In our case, as seen from Figs. 3 and 4, the current–voltage characteristics exhibit an increase in the differential resistance R_d with current with periodic steps of equal height $R_{d0} \approx 0.68\ \Omega$. These steps can be caused by the appearance of identical lines of vortices, so that each jump in R_d corresponds to the formation of a new vortex line.

From Fig. 3, one can see that the linear portions of the current–voltage characteristic are extrapolated to the same current value $I = I_p$ corresponding to $V = 0$. With allowance made for the pinning, the equation describing the viscous vortex motion takes the form

$$u = \eta^{-1}\phi_0(j - j_p), \qquad (1)$$

where u is the velocity of vortices, η is the viscosity coefficient, ϕ_0 is the magnetic flux quantum, and j_p is the current density at which the vortices begin to separate from the pinning centers (see, e.g., [12]). If we assume that, in our case, we have $j_p \approx I_p/S$, where S is the cross-sectional area of the bridge, then, because $V \propto u$, condition (1) means that $V \propto (I - I_p)$, which corresponds to the linear portions of the current–voltage characteristic (Fig. 3). From Eq. (1), using the fact that the mean velocity of vortices in the lines is $u = V\xi/N\phi_0$ (on the assumption that the distance between vortices in

a line is about ξ and the voltage drop at each line is V/N) and that $\xi(65\ \text{K}) \approx 100$ Å, we obtain the viscosity coefficient for BSCCO: $\eta = \phi_0^2 N(j - j_p)/V\xi = \phi_0^2/R_{d0}\xi S = 6 \times 10^{-9}$ H s/m^2. It should be noted that the estimate of η for YBCO single crystals near T_c, which can be obtained from the observation [13] of the vortex lattice motion in a spatially inhomogeneous potential of the pinning centers, yields a value that is an order of magnitude greater: $\eta(89\ \text{K}, 1.7\ \text{T}) = 6.3 \times 10^{-8}$ H s/m^2. For low-temperature superconductors, the viscosity is still greater: for, e.g., $NbSe_2$, $\eta(3.2\ \text{K}) = 1.4 \times 10^{-7}$ H s/m^2 [14]. Nevertheless, the value of η obtained from our experiment seems to be reasonable, because the estimate of the normal resistivity ρ_n by the Bardeen–Stefan formula $\eta = H_{c2}\phi_0/\rho_n$ [15], where $H_{c2} = \phi_0/2\pi\xi^2$ is the upper critical field, yields the value $\rho_n(65\ \text{K}) \approx 100\ \mu\Omega$ cm, which is fairly close to the value obtained by the linear extrapolation of $R(T)$ (the dashed line in Fig. 1d).

When the bridge is filled with vortex lines, their maximal number should be equal to $N_{\max} = 0.4l/\xi$ [2]. In this case, the resistance of the bridge should be close to the normal-state resistance R_n. Therefore, $N_{\max}$ can be estimated as R_n/R_0, where R_0 is the contribution of each line to the bridge resistance. From Fig. 4, one can see that the curve $R(N)$ is close to a straight line, and from its slope we determine $R_0 \sim 0.3\ \Omega$. Knowing the length of the bridge $l \approx 1$ μm and the resistance $R_n \approx 10\ \Omega$ at a given temperature, we obtain $\xi = 0.4l/N_{\max} = 0.4lR_0/R_n \approx 100$ Å, which agrees well with the value of $\xi(65\ \text{K})$ for BSCCO. An equally good agreement of the estimates was obtained for all samples studied in our experiment.

Knowing the value of the resistance step R_0, one could expect that the normal state would be reached as a result of approximately 40 resistance jumps. However, our experiment showed that, approximately after the tenth step, the resistance exhibits a sharp increase, which can be related to the nonmonotonic dependence $\eta(u)$ [16]. If the vortex velocity exceeds a characteristic value u^*, the viscosity begins to decrease and the current–voltage characteristic breaks. Estimating $u^* = V^*\xi/N\phi_0$ ($N = 9$, Fig. 3), where V^* is the voltage corresponding to the break of the characteristic, we obtain $u^* \approx 5 \times 10^5$ cm/s, which corresponds to the value of u^* in BSCCO films [17].

Thus, the whole set of data suggests that the appearance of regular steps in the current–voltage characteristics of BSCCO microbridges of width $w \le \lambda$ is associated with the sequential formation of individual vortex lines under the effect of current. It should be noted that the periodic increase in R_d by the value R_{d0} corresponding to the formation of a single line was never observed before. The study of multistep current–voltage characteristics of high-T_c microbridges offers new possibilities for investigating the motion of vortices in lines and their interaction.

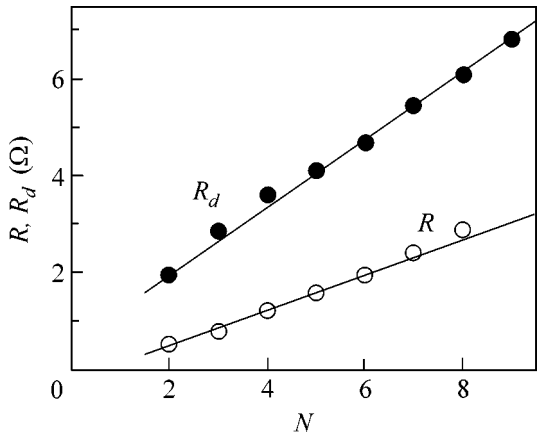

Fig. 4. Dependences of the differential resistance R_d (determined from the slope of the linear portions of the current–voltage characteristics) and the total resistance R (determined from the beginning of the voltage jumps) on the step number. The first step is assumed to be doubled.

In closing, we note two more facts. As seen from Fig. 3, the current–voltage characteristic of a long (30 μm) whisker has a stepped structure similar to that observed in the current–voltage characteristics of short bridges of the same width. This means that, for the formation of vortex lines, the bridge must not necessarily be short (see [1]): the fundamental requirement is that the bridge width is $\sim\lambda_\perp$. In addition, we can conclude that a long-range interaction occurs between the vortex lines: the first line suppresses the formation of others, and only when the current increases by a certain value, does the appearance of the second, third, and following lines become possible.

As seen from Fig. 2, the nucleation of lines of three-dimensional vortices in quasi-two-dimensional high-T_c superconductors can lead to a deviation of the current–voltage characteristic from the power law typical of the Berezinski–Kosterlitz–Thouless transition, which is observed in BSCCO single crystals [9] and, specifically, in whiskers [10]. Presumably, the nucleation of three-dimensional vortex lines is responsible for the wavy form of the current–voltage characteristics, which is almost always observed in layered high-T_c superconductors (see, e.g., [18]).

We are grateful to A.M. Nikitina for synthesizing the samples, to V.N. Timofeev for studying the bridge structures using an electron microscope, and to S.N. Artemenko and V.N. Gubankov for discussing the results.

This work was supported by the Federal program "Topical Problems of the Physics of Condensed State" (the subprogram "Superconductivity," project no. 98049) and the Russian Foundation for Basic Research (project nos. 00-02-22000 NTsNI and 99-02-17387).

REFERENCES

1. K. K. Likharev, Zh. Éksp. Teor. Fiz. **61**, 1700 (1971) [Sov. Phys. JETP **34**, 906 (1971)].
2. V. N. Gubankov, V. P. Koshelets, K. K. Likharev, and G. A. Ovsyannikov, Pis'ma Zh. Éksp. Teor. Fiz. **18**, 292 (1973) [JETP Lett. **18**, 171 (1973)].
3. Yu. M. Ivanchenko, P. N. Mikheenko, and V. F. Khirnyĭ, Zh. Éksp. Teor. Fiz. **80**, 171 (1981) [Sov. Phys. JETP **53**, 86 (1981)].
4. R. N. Sheftal, S. G. Zybtsev, and Sn. M. Babadjanian, in *Progress in High Temperature Superconductivity* (World Sci., Singapore, 1991), Vol. 32, p. 236.
5. Z. L. Xiao, E. Y. Andrei, and P. Ziemann, Phys. Rev. B **58**, 11185 (1998).
6. J. D. Meyer and G. V. Minnigerode, Phys. Lett. A **38A**, 529 (1972).
7. Yu. I. Latyshev, I. G. Gorlova, A. M. Nikitina, *et al.*, Physica C (Amsterdam) **216**, 471 (1993).
8. I. G. Gorlova and V. N. Timofeev, Physica C (Amsterdam) **255**, 131 (1995).
9. S. N. Artemenko, I. G. Gorlova, and Yu. I. Latyshev, Pis'ma Zh. Éksp. Teor. Fiz. **49**, 566 (1989) [JETP Lett. **49**, 654 (1989)].
10. I. G. Gorlova, S. G. Zybtsev, A. M. Nikitina, *et al.*, Pis'ma Zh. Éksp. Teor. Fiz. **68**, 205 (1998) [JETP Lett. **68**, 216 (1998)].
11. R. B. Akoryan and S. G. Gevorgyan, Pis'ma Zh. Éksp. Teor. Fiz. **52**, 1255 (1990) [JETP Lett. **52**, 674 (1990)].
12. L. G. Aslamazov and S. V. Lempitskiĭ, Zh. Éksp. Teor. Fiz. **84**, 2216 (1983) [Sov. Phys. JETP **57**, 1291 (1983)].
13. J. M. Harris, N. P. Ong, R. Garnon, *et al.*, Phys. Rev. Lett. **74**, 3684 (1995).
14. Y. Matsuda, N. P. Ong, Y. F. Yan, *et al.*, Phys. Rev. B **49**, 4380 (1994).
15. J. Bardeen and M. J. Stephen, Phys. Rev. **140**, 1197 (1965).
16. A. I. Larkin and Yu. N. Ovchinnikov, Zh. Éksp. Teor. Fiz. **68**, 1915 (1975).
17. Z. L. Xiao, P. Voss-de Haan, G. Jakob, and H. Adrian, Phys. Rev. B **57**, 736 (1998).
18. L. Miu, P. Wagner, U. Frey, *et al.*, Phys. Rev. B **52**, 4553 (1995).

Translated by E. Golyamina

JETP Letters, Vol. 74, No. 3, 2001, pp. 173–176. Translated from Pis'ma v Zhurnal Éksperimental'noĭ i Teoreticheskoĭ Fiziki, Vol. 74, No. 3, 2001, pp. 191–194.

Control of the Electron Spectrum of a Quasi-One-Dimensional Conductor $K_{0.3}MoO_3$ with the Use of a Microcontact

A. A. Sinchenko[1], V. Ya. Pokrovskiĭ[2]*, and S. G. Zybtsev[2]

[1] *Moscow Institute of Engineering Physics, Kashirskoe sh. 31, Moscow, 115409 Russia*

[2] *Institute of Radio Engineering and Electronics, Russian Academy of Sciences, ul. Mokhovaya 18, Moscow, 103907 Russia*

* *e-mail: pok@mail.cplire.ru*

Received July 3, 2001

When an electric field is applied to a Peierls quasi-one-dimensional conductor $K_{0.3}MoO_3$, a change in conductivity is observed in the vicinity of the point contact. This change is due to a strong local distortion of the charge density wave in the pinned state. In this case, the chemical potential can be varied over a wide range by changing the conductivity from the *n* type to the *p* type. The local position of the chemical potential can be determined by the method proposed; in particular, the low-temperature anomaly of conductivity is explained. © *2001 MAIK "Nauka/Interperiodica".*

PACS numbers: 72.15.Nj; 71.45.Lr; 73.20.Mf; 73.40.Ns

Electrons in quasi-one-dimensional conductors at temperatures below the Peierls transition temperature T_P condense to a charge density wave (CDW) [1]. In the region of voltages below the threshold value V_T for the beginning of CDW motion, the electronic properties of quasi-one-dimensional conductors are adequately described by the semiconductor CDW model ([2] and references therein). The essence of the model is that the transport properties in the case of a static CDW are determined by electron and hole excitations through the Peierls gap 2Δ, and the charge of quasiparticles $p - n$ changes as the CDW wave vector q changes: $q - q(T = 0) = \frac{1}{\pi}(p - n)$. The temperature dependence of the conductivity, the thermal emf, and the Hall coefficient, as well as the hysteresis of these values associated with a CDW distortion, can be explained within the framework of this model [2]. This distortion δq, that is, the deviation of q from an equilibrium value can be caused by the temperature prehistory and by an electric field. The hysteresis is due to the fact that, in order to change the wave vector, the CDW must break at a weak point for one period of the CDW to be created or annihilated, that is, for a phase slip (PS) to occur. For this purpose, it is necessary to stretch or compress the CDW to a critical value, which can be conveniently characterized by a shift of the chemical potential ζ. As a rule, the critical shift of the chemical potential comprises a value in the range of several millielectron-volts, that is, considerably smaller than kT (k is the Boltzmann constant): at larger distortions a CDW PS (that is, relaxation of the metastable state) occurs. Correspondingly, the hysteresis of the resistance $\delta R/R \lesssim 50\%$ is observed.

When an electric field $\lesssim E_T$ is applied to a sample of a Peierls conductor, a distortion of the CDW occurs in the vicinity of the contacts with the input lead; as the field further increases, PS centers form in the vicinity of the contacts, and CDW motion starts. As was mentioned above, in the case when the contact area is large, the shift of the chemical potential in the vicinity of the contacts is insignificant ($< kT$). A different situation may occur in the vicinity of a microcontact. Let us make a crude estimate. Assume that the size of the microcontact is $a \sim 100$ Å. Hence, the length of the CDW distortion region can be of the same order of magnitude, because the electric field is localized in a region with the characteristic size $\sim a$ [3]. In the case when a PS occurs, the change in q can be estimated at $\delta q = 2\pi/a$, and the corresponding $\delta\zeta_{2\pi}$ can be readily evaluated if the temperature dependence of the resistance $R(T)$ is known: $\delta\zeta_{2\pi} \approx \delta q(\delta\zeta/dq) \approx kT(\delta q/q)(R(T)/R(300\ \mathrm{K}))$ [4]. This value for typical Peierls conductors like $K_{0.3}MoO_3$ is many times higher than kT at all temperatures, except for the region in the vicinity of T_P. Thus, even a single PS event shifts the chemical potential by a large value.[1] This means that a PS does not occur before the shift of the chemical potential reaches even a half of $\delta\zeta_{2\pi}$. A CDW distortion opposite in sign and even larger in magnitude would arise otherwise. Hence, it may be suggested that a very large CDW distortion and a shift of the chemical potential can be obtained for the static CDW in the vicinity

[1] The shift of the chemical potential would be somewhat smaller if the PS occurred as a climb of a dislocation loop in the CDW. However, when the size of the contact is ~ 100 Å, the number of CDW chains that fall within the contact is of order 10, so that it makes no sense to speak about a dislocation.

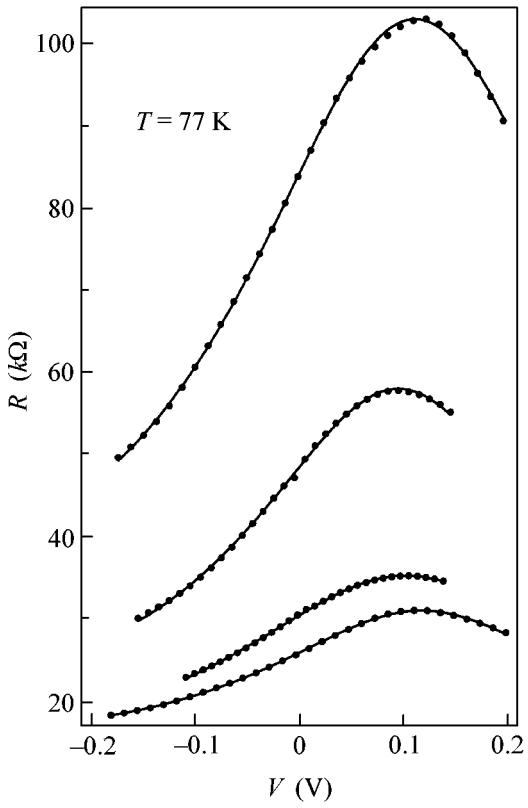

Fig. 1. Resistance of several Cu–$K_{0.3}MoO_3$ microcontacts as a function of the voltage applied to a microcontact. Points correspond to experiment, and solid lines are approximations by Eq. (1).

of a point contact of a sufficiently small area. The characteristics of point Cu–$K_{0.3}MoO_3$ contacts were studied in [5]. The asymmetric voltage dependence of the differential resistance obtained in [5] actually pointed to a CDW distortion in the vicinity of the contact. However, because the diameter of the contacts studied was too large and corresponded to the differential resistance $R_d(0) \lesssim 10^3\ \Omega$, a PS occurred even at low voltages. This was manifested in the $R_d(V)$ curves as a sharp decrease in resistance and an increase in noise.

In this work, an effort was made to study high-resistance point contacts of a normal metal (Cu) with single crystals of the blue bronze $K_{0.3}MoO_3$, with the aim of comprehensively studying the local CDW distortion and experimentally verifying the applicability of the model [2]. The blue bronze $K_{0.3}MoO_3$ is a typical quasi-one-dimensional CDW conductor, in which the Peierls transition occurs at $T_P = 180$ K. As compared with other quasi-one-dimensional conductors, blue bronze crystals are distinguished by relatively large sizes. This fact facilitates the preparation of point contacts to these samples, including those for passing a current along chains. Electrochemically sharpened copper wires 50 and 75 μm in diameter were used in this work as normal electrodes. The rounded radius of the needles did not exceed 1 μm. The point contacts were formed directly at a low temperature with the use of a high-precision mechanical transmission system. The contact diameter a was estimated by its resistance R using the Sharvin equation [6]: $R \approx \rho l/a^2$, where $\rho = 0.2\ \Omega$ cm is the resistivity of $K_{0.3}MoO_3$ at $T = 77$ K, and $l = 10$ nm is the mean free path [1]. Contacts with the resistance up to several hundreds of kiloohms, that is, $d \lesssim 100$ Å, were obtained and studied at $T = 78$ K. Unfortunately, obtaining temperature characteristics for these contacts turned out to be very difficult because of their low stability especially under variations of temperature.

Several typical dependences of resistance $R \equiv V/I$ on the voltage V applied to various point contacts at $T = 78$ K are displayed in Fig. 1. The contacts were created at the sample end; that is, the current passed along the conducting chains. As distinct from the contacts studied in [5], the resistance $R(V)$ (Fig. 1) varies smoothly; that is, the CDW remains static in the entire range of applied voltages. A maximum of the resistance is observed in all the curves at $V = V_0 > 0$. Under variations of the contact diameter and temperature, V_0 oscillated within the range 60–110 meV. We observed no systematic variations of $V_0(T)$ in the range 77–84 K. Curves similar to those shown in Fig. 1 were obtained only when the current in the contact passed strictly along the chains, that is, when the contact was created at a sample cleavage strictly perpendicular to the chains.

In order to reveal how the observed conductivity is related to the bulk crystal properties, we measured the temperature dependence of the volume resistance of a $K_{0.3}MoO_3$ sample from the same lot. The dependence $R_v(T)$ for a bulk crystal from the same lot is shown in Fig. 2 in a solid line, and the dark circles correspond to $R(0)$ for a stable microcontact for which it has been possible to perform measurements at several temperatures. The resistance of the microcontact has been multiplied by 3.1×10^{-3}. It is evident that the results virtually coincide with each other. This means that the conductivity of the microcontact at $V = 0$ reflects the bulk properties of the crystal, and the contact shift of the chemical potential is of minor importance. Both dependences below 100 K exhibit a departure from the activation law corresponding to $\Delta/k = 590$ K (dashed line). The dependence $R_M(T)$ is shown in the same figure (light circles), where R_M at each temperature corresponds to a maximum of $R(V)$ (Fig. 1). It is evident that the dependence $R_M(T)$ hardly deviates from the activation law down to the lowest temperatures, and the activation energy corresponding to the temperature $T = 590$ K is close to the known value Δ [7, 8]. Note that a deviation of the dependence $R(T)$ from the activation law at low temperatures is typical for all CDW materials [1].

The following qualitative picture stems from these results: a CDW distortion δq leads to partial screening of the electric field in the vicinity of the contact. This

results in a shift of the chemical potential $\delta\zeta \approx \delta q(d\zeta/dq)$ and in a change in resistance. A maximum of the resistance corresponds to the position of the chemical potential in the effective midgap ($\mu_n n = \mu_p p$, where μ_n and μ_p are the mobilities of electron and hole excitations, respectively), that is, to a transition from electron to hole conductivity. It is known from measurements of the thermal emf and the Hall effect [9] that blue bronze possesses *n*-type conductivity. A schematic diagram of energy bands in the vicinity of a point contact is shown in Fig. 3. The positive sign of V_0 corresponds to a downward shift of the chemical potential (assume that $\delta\zeta > 0$, which corresponds to a stretch of the CDW, $\delta q < 0$). Actually, it is evident in Fig. 3 that the CDW distortion in the vicinity of the contact is characterized by the property that the electric field determined by the gradient of the electrostatic potential (dashed curve in Fig. 3) decreases near the contact. At $V > 0$, the chemical potential in the vicinity of the contact drops down,[2] and can drop below the midgap in the case of a sufficiently large CDW distortion. Such a significant shift of the chemical potential of quasiparticles has not been observed previously. The departure of the temperature dependences of R_v and $R(0)$ from the activation law (Fig. 2) finds its natural explanation within the framework of the semiconductor model: as the temperature decreases, the average shift of the chemical potential in reference to the midgap becomes $\gtrsim kT$ in an equilibrium.

In order to describe $R(V)$ quantitatively (Fig. 1), note that the change in the resistance of the near-contact region is nonuniform (Fig. 3). For simplicity, represent R as a sum $R(\delta\zeta) + R_0$, where $\delta\zeta = bV$, and R_0 is independent of V [b is the coefficient of proportionality between V and $\delta\zeta$; the case $b = 1$ corresponds to the complete screening of the applied field (see Fig. 3)]. In other words, the region of the voltage drop will be considered as two sections connected in a series: one with a uniform shift of the chemical potential and another one with the resistance not depending on V,

$$R(V) = R_1/\cosh\left(\frac{b(V - V_0)}{kT}\right) + R_0. \qquad (1)$$

We have obtained an equation with four fitting parameters; the value of bV_0 gives an estimate for the initial shift of the chemical potential in reference to the effective midgap. Solid lines in Fig. 1 show the results of approximating the obtained $R(V)$ curves using Eq. (1). It is evident in the figure that the proposed model describes perfectly the experimental behavior. As a rule, R_1 is several times higher than R_0; that is, the CDW is distorted in virtually the entire region of contact voltage drop. The value of b was found equal to about 1/20, and, correspondingly, $\zeta_0 = aV_0 \approx 3$–5 meV. The comparatively low value of b means that the CDW only partly screens the field in the vicinity of the point contact, which is associated with pinning at impurities and at neighboring CDW chains. The initial shift of the chemical potential in reference to the effective midgap is small as compared to the gap itself; however, it is comparable with kT, which may explain the virtually unipolar (electron) conductivity type of blue bronze.

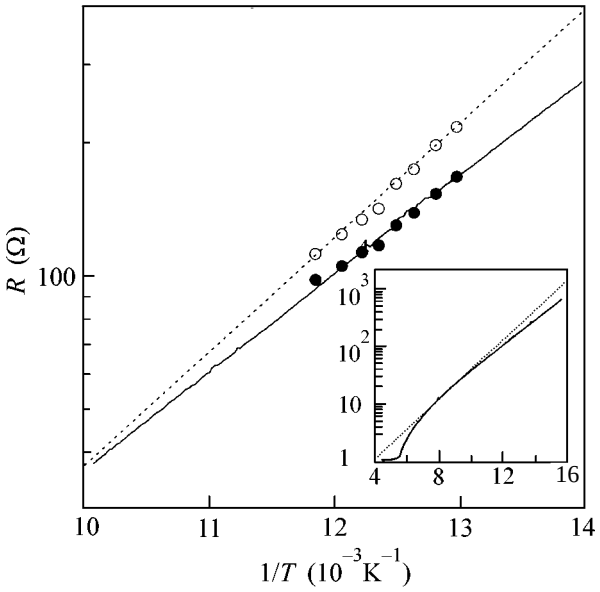

Fig. 2. Resistance as a function of the inverse temperature for a bulk single crystal (solid line) and also for a stable microcontact at $V = 0$ (dark circles) and at V corresponding to a maximum of $R(V)$ (light circles) in the temperature range 77–100 K. The resistance of the microcontact is multiplied by 3.1×10^{-3}. The inset shows the same in the range 63–300 K. The straight line with an activation energy of 590 K, which corresponds to the Peierls band gap for $K_{0.3}MoO_3$, is shown in a dashed line.

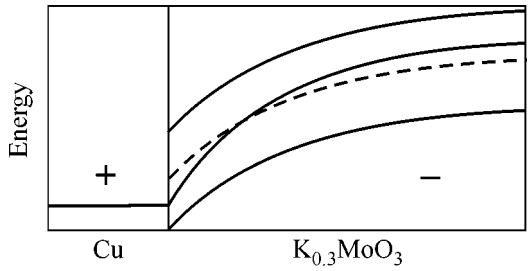

Fig. 3. Schematic diagram of energy bands in the vicinity of a metal–CDW point contact at $V > V_0$. The dash designates the effective middle of the Peierls gap (electrostatic potential). The electric field is partially screened in the vicinity of the contact: the slope of the electrostatic potential is less than that of the electrochemical potential (solid line). The electrochemical potential crosses the midgap (transition from the *n*-type to *p*-type conductivity).

[2] The same result will be obtained if we take into account that the (hole) CDW having a positive charge at $V > 0$ is stretched in the vicinity of the contact. In this case, the number of sites above the gap decreases, which results in an increase in the number of holes below the gap, that is, to a downward shift of the chemical potential.

Thus, we managed to observe a hysteresis-free CDW distortion in the vicinity of the point contact. The chemical potential can be controlled over a wide range of values with the use of a voltage applied to the microcontact. Even the sign of the majority carriers can be changed using this technique. In this case, the change in the resistance of the microcontact is described well within the framework of the semiconductor model of the CDW. It is shown that the deviation of the temperature dependence of the $K_{0.3}MoO_3$ resistance from the activation law observed at low temperatures is due to the fact that the equilibrium shift of the chemical potential in reference to the effective midgap ($\zeta_0 \approx 4$ meV) becomes comparable with kT. The results of this work showed that the proposed method of microcontact spectroscopy can be used for determining the local shift of the chemical potential in reference to the midgap and may turn out to be promising for studying defects and metastable states of CDW materials.

The authors are grateful to Yu.I. Latyshev, I.G. Gorlova, and A.V. Golovnya for help in this work, to S.V. Zaitsev-Zotov and S.N. Artemenko for discussions, and to R.E. Thorne for presenting $K_{0.3}MoO_3$ samples. This work was supported by the Russian Foundation for Basic Research (project nos. 99-02-17364, 99-02-17387, 01-02-16321, and 00-02-22000 NTsNI) and by the program "Physics of Solid-State Nanostructures" of the Ministry of Science of the Russian Federation, project no. 97-1052.

REFERENCES

1. *Charge Density Waves in Solids*, Ed. by L. Gor'kov and G. Grüner (Elsevier, Amsterdam, 1989); G. Grüner, in *Density Waves in Solids* (Addison-Wesley Reading, 1994).
2. S. N. Artemenko, V. Ya. Pokrovskiĭ, and S. V. Zaĭtsev-Zotov, Zh. Éksp. Teor. Fiz. **64**, 509 (1996) [JETP **83**, 590 (1996)].
3. I. O. Kulik, A. N. Omel'yanchuk, and R. I. Shekhter, Fiz. Nizk. Temp. **3**, 1543 (1977) [Sov. J. Low Temp. Phys. **3**, 740 (1977)].
4. V. Ya. Pokrovskii and S. V. Zaitsev-Zotov, Synth. Met. **32**, 321 (1989).
5. A. A. Sinchenko, Yu. I. Latyshev, S. G. Zybtsev, and I. G. Gorlova, Pis'ma Zh. Éksp. Teor. Fiz. **67**, 146 (1998) [JETP Lett. **67**, 164 (1998)].
6. Yu. V. Sharvin, Zh. Éksp. Teor. Fiz. **48**, 984 (1965) [Sov. Phys. JETP **21**, 655 (1965)].
7. B. Dardel, D. Malterre, M. Grioni, *et al.*, Europhys. Lett. **19**, 525 (1992).
8. G. Travaglini, P. Wachter, J. Marcus, and C. Schlenker, Solid State Commun. **37**, 599 (1981).
9. *Low-Dimensional Electronic Properties of Molybdenum Bronzes and Oxides*, Ed. by C. Schlenker (Kluwer, Dordrecht, 1989).

Translated by A. Bagatur'yants

JETP Letters, Vol. 74, No. 3, 2001, pp. 177–181. Translated from Pis'ma v Zhurnal Éksperimental'noĭ i Teoreticheskoĭ Fiziki, Vol. 74, No. 3, 2001, pp. 195–199.

Fullerene Model of Silicon Nanofibers

E. F. Sheka[1], E. A. Nikitina[1], V. A. Zaets[2]*, and I. Ya. Ginzburg[2]

[1] *Peoples Friendship University, ul. Miklukho-Maklaya 6, Moscow, 117198 Russia*

* *e-mail: sheka@icp.ac.ru*

[2] *Institute of Problems of Chemical Physics, Russian Academy of Sciences, Chernogolovka, Moscow region, 142432 Russia*

Received January 16, 2001; in final form, July 3, 2001

A computational (quantum-chemical) experiment has been performed on constructing a silicon nanofiber by gas-phase deposition. A model of two-step polymerization has been proposed in which a fullerene Si_{60} molecule serves as the main structural unit. The formation of oligomers of the molecule containing from three to eight molecular units explains the discrete values of the fiber width observed experimentally. The formation of a "rouleau" of oligomers leads to fiber growth in terms of length. It is shown that both steps are favorable in energy with the decisive superiority of a high-spin state, which poses the question of considering silicon nanofibers to be molecular magnets. © *2001 MAIK "Nauka/Interperiodica".*

PACS numbers: 61.48.+c; 61.46.+w

Silicon nanofibers synthesized from gas-phase atomic silicon on the surface of highly oriented pyrolytic graphite [1] represent a new kind of nanosized silicon. It was shown that the formation of fibers is preceded by the occurrence of compact spheroidal silicon clusters, which are found on the graphite surface at coverages far from monolayer ones. These clusters are weakly bound with the surface and possess a significant kinetic energy acquired during their generation in hot atomic gas. They easily diffuse over the surface and readily coagulate, which leads to the formation of bundles of nanofibers when the pressure of the atomic gas exceeds a certain critical value. This empirical picture was the basis of the fullerene–polymer structure of fibers with the fullerene Si_{24} structure proposed by the authors as the main building block of the polymer. However, while explaining the possibility of the longitudinal growth of a fiber as a polymer chain, the authors did not consider the question of fiber thickness. The thickness, as follows from the same experiments, is strictly deterministic and varies in a discrete way, comprising 3, 4, 7, and 10 nm. At the same time, remaining within the framework of the fullerene–polymer model, one may naturally assume that the fiber thickness is also formed in the process of fullerene polymerization. In this case, fullerene oligomers differing in length are responsible for on one hand, strictly fixed fiber thickness, and on the other hand, discretely varying fiber thickness. From the thickness values listed above, it is evident that the linear dimension of a "monomer" forming the oligomer must be of order 1 nm, which considerably exceeds the lateral dimension of the Si_{24} molecule. In this work, a computational synthesis of a silicon fiber was performed based on the assumption of the two-step polymerization of a Si_{60} fullerene as a monomer unit. The first part of this computational experiment was in a detailed investigation of fullerene itself, and the second part of this work is devoted to its polymerization (oligomerization).

Calculations were carried out using the semiempirical quantum-chemical AM1 method [2]. This SCF MO LCAO method is based on the one-electron Hartree–Fock approximation in the valence basis set under the following assumptions: (1) the wave functions of neighboring atoms do not overlap, and (2) only two-electron two-center integrals are considered among the remaining molecular integrals, whose contribution is determined by the corresponding parameters obtained by comparing calculated results with experimental data for a certain set of reference compounds. The calculations were performed using both the sequential uniprocessor [3] and parallel multiprocessing [4] versions. In the latter case, the calculations were performed on two clusters of 16 processors: an Intel® PIII cluster based on Pentium® III 667 MHz processors integrated by a 3COM switch using the 100 Mbit Fast Ethernet technology and a MBC-1000M Alpha 21264 cluster.

Si_{60} monomer. Theoretically, the existence of the Si_{60} molecule was considered many times (see [5] and references therein). Experimental efforts to synthesize or discover silicon fullerenes were started almost immediately after discovering carbon analogues. However, it turned out that silicon clusters with a pure unterminated surface are extremely reactive and can be

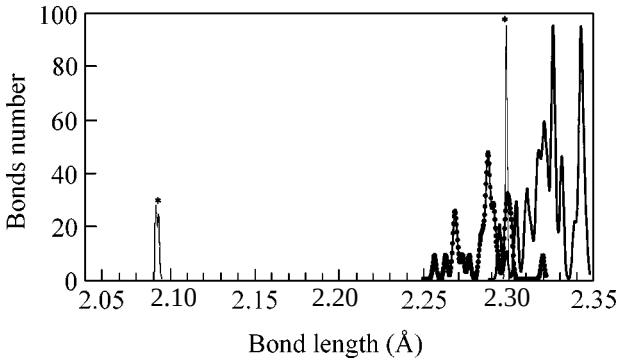

Fig. 1. Bond lengths in the Si_{60} molecule. The curves were constructed using the Gaussian function $\exp(-l^2/\lambda^2)$ with the broadening parameter $\lambda = 0.0005$ Å.

obtained in molecular beams only under high-vacuum conditions (see [6, 7] and references therein). The density of the number of clusters is low; therefore, their composition and structure cannot be reliably identified. As a consequence, only indirect experimental evidence of the existence of silicon fullerenes of the Si_{60} type is available so far. Thus, as early as ten years ago, it was found in experiments on the adsorption of ammonia on positive Si_n ions that the average number of ammonia molecules bound with one Si_n ion is six [8]. In similar experiments with carbon ions, the number six was reached only in the adsorption of ammonia on C_{60} ions [9]. It is possible that nanofibers [1] discussed in the article represent another indirect evidence of the existence of this fullerene.

The main distinction of this investigation from previous works was that the calculations were carried out not only for the singlet state but also for high-spin configurations. Fullerene Si_{60} is an open silicon structure, which is characterized by high free valences of all its atoms. In this connection, it should be expected that its ground state, as in the case of other open silicon structures [10–12], is stabilized through an ordered arrangement of spins in higher spin states. The starting molecular structure was constructed similarly to its carbon C_{60} prototype molecule. The lengths of all Si–Si bonds were equal to 2.35 Å. This value is characteristic of cubic crystalline silicon. The structure obtained is geometrically closed without any visible traces of stresses. After searching a minimum of the total energy in a cycle of full geometry optimization, the initial structure is transformed to equilibrium states calculated for the singlet, triplet, quintet, and septet spin states. All the obtained structures possess the configuration of a truncated icosahedron consisting of 20 hexagons and 12 pentagons and look rather similar. The maximal horizontal and vertical dimensions of molecules are given in Table 1. It is evident from the table that the molecule possesses the smallest dimensions in the singlet state, and both the dimensions are smaller than those for the initial geometry (1.17 and 1.14 nm). On the contrary, the molecular dimensions in high spin states notably increase as compared with the starting ones and fall into a narrow range of values.[1] The size and the shape of the molecule are determined by the distribution of Si–Si bond lengths. Two narrow peaks at 2.094 and 2.298 Å marked with stars in Fig. 1 are related to the singlet structure. The first of them relates to the reduced conjugated Si=Si bond, whereas the second peak describes ordinary Si–Si bonds.[2] There are two long bonds for each short bond. The dipole moment is virtually equal to zero, the molecular symmetry is I_h. The picture obtained is fully similar to that for the C_{60} molecule,[3] so that one may speak about an $sp^{2.5}$ configuration for silicon atoms in the singlet state of the molecule.

The set of peaks in the region 2.25–2.35 Å describes the structure of the molecule in the triplet state, which is formed in this spin state by only ordinary Si–Si bonds. The curve with points and the solid curve describe bonds that correspond to short and long bonds of the singlet molecule, respectively. As before, there are two "long" bonds in the range 2.30–2.35 Å for each short bond in the range 2.25–2.30 Å. The width of the distribution makes up 0.1 Å, which points to the smearing of symmetry at the atomic positions in reference to the I_h symmetry of the singlet molecule. Actually, the symmetry of the molecule in the triplet state is reduced to C_i, which is the reason for the deviations from zero of the molecular dipole moments given in Table 1. The symmetry of the molecule in the quintet and septet spin states is C_i, and the distribution of bond lengths is equivalent to the triplet one.

Table 1 also gives the heats of formation of the molecule. It is evident from the calculated data that the energies of the Si_{60} molecule in the high-spin states are significantly lower than the energy of the singlet state and fall in a narrow range 2–3 kcal/mol in width. Thus, the ground state of the Si_{60} molecule is spin-mixed because of the quasi-degeneracy of the molecular energy with respect to spin. The electron configuration of atoms in this case corresponds to an sp^3 hybridization, which is maintained by the spin density on atoms (which is different from zero), in addition to the electron density, which is responsible for the formation of three chemical bonds of a given atom with the neighboring ones.

The result obtained continues the tendency discovered for open silicon structures, exemplified by the Si_2 molecule [10] and the crystal Si(111)(7 × 7) [11] and Si(001)(2 × 1) [12] surfaces, whose triplet configurations turn out to be significantly more favorable in

[1] In order to assign the structures obtained to a minimum of the total energy, the signs of the second derivatives of the energy with respect to molecular coordinates were verified in the calculation.

[2] The bond order was determined by the Wiberg index [13], which equals 1.685 and 1.078 for the short and long bonds, respectively.

[3] According to our calculation, the corresponding C–C bond lengths comprise 1.384 and 1.463 Å, and the Wiberg indices are 1.495 and 1.078, respectively.

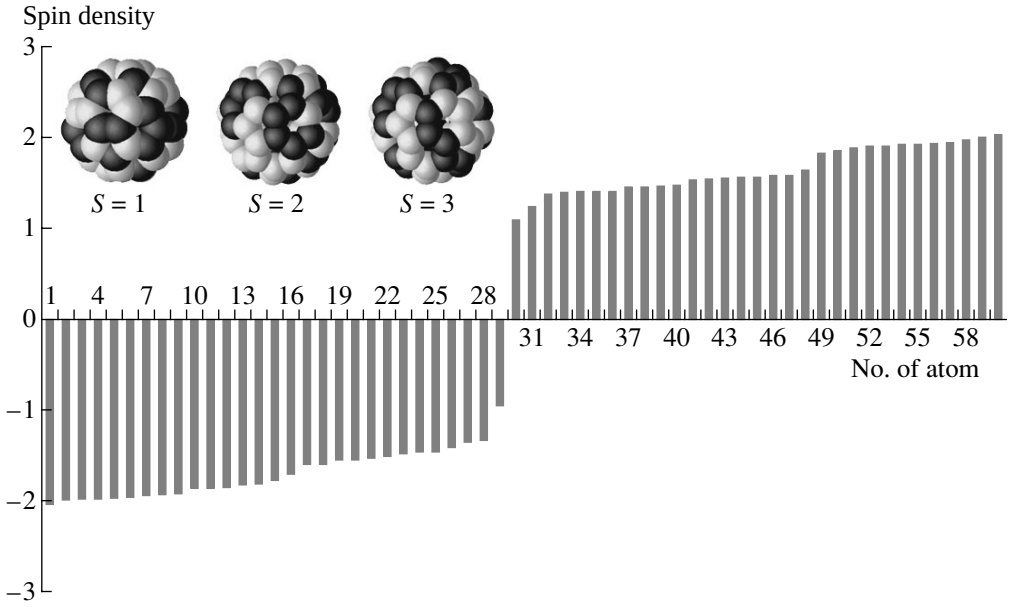

Fig. 2. Distribution of spin densities over atoms of Si_{60} fullerene.

energy (by 20–40%). The occurrence of a spin density in the ground state of these structures allows one to class them among the objects possessing molecular magnetism [14]. After recent experiments using an STM in combination with polarization analysis [15] and those combined with studying second harmonic generation [16], the molecular magnetism of the silicon Si(111)(7 × 7) surface predicted earlier [11] has become the experimental reality.

The distribution of the spin density in the Si_{60} molecule in the triplet state is shown in Fig. 2. The distributions for the quintet and septet are similar. The spin densities were arranged in ascending order. It is evident in the figure that the distribution function is rather symmetric with respect to negative and positive values, whose spread does not exceed 14%. As a result, the spin density distribution over the atoms of the molecule can be visualized using a dichromatic representation in which the light and dark markings correspond to a positive or negative spin density. The Si_{60} molecule painted in such a way is shown in the inset in Fig. 2 for three spin states. It is evident in the figure that a speckle structure of the spin density distribution is characteristic of all spin states.

Oligomerization of Si_{60} molecules. It follows from Table 1 that the maximal lateral dimension of the Si_{60} molecule comprises 1.08 and 1.44 nm for the singlet and triplet structures, respectively. If it is assumed that this molecule is the main building block of silicon fibers in [1], the formation of fibers can be thought of as the multiplication of chains containing two, three, or five molecules along the fibers. An indirect confirmation of the possibility of this process is the photopolymerization of C_{60} molecules (to dimers and trimers) deposited on a silicon surface, as was observed recently in [17]. It was shown that the STM data are explained well by the dumb bell structure of the dimer in which the molecules present axial hexagons to each other. Chemical C–C bonds form between these hexagons, so that the junction represents a regular hexahedral prism. We used this structure of the junction between two fullerene molecules in constructing models of oligomer chains $\{Si_{60}\}_n$ with n taking all the values from two to eight. The calculations of these models were performed with full geometry optimization for the singlet and triplet spin configurations. It was shown that the oligomers are constructed by simple chain growth through the hexahedral prismatic junction. The structure of chains in the singlet and triplet states is not distinguished by eye. Table 2 presents the heats of formation of oligomers and the binding energies of molecules in oligomers per one molecule E_b, which were determined in accordance with the following relationship:

$$E_b = \{\Delta H[\{Si_{60}\}_n] - n\Delta H[Si_{60}]\}/n.$$

Table 1. Main characteristics of the Si_{60} molecule

	Si_{60}		
	dimension, nm $\langle x\rangle_{max}/\langle y\rangle_{max}$	heat of formation, kcal/mol	dipole moment, D
Starting structure	1.17/1.14		
Singlet	1.08/1.02	1315.08	0.000
Triplet	1.44/1.29	1028.52	0.159
Quintet	1.46/1.20	1031.35	0.183
Septet	1.39/1.28	1029.28	0.154

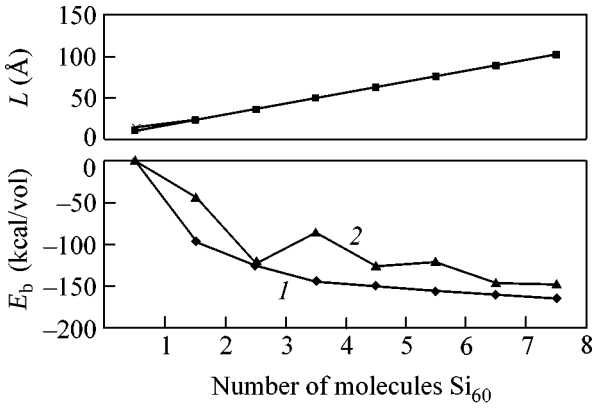

Fig. 3. Binding energy E_b (lower part) and the oligomer length L (upper part) as functions of the number of monomer molecules: (*1*) singlet and (*2*) triplet.

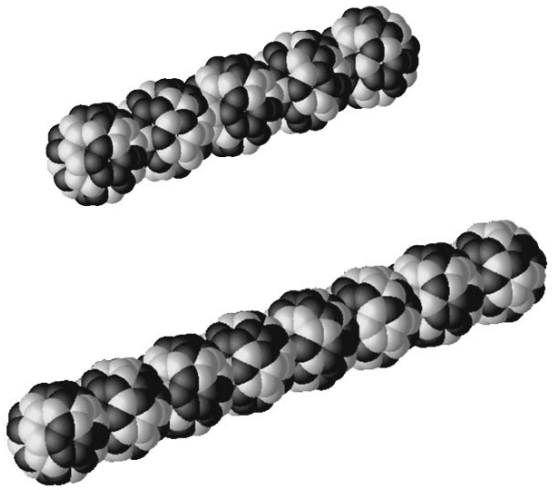

Fig. 4. Spin density distribution over the atoms of $5Si_{60}$ and $8Si_{60}$ oligomers in spin triplet state.

Here, $\Delta H[\{Si_{60}\}_n]$ and $\Delta H[Si_{60}]$ are the heats of formation of the nth oligomer and the free molecule, respectively, in a given spin state.

It follows from the data reported that polymerization and (or) oligomerization of Si_{60} molecules are favorable in energy. The second conclusion relates to the statement that the predominant formation of oligomers in a high-spin configuration is favorable in energy, because the heat of formation of an oligomer is significantly lower in all cases. The dependence of the binding energy E_b and the linear dimension of an oligomer on the number of monomer units is shown in Fig. 3. It is evident in the figure that the singlet and triplet configurations are virtually equivalent from the point of view of bonding energy. The binding energy steadily grows in both cases as the number of molecules in the chain increases. However, whereas this growth is monotonic for the singlet configuration, it is markedly modulated for the triplet one. This fact can also explain in energy terms the occurrence of a certain modulation in the probability of the formation of oligomers differing in composition. Thus, from the energy point of view, it is favorable to for oligomers with the number three (L = 3.66 nm), then five and six (L = 6.24–7.54 nm), and finally, seven and eight (L = 8.85–10.15 nm). These data explain the experimental data on bundles of nanofibers with a thickness of 4, 7, and 10 nm [1]. In this model, there are no fibers with a thickness of 3 nm. However, according to the experimental data reported in [1], the bundles of the corresponding fibers are inconsiderable in number and are of low intensity. It may be suggested that a fullerene of lower composition participates in their formation.

Table 2. Heats of formation of oligomers of the Si_{60} molecule, kcal/mol

	Singlet		Triplet	
	ΔH	ΔH per molecule	ΔH	ΔH per molecule
Si_{60}	1315.08		1028.52	
$2 \cdot Si_{60}$	2438.17	–96	1969.28	–44
$3 \cdot Si_{60}$	3571.25	–125	2721.09	–122
$4 \cdot Si_{60}$	4697.50	–144	3768.64	–86
$5 \cdot Si_{60}$	5823.82	–150	4513.92	–126
$6 \cdot Si_{60}$	6950.12	–157	5437.97	–122
$7 \cdot Si_{60}$	8076.41	–161	6170.18	–147
$8 \cdot Si_{60}$	9202.74	–165	7046.04	–148

Fullerene-based silicon nanofibers are open structures with spin-mixed ground states which means these structures should also be assigned to molecular magnets. The expected distinctness of magnetic properties is associated with the spin density whose distribution over oligomer atoms is similar to that for the free molecule in Fig. 2. In Fig. 4, this distribution is visualized in a dichromatic way for the triplet state of the pentamer and octamer. It is evident that, as the length of an oligomer increases, the distribution acquires pronounced features of a fractal nature.

Whereas the fixed fiber width is specified by the oligomer of a certain length, the fiber can grow in length only in the case of effective secondary polymerization. However, in this case, it should be the polymerization of oligomers. The interaction between oligomers was studied in this work using two dimers and two trimers as examples. The value of E_b per one oligomer is comparable with the interaction energy of molecules in an oligomer.

The computational experiment performed in this work showed that Si_{60} silicon fullerenes are character-

ized by the spin-mixed ground state, because the heats of formation of the molecule in different high-spin states are almost equal to each other (close to degeneracy). The atomic configurations of silicon atoms correspond to an sp^3 hybridization, which is maintained by high spin densities on atoms in addition to the electron density providing the chemical bonding of this atom with its neighbors. In this work, a model is suggested for the formation of a silicon nanofiber through two polymerization processes in which this molecule is considered the main building block. The primary process is responsible for the formation of an oligomer of Si_{60} molecules determining the fiber thickness. The secondary process binds the oligomers with each other with the growth of the fiber in length. Within the framework of this model, nanofibers represent open structures with a high free valence of the constituent atoms and a high-spin configuration of the ground state. The high spin density on atoms must reveal itself in peculiar magnetic properties of this new substance, which represents a molecular magnet.

REFERENCES

1. B. Marsen and K. Sattler, Phys. Rev. B **60**, 11593 (1999).
2. M. J. S. Dewar, E. G. Zoebisch, E. F. Healey, and J. J. P. Stewart, J. Am. Chem. Soc. **107**, 3902 (1985).
3. V. A. Zaets, *Program Complex of Quantum-Chemical Computations CLUSTER-Z1* (Inst. Khimii Poverkhnosti Nats. Akad. Nauk Ukrainy, Kiev, 1991).
4. P. K. Berzigiyarov, V. A. Zaets, I. Ya. Ginzburg, *et al.*, *Program Complex of Parallel Quantum-Chemical Computations in sp-Basis MP-AM1* (Inst. Problem Khim. Fiz. Ross. Akad. Nauk, 2000).
5. Bao-xing Li, Pei-lin Cao, and Duan-lin Que, Phys. Rev. B **61**, 1685 (2000).
6. L. R. Anderson, S. Maruyama, and R. E. Smalley, Chem. Phys. Lett. **176**, 348 (1991).
7. U. Ray and M. F. Jarrold, J. Chem. Phys. **94**, 2631 (1991).
8. M. F. Jarrod, Y. Ijiri, and U. Ray, J. Chem. Phys. **94**, 3607 (1991).
9. A. Ilirsh, Q. Li, and F. Wudl, Angew. Chem. Int. Ed. Engl. **30**, 1309 (1991).
10. *Molecular Constants of Inorganic Compounds*, Ed. by K. S. Krasnov (Khimiya, Leningrad, 1979).
11. V. Khavryutchenko, E. Sheka, M. Aono, and D.-H. Huang, Phys. Low-Dimens. Struct., No. 3/4, 81 (1998).
12. E. F. Sheka, in *Proceedings of the First International Symposium on Nanoarchitechtonics Using Suprainteraction—NASI-1, Tsukuba, Japan, 2000*, p. 28.
13. K. B. Wiberg, Tetrahedron **24**, 1083 (1968).
14. *Molecular Magnetism*, Ed. by K. Itoh and M. Kinoshita (Kodansha, Tokyo, 2000).
15. Z. H. Wu, T. Nakayama, and M. Aono (RIKEN Collab.), in *Proceedings of the First International Symposium on Nanoarchitechtonics Using Suprainteraction—NASI-1, Tsukuba, Japan, 2000*, quoted by M. Aono.
16. T. Suzuki, V. Venkataraman, and M. Aono, in *Proceedings of the First International Symposium on Nanoarchitechtonics Using Suprainteraction—NASI-1, Tsukuba, Japan, 2000*, p. 64.
17. T. Nakayama, J. Onoe, K. Nakatsuji, *et al.*, Surf. Rev. Lett. **6**, 1073 (1999).

Translated by A. Bagatur'yants

JETP Letters, Vol. 74, No. 3, 2001, pp. 182–185. Translated from Pis'ma v Zhurnal Éksperimental'noĭ i Teoreticheskoĭ Fiziki, Vol. 74, No. 3, 2001, pp. 200–203.

Long Electron Spin Memory Times in Gallium Arsenide

R. I. Dzhioev[1], B. P. Zakharchenya[1], V. L. Korenev[1]*, D. Gammon[2], and D. S. Katzer[2]

[1] *Ioffe Physicotechnical Institute, Russian Academy of Sciences, Politekhnicheskaya ul. 26, St. Petersburg, 194021 Russia*

** e-mail: korenev@orient.ioffe.rssi.ru*

[2] *Naval Research Laboratory, Washington DC 20375, USA*

Received July 6, 2001

Extremely long electron spin memory times in GaAs are reported. It was established by the optical orientation method that the spin relaxation time of electrons localized at shallow donors in *n*-type gallium arsenide ($N_d - N_A \approx 10^{14}$ cm^{-3}) is 290 ± 30 ns at a temperature of 4.2 K. The exchange interaction of quasi-free electrons and electrons at donors suppresses the main spin-loss channel for electrons localized at donors—spin relaxation due to the hyperfine interaction with lattice nuclei. © *2001 MAIK "Nauka/Interperiodica".*

PACS numbers: 71.35.-y; 73.61.Ey; 78.55.Cr

1. In recent years, spin phenomena in semiconductors have attracted considerable interest due to the idea of using spin degrees of freedom for data recording, storage, and retrieval [1]. In particular, long electron spin memory times are necessary for data processing on quantum computers, where electron spin is used as a bit [2]. In this respect, *n*-type gallium arsenide represents a promising material, because it displays long-time spin dynamics. It was established that the electron spin relaxation time in *n*-GaAs with the difference in concentrations of donor and acceptor impurities $N_d - N_A \approx 10^{13}$ cm^{-3} is $\tau_s = 30$ ns at helium temperatures [3]. It was found in [4] that $\tau_s = 42$ ns at $N_d - N_A \sim 10^{15}$ cm^{-3}. The time $\tau_s = 130$ ns was reported in [5].

This work presents the experimental results on the Hanle effect in *n*-GaAs ($N_d - N_A \approx 10^{14}$ cm^{-3}) upon quasi-resonant exciton excitation at $T = 4.2$ K. It is shown that the spin lifetime at weak pumping is determined by the electron spin relaxation time $\tau_s = 290 \pm 30$ ns. This is by far the longest time among the presently known electron spin relaxation times in GaAs. It is caused by the suppression of the main spin-loss channel for electrons localized at donors—relaxation due to the hyperfine interaction with lattice nuclei. The exchange interaction between the quasi-free electrons from the barrier regions and the electrons at donors is at the basis of this effect.

Electrons with spins oriented along the exciting beam are produced in semiconductors upon the interband absorption of circularly polarized light [6]. If the photoexcited carriers do not completely lose spin orientation during their lifetime, the photoluminescence (PL) will be partially circularly polarized. The degree of circular polarization for the photoluminescence in GaAs is determined by the projection S_z of the average electron spin onto the direction of the exciting beam (z axis); for the homogeneous spin-density distribution in space, it is given by the simple expression $\rho = S_z$. The hole polarization is zero because of the fast spin relaxation. Under these conditions, the maximal degree $\rho = 25\%$ [6].

2. The experiments on optical orientation were performed with a sample containing semi-insulating GaAs substrate, on which a layer of GaAs (5000 Å) and an AlAs barrier (250 Å) separating the main structure from the substrate were grown by molecular beam epitaxy. Then a GaAs layer (1000 Å), capped with an $Al_{0.3}Ga_{0.7}As$ (250 Å) barrier followed by a series of five quantum wells of different thickness was built up. The residual doping corresponded to the *n*-type impurity concentration at a level of 10^{14} cm^{-3}. The main contribution to the GaAs PL comes from the 1000-Å layer that is bounded by barriers on both the substrate and quantum well sides. The presence of quantum wells is insignificant because measurements were made with quasi-resonant excitation of GaAs in the transparent region of quantum wells. The light absorption depth in GaAs (~1 μm) far exceeds the thickness of the buffer layer under study, so that the charge carriers and excitons are homogeneously distributed in the layer. The small thickness allows the reemission effect to be ignored.

The sample was placed in a liquid helium cryostat and excited by the beam of a tunable Ti:sapphire laser. The circular polarization changed its sign with a frequency of 26.61 kHz using a photoelastic quartz modulator to get rid of the Overhauser effect on the shape of the electron magnetic depolarization curve [6]. The geomagnetic field was compensated and did not exceed 0.1 G in the sample location. The PL polarization was measured in the "reflection" geometry by an analyzer of circular polarization (quarter-wave phase plate and

linear polarizer). The PL was analyzed by a double-grating spectrometer with a dispersion of 5 Å/mm. Electronic circuit measured the effective degree of circular polarization $\rho = (I_+^+ - I_+^-)/(I_+^+ + I_+^-)$, where I_+^+ and I_+^- are the intensities of the PL σ^+ component for the σ^+ and σ^- excitations, respectively. In our case, circular dichroism was insignificant and the degree ρ could be regarded as a Stokes parameter characterizing the circular polarization of PL.

The PL spectrum is dominated by two lines corresponding to the recombination of a free exciton (line *X*) and an exciton bound to neutral donor (D^0–*X* line) [7]. The emission depolarization in a magnetic field perpendicular to the *z* axis (Hanle effect) was measured for the different sections of the PL spectrum. Note that the shape of the magnetic depolarization curve (Hanle curve) is identical for the *X* and D^0–*X* transitions. Below, the results on the Hanle effect are presented for the emission at 1.5155 eV corresponding to the exciton recombination. The PL magnetic depolarization curves measured upon the quasi-resonant exciton excitation (photon energy $h\nu$ = 1.5165 eV) with different excitation densities *W* are shown in Fig. 1. The dots in Fig. 1a correspond to the excitation density W = 2 mW/cm^2 and, in Fig. 1b, to 40 mW/cm^2. One can see that both the zero-field polarization $\rho(0)$ and the halfwidth of the Hanle effect increase with a rise in pumping. The experimental dependence of the degree $\rho(0)$ on the excitation density *W* is shown in Fig. 2a.

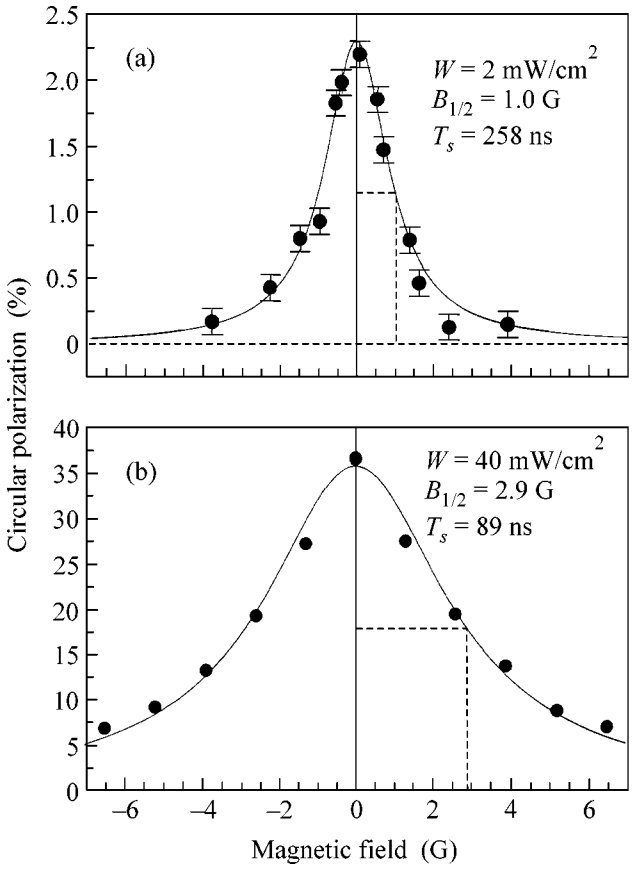

Fig. 1. Photoluminescence magnetic depolarization curves (Hanle effect) for the quasi-resonant exciton excitation (photon energy $h\nu$ = 1.5165 eV). Excitation density W = (a) 2 and (b) 40 mW/cm^2. Solid lines are constructed using Eq. (3).

The experimental results can be interpreted within the framework of a model of electron optical orientation in *n*-type GaAs [6]. The basic positions of this model are as follows. A circularly polarized light prepares electrons with a preferred spin direction. If electrons with spins "up" and "down" recombine with equal probability and the spin relaxation is slow, the spin polarization will accumulate. Then the equilibrium electrons in the steady state will be oriented, even if the pumping is weak and, hence, the number of excess electrons is smaller than the number of equilibrium electrons. The steady-state value of the average electron spin is

$$S_0 = S_i \frac{\tau_s}{\tau_s + \tau_J}, \quad (1)$$

where the initial average electron spin S_i is determined by the selection rules. The time τ_J is the electron characteristic lifetime. Its steady-state value is

$$\tau_J = N/G. \quad (2)$$

Here, *N* is the electron concentration, which is equal to the equilibrium concentration at weak pumping, and *G* is the number of electron–hole pairs created by light in unit time in a unit volume. One can see from Eqs. (1) and (2) that, consistent with the experiment, the lifetime increases and the average electron spin (and, hence, the degree ρ) decreases to zero with a decrease in light intensity (Fig. 2a). The solid line in Fig. 2a is constructed using Eqs. (1) and (2) for S_i = 50% and $\tau_s/\tau_J = 0.05W$, where the excitation density *W* has dimensionality mW/cm^2. After applying an external magnetic field perpendicularly to the exciting beam, the average electron spin precesses about the field with the Larmor frequency $\omega = \mu_B g_e B/\hbar$ (g_e is the electron *g* factor and μ_B is the Bohr magneton). Under steady state conditions, the projection S_z of electron spin onto the initial direction decreases with increasing field, resulting in the PL depolarization (the Hanle effect). The $S_z(B)$ dependence is described by the formula [6]

$$S_z(B) = \frac{S_0}{1 + (\omega T_s)^2}, \quad (3)$$

where the average spin in zero field S_0 is given by Eq. (1). The reciprocal spin lifetime

$$T_s^{-1} = \tau_s^{-1} + \tau_J^{-1} = \tau_s^{-1} + G/N \quad (4)$$

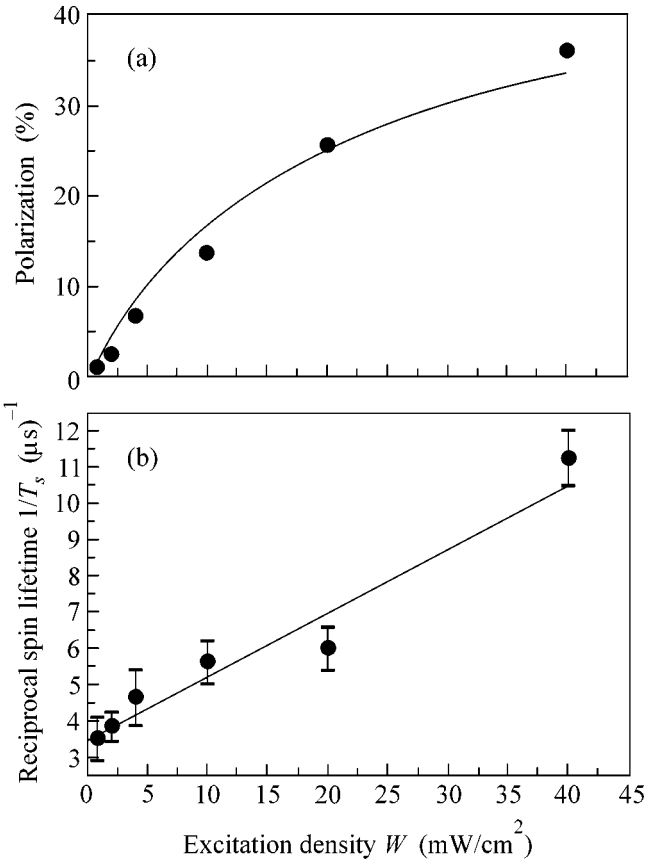

Fig. 2. (a) Degree of PL circular polarization as a function of excitation density in zero field (dots). Solid line is constructed using Eqs. (1) and (2) with $S_0 = 50\%$ and $\tau_s/\tau_J = 0.05W$. (b) Reciprocal spin lifetime as a function of excitation density (dots). The straight line is drawn according to Eq. (5).

can be determined by measuring the halfwidth of magnetic depolarization curve $B_{1/2} = \hbar/\mu_B g_e T_s$. It follows from Eq. (4) that the spin lifetime in the weak-pump limit is equal to the electron spin relaxation time. The experimental results are adequately described by Eq. (3) with $S_0 = 2.3\%$ and $B_{1/2} = 1.0$ G (solid curve in Fig. 1a). Knowing the halfwidth of the Hanle curve, one obtains $T_c = 258$ ns ($g_e = -0.44$ [8]). The spin lifetime shortens with a rise in pumping. The curve in Fig. 1b is constructed for $S_0 = 36\%$ and $B_{1/2} = 2.9$ G. In this case, $T_s = 89$ ns. The dependence of T_s^{-1} on the pump intensity is shown in Fig. 2b. It is approximated well by the linear function

$$T_s^{-1} = (3.5 \pm 0.4) + (0.17 \pm 0.02)W, \qquad (5)$$

where time T_s is expressed in microseconds and light intensity is in mW/cm^2. In the weak-pump limit, $T_s = \tau_s = 290 \pm 30$ ns. As was pointed out above, this time is the longest among the spin relaxation times ever reported in the literature for conduction electrons in gallium arsenide. The concentration of equilibrium electrons can be determined from the slope of the experimental curve $T_s(W)$ using Eq. (4). To do this requires the knowledge of the relation between the number of carrier pairs created in unit time in a unit volume and the excitation density W. This relationship has the form

$$G = (1 - R)\frac{\alpha W}{h\nu}, \qquad (6)$$

where the reflectivity of GaAs surface is $R \approx 0.3$, the absorption coefficient of gallium arsenide for the resonant excitation of an exciton is $\alpha \approx 1.2 \times 10^4$ cm^{-1} [9], and the photon energy $h\nu = 1.5165$ eV. Using Eqs. (4)–(6), one can determine the concentration of equilibrium electrons $N \approx 1.8 \times 10^{14}$ cm^{-3}. Therefore, the number of equilibrium electrons determined by the optical orientation method corresponds to a residual doping level of $\sim 10^{14}$ cm^{-3}.

3. According to the theory of optical orientation [6], the limiting degree of polarization in an unstrained bulk GaAs is 25%. However, the fitting procedure with the use of Eqs. (1) and (2) gives the limiting value $\rho = 50\%$. This may be due to a small residual stretching strain along the growth axis in the GaAs layer, resulting in the splitting of the hole levels $|\pm 3/2\rangle$ and $|\pm 1/2\rangle$ by a value on the order of kT. In this case, holes mainly fill the upper levels $|\pm 3/2\rangle$, so that $\rho = 2S_z$ [6] and the limiting degree of polarization becomes $\rho = 50\%$.

The circularly polarized light with $h\nu = 1.5165$ eV creates excitons whose emission polarization is the subject of investigation. At low temperatures, equilibrium electrons are bound to donors. In what way does the electron spin of an exciton obtain information about the polarization of equilibrium electrons localized at donors? The matter is that the spin-flip electron–electron scattering efficiently mixes electron spin over different states [10]. It is shown in the cited work that, down to the lowest pump intensities, the average electron spin is the same in different states. The efficient averaging is also evident from the fact that the shapes of depolarization curves for the X and D^0–X lines are the same, although their PL polarizations in the zero field differ by more than an order of magnitude. The difference in the initial polarizations is due to the difference in the selection rules for these two transitions [7]. At weak pumping (the number of excitons $n_x \ll N$), the relaxation of the total average spin is determined by the spin relaxation of the electrons localized at donors [10]. For this reason, the observed time $\tau_s = 290 \pm 30$ ns corresponds to the spin relaxation of electrons at donors.

Let us discuss the reasons for the long spin relaxation time of electrons localized at donors. Four basic mechanisms of electron spin loss in gallium arsenide are known [6]: the D'yakonov– Perel' and Elliott–Yafet mechanisms based on the spin–orbit interaction; the Bir–Aronov–Pikus (BAP) mechanism based on the exchange interaction with holes; and spin relaxation

due to the hyperfine interaction with lattice nuclei. The first two mechanisms are suppressed because the electron orbital motion in the donor is quenched. The BAP mechanism is irrelevant because the steady-state hole concentration in the weak-pump limit is exceedingly small in *n*-type semiconductors. The only operative mechanism in the situation at hand is that of the hyperfine interaction with nuclei. With this mechanism, the estimate indicates that the electron residence time at donor is on the order of 10^{-10} s. In our case, correlation times as short as those cannot be caused by the electron hopping over the randomly distributed donors, because the impurity concentration is small [11]. Electron transitions to the conduction band are inefficient at helium temperatures. We relate the exceedingly short electron spin correlation times to the specific features of the structure under study. In this structure, the buffer layer is bounded on both sides by high barriers, whose residual doping is the same as in the buffer; i.e., $N_d - N_A \approx 10^{14}$ cm^{-3}. In equilibrium, electrons transfer from the barriers to the buffer layer. Thus, in addition to the electrons localized at donors, "excessive" electrons appear, which either concentrate near the bottom of the conduction band or are bound to neutral donors to form D^- centers. The free-electron spin-flip scattering by neutral donors (or hopping of a weakly bound second electron over donors) can be an efficient mechanism for changing the spin state of the electrons at neutral donors. This will result in the shortening of the spin correlation time. This model explains qualitatively the origin of the extremely long spin memory time $\tau_s = 290 \pm 30$ ns of electrons localized at shallow donors.

We are grateful to I.A. Merkulov for discussion. This work was supported in part by the Russian Foundation for Basic Research (project nos. 00-02-16991 and 01-02-17906), The Project of Young Scientists of the Russian Academy of Sciences on the Fundamental and Applied Research (no. 36), and the CRDF (grant no. RPI-2252).

REFERENCES

1. G. A. Prinz, Science **282**, 1660 (1998).
2. G. Burkard, D. Loss, and D. P. DiVincenzo, Phys. Rev. B **59**, 2070 (1999).
3. C. Weisbuch, PhD Thesis (1977).
4. R. I. Dzhioev, B. P. Zakharchenya, V. L. Korenev, and M. N. Stepanova, Fiz. Tverd. Tela (St. Petersburg) **39**, 1975 (1997) [Phys. Solid State **39**, 1765 (1997)].
5. J. M. Kikkawa and D. D. Awschalom, Phys. Rev. Lett. **80**, 4313 (1998).
6. *Optical Orientation, Vol. 8: Modern Problems in Condensed Matter Science*, Ed. by B. P. Zakharchenya and F. Meier (North-Holland, Amsterdam, 1984; Nauka, Leningrad, 1989).
7. G. Fishman, C. Hermann, G. Lampel, and C. Weisbuch, J. Phys. (Paris) **35**, C3-7 (1974).
8. C. Weisbuch and C. Hermann, Phys. Rev. B **15**, 816 (1977).
9. *Semiconductors and Semimetals*, Vol. 3: *Optical Properties of III–V Compounds*, Ed. by R. K. Willardson and A. C. Beer (Academic, New York, 1967; Mir, Moscow, 1970), Chap. 11.
10. D. Paget, Phys. Rev. B **24**, 3776 (1981).
11. K. V. Kavokin, Phys. Rev. B **64**, 075305 (2001).

Translated by V. Sakun

JETP Letters, Vol. 74, No. 3, 2001, pp. 186–189. Translated from Pis'ma v Zhurnal Éksperimental'noĭ i Teoreticheskoĭ Fiziki, Vol. 74, No. 3, 2001, pp. 204–208.

Preparation and Study of the Optical Properties of Porous Graphite

V. A. Karavanskiĭ[1]*, N. N. Mel'nik[2], and T. N. Zavaritskaya[2]

[1] *Center of Natural-Science Research, Institute of General Physics, Russian Academy of Sciences, Moscow, 119991 Russia*
[2] *Lebedev Physical Institute, Russian Academy of Sciences, Leninskiĭ pr. 53, Moscow, 119991 Russia*
* *e-mail: karavan@kapella.gpi.ru*

Received July 11, 2001

Optical properties of porous graphite samples prepared by electrochemical etching were investigated. It is found that electrochemical etching modifies their Raman spectra and gives rise to photoluminescence. The evolution of Raman spectra at the initial etching stages is studied in detail. A model is proposed explaining the salient features of the observed Raman spectra. It assumes the appearance of graphite nanoparticles and the formation of sp^3 bonds between the graphite planes at the nanocrystal boundaries. © *2001 MAIK "Nauka/Interperiodica".*

PACS numbers: 78.67.Bf; 78.30.Ly; 78.55.Mb; 81.40.Tv

Extensive studies of nanocrystalline materials are caused by their unique properties, which are absent in the initial bulk crystals [1]. The appearance of new properties is primarily due to the size quantization effects and to the presence of a vast specific surface, whose properties, however, cannot be regarded separately from the properties of nanocrystal bulk. This can result in the cardinal transformation of the electronic and phonon states and give rise to new electric and optical properties [1].

By now, a wide diversity of methods have been developed for preparing nanocrystalline materials, one of which is electrochemical etching [2]. It turned out that, for some electrochemical etching regimes, the material is removed leaving behind it multiple channels of nanometer size in the initial crystal. The rest of the material, as a rule, preserves its initial composition, structure, and crystal orientation and, in the case of a sufficiently high porosity, can be regarded as a nanocomposite composed of oriented nanocrystals with various degree of bonding to each other [3]. This method found widespread use in the formation of porous semiconductor structures, among which porous silicon is most familiar [4]. One of the merits of this method is that it provides a possibility of choosing the appropriate initial material and exhibits a certain flexibility in choosing the formation conditions (voltage, current density, composition and concentration of electrolytes, temperature, and illumination conditions), thereby controlling the porosity, the characteristic pore sizes (and the size of the remaining framework), and the pore depth (thickness of the porous layer). Although, it should be noted that a detailed understanding of the electrochemical processes at a level allowing the description of pore microstructure is presently lacking in the majority of cases [4].

Apart from the silicon nanostructures (the basic material in microelectronics), much attention is being given at present to the carbon nanostructures. This is explained not only by the widespread use of graphite modifications such as graphite and diamond but also by the discovery of a series of new structural modifications such as amorphous carbon, fullerenes, nanotubes, etc. [5, 6], whose properties radically differ from the properties of graphite and diamond. It is worth noting that there is no consensus in the literature on the interpretation of the properties of carbon nanostructures. The explanation of the origin of so-called *D* and *G* bands in disordered graphite provides an example [7].

In this work, samples of porous graphite were obtained by electrochemical etching, and their Raman spectra were studied. It was found that electrochemical etching gives rise to photoluminescence. The transients of Raman spectra at the initial etching stages were studied in detail and the appropriate interpretation was given. It is shown that the appearance of the *D* band is due to the formation of sp^3 bonds between the neighboring graphite layers at the boundaries of nanocrystals formed. These bonds are shown to radically modify the Raman spectra and give rise to additional Raman bands.

Samples of porous graphite were prepared from high-quality (ZYA grade) single crystals of pyrolytic graphite (Union Carbide Corporation) by anodization in a two-compartment electrochemical cell with platinum electrodes. Hydrofluoric acid HF(49%) and ethanol taken in the ratio 1 : 1 were used as an electrolyte. The samples were prepared with anodizing times varying from 1 to 10 min at a current density from 1 to

50 mA. Samples with smooth transition layers between the nonetched and etched areas were also prepared. Note that we did not find any indications on the use of anodic etching for graphite in the available literature, so that the corresponding etching mechanism calls for additional investigation. As to the choice of the electrolyte composition, we were only aware that it was used in the formation of porous layers on SiC crystals.

Raman and photoluminescence (PL) spectra were recorded on a U-1000 spectrometer in the regime for studying microsamples. The exciting radiation (488 nm) was focused to a spot as small as 10 μm in diameter. This allowed us to study the homogeneous and transition areas of the sample surface and monitor the absence of the laser heating effect on the sample. The Raman spectra were recorded with a resolution of 1–5 cm^{-1}.

The Raman spectrum of the prepared porous graphite is shown in Fig. 1a (curve *2*). One can see that etching modifies the surface and renders a Raman spectrum similar to the spectrum of nanocrystalline graphite. The Raman spectra of the initial graphite (curve *1*) and of the pyrolytic graphite irradiated with carbon ions (curve *3*) [8] are presented for comparison. Note that, despite the cardinally different technologies of sample preparation, the spectra are similar to each other. The samples of pyrolytic graphite with long anodic etching times exhibit photoluminescence (Fig. 1b, curve *4*). For comparison, the photoluminescence spectrum of a carbon film prepared by vacuum deposition of carbon plasma on a metallic substrate is also shown in Fig. 1b (curve *5*) [9]. These curves also clearly demonstrate that the spectra of the samples prepared by different methods are similar. The optical, especially Raman, spectra of a particular material are quite specific [10] and, therefore, often used for the analysis of the composition and structure of a material. The similarity of the Raman spectra is evidence that we deal in this particular case with the same carbon-based substance.

The anodic etching procedure made it possible to trace the evolution of a Raman spectrum in passing from the initial single-crystal graphite to the nanocrystalline state. To do this, a series of Raman spectra were recorded both for the samples differing in the degree of anodization and for the gradient transition region from the unetched to the etched part of the surface. The sequence of Raman spectra in Fig. 2 demonstrates the evolution of a graphite spectrum on the way to the spectrum of porous graphite. In the Raman spectrum of an initial single crystal, a line at ~1582 cm^{-1} in the range 1250–1700 cm^{-1} is due to the in-plane E_{2g} mode (curve *1*). At the beginning of the etching process, an additional narrow Raman line appears at ~1606 cm^{-1} (curve *2*), and a band with a maximum at ~1355 cm^{-1} appears simultaneously. As the degree of etching increases, these bands become stronger and broader (curves *3*, *4*). For samples with the maximal degree of etching, all three lines merge into two broad unresolved

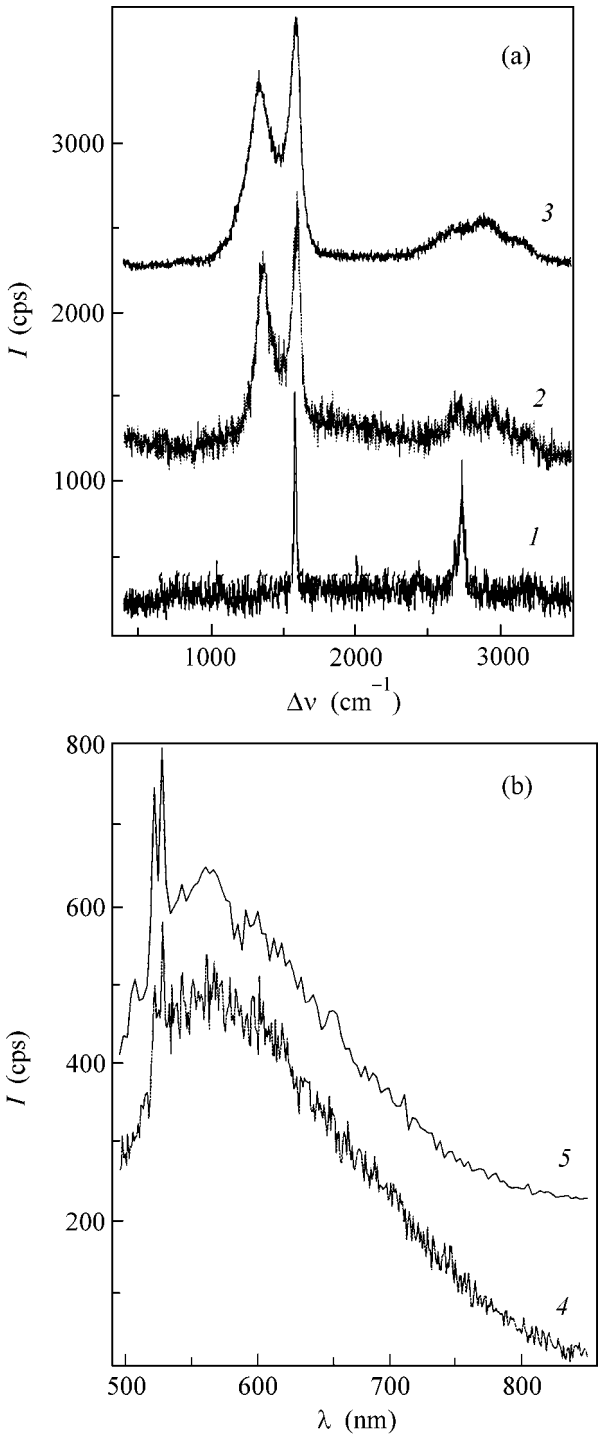

Fig. 1. Raman and PL spectra of porous graphite. (a) Raman spectra: (*1*) initial substrate; (*2*) porous layer, and (*3*) pyrolytic graphite irradiated with carbon ions [8]. (b) PL spectra: (*4*) porous layer and (*5*) carbon layer from [9].

bands with maxima at ~1354 and ~1595 cm^{-1} (curve *5*). In the literature, these bands are referred to as *D* and *G* bands, respectively (see, e.g., [7]).

Raman spectra are used extensively in studying various carbon modifications. However, there is still no

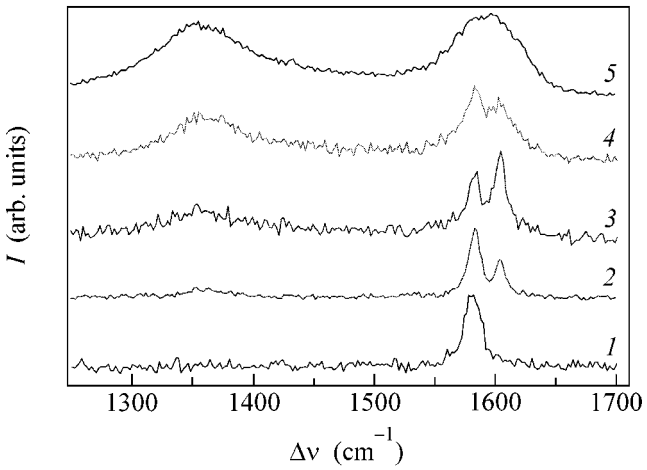

Fig. 2. A sequence of Raman spectra corresponding to the areas differing in their degree of anodization. Curves *1* and *5* relate, respectively, to the initial graphite and the porous graphite with the maximal degree of anodization.

consensus on the interpretation of the Raman spectra of disordered carbon structures. Two approaches to the explanation of their spectra can be distinguished.

In the first approach, a model assuming the violation of the wave-vector selection rules is used. New bands in the Raman spectrum are assigned to the maxima of phonon density of states in the initial substance. For example, band *D* is assigned in [11] only to the phonon density of states at point *K* in the Brillouin zone of a bulk single crystal, while the intensity ratio $I(D)/I(G)$ is determined by the nanocrystal size.

In the second approach, the new bands are assigned to new polymorphic carbon modifications, e.g., to clusters containing distorted sp^3 bonds. The authors of [7] analyzed the Raman spectra of the disordered and amorphous carbon and arrived at the conclusion that the ratio $I(D)/I(G)$ carries information about the amount of carbon atoms containing the sp^3 bond. In [8], the first- and second-order Raman spectra of a disordered carbon were compared with each other to conclude that the nanoparticles in some samples also contain sp^3 bonds.

To interpret the results of this work, we assume that, when etching, sp^3 bonding can arise between atoms situated in different atomic planes near the boundaries of micropores passing through the atomic layers with sp^2 bonds. This assumption is confirmed by the Raman spectra of a freshly cleaved graphite single crystal (Fig. 3). Spectrum *1* corresponds to the atomic layer in graphite. Spectrum *2* is due to the region with a high density of terraces that appear upon cleaving graphite with a force perpendicular to the layer plane. A broad band in the range 1300–1450 cm^{-1} is clearly seen in spectrum *2*. One can assume that the formation of sp^3 bonds (from the broken bonds at the edges of the disrupted planes) upon cleaving a single crystal is more probable than the formation of nanocrystals or a strongly disordered structure.

The evolution and the aforementioned features of the Raman spectra of porous graphite can be explained in terms of the following qualitative model. The anodization of graphite gives rise to micropores passing through the atomic planes. Simultaneously, the sp^3 bonds arise near the pore walls and bind the atoms of the neighboring atomic planes together. The vibrations of the carbon atoms directly bonded by the sp^3 bonds contribute to the Raman band in the range 1300–1450 cm^{-1}. Moreover, these bonds modify the vibrations of pure graphite. Let us consider the E_{2g} mode (1582 cm^{-1}). This mode corresponds to the in-plane atomic vibrations, with the atoms of the neighboring planes moving in antiphase. The bonding between such atoms should increase the frequency of their in-plane vibrations. Correspondingly, the line at 1606 cm^{-1} can be assigned to this vibration. The fact that the frequency of this vibration is virtually the same for the samples differing in the degree of anodization provides evidence for its local character. Therefore, the atoms with sp^3 bonding between the layers contribute simultaneously to the broad band in the range 1300–1450 cm^{-1} and to the narrow line at 1606 cm^{-1}. Clearly, as the number of such atoms increases, the area of these bands will change simultaneously. An increase in the degree of etching will lead to an increase in the number and size of micropores, i.e., to the increase in the micropore surface area and, hence, to the increase in the number of carbon atoms containing the sp^3 bond. At the same time, the characteristic sizes of the remaining graphite domains will decrease, while their dispersion will increase. In combination, this can be the cause for the observed inhomogeneous broadening of all Raman bands (Fig. 2, curves 2 ⟶ 3 ⟶ 4 ⟶ 5) with an increasing degree of anodization (increase in the anodization time and current density). That the sp^3 bonds relate to the graphite nanocrystals, and not to the other carbon formations (e.g., in the pores between the nanocrystals), becomes evident from the character of the second-order Raman spectra (Fig. 1). The frequency analysis confirms [8] that the scatterers contributing to the bands with maxima in the range 1355 and 1580 cm^{-1} interact with each other; i.e., they refer to the same object (nanocrystal).

Turning back to photoluminescence properties, note that, although the nature of PL was not analyzed in detail in this work, the following is noteworthy. A change in the PL intensity correlates with the increase in the number of sp^3 bonds and increases with increasing degree of graphite etching. It follows from the Raman spectra that no other substances are synthesized in the films of porous graphite upon etching; i.e., the emergence of PL is most likely due to the presence of a multitude of small graphite nanocrystals that also contain sp^3 bonds. Although there was no direct evi-

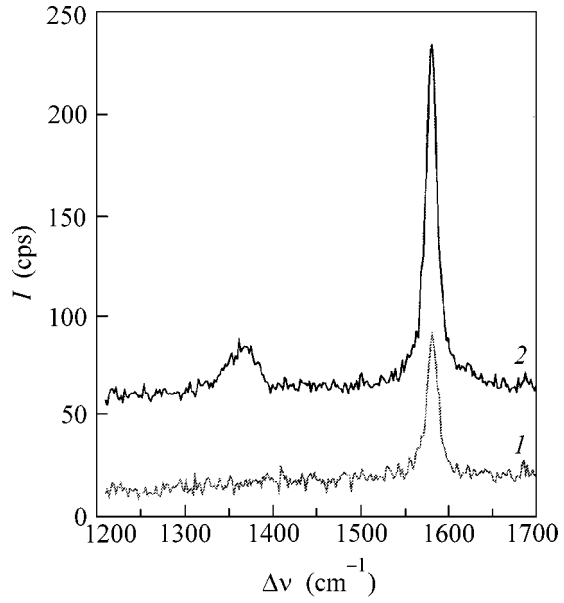

Fig. 3. Raman spectra of graphite. Curve *1* is for the flat plane of the initial graphite single crystal, and curve *2* corresponds to the nearby area with a high density of terraces.

dence (e.g., band shift with increasing degree of etching) for the size-quantization nature of PL, this cannot be considered as an argument against such an explanation, because the emission characteristics of nanoobjects strongly depend on many parameters (size, shape, surface state, surroundings, etc.). Note in conclusion that PL is inherent in a wide range of nanocomposites, including semiconductor structures and carbon nanostructures [9], so that elucidation of its nature requires a detailed and quite accurate inspection in each particular case.

Thus, the samples of porous graphite were prepared by electrochemical etching, and their optical properties were studied. It is found that electrochemical etching gives rise to graphite nanoparticles and photoluminescence. The evolution of Raman scattering spectra at the initial etching stages is studied in detail. The appearance of the *D* band (~1355 cm^{-1}) is satisfactorily explained by the formation of sp^3 bonds between neighboring graphite layers at the nanocrystal boundaries. It is shown that the additional bonds between the graphite layers are responsible for the new band at 1606 cm^{-1}.

This work was supported in part by the Russian Foundation for Basic Research (project no. 00-02-17864), the program "Integration of Higher School and Fundamental Science" (project no. A0103), the program "Physics of Solid-State Nanostructures" (project nos. 97-1073, 2000-2F), and the program "Perspective Technologies and Devices in Micro- and Nanoelectronics" (project no. 1).

REFERENCES

1. H. Gleiter, Acta Mater. **48**, 1 (2000).
2. A. G. Cullis, L. T. Canham, and P. D. J. Calcott, J. Appl. Phys. **82**, 909 (1997).
3. O. Bisi, S. Ossicini, and L. Pavesi, Surf. Sci. Rep. **38**, 1 (2000).
4. L. T. Canham, Appl. Phys. Lett. **57**, 1046 (1990).
5. M. S. Dresselhaus and G. Dresselhaus, J. Electroceram. **1–3**, 273 (1997).
6. Y. Lifshitz, Diamond Relat. Mater. **8**, 1659 (1999).
7. A. C. Ferrari and J. Robertson, Phys. Rev. B **61**, 14095 (2000).
8. N. N. Mel'nik and T. N. Zavaritskaya, Kratk. Soobshch. Fiz., No. 1, 19 (2001).
9. N. N. Melnik, T. N. Zavaritskaya, M. V. Rzaev, *et al.*, Proc. SPIE **4069**, 212 (2000).
10. *The Raman Effect*, Ed. by A. Anderson (Marcel Dekker, New York, 1973), Vol. 2.
11. R. J. Nermanich and S. A. Solin, Phys. Rev. B **20**, 392 (1979).

Translated by V. Sakun